United States
Naval Postgraduate School

EHD RESEARCH

FINAL REPORT FOR THE YEAR

1969-70

by

Oscar Biblarz, K. E. Woehler, and T. H. Gawain

30 December 1970

NAVAL POSTGRADUATE SCHOOL
Monterey, California

Rear Admiral R. W. McNitt, USN
Superintendent

M. U. Clauser
Academic Dean

ABSTRACT:

This is the second year-end report on the EHD contract. Whereas previous work concentrated on building up the experimental facility and on delineating the effects of turbulence on breakdown, this work details the effects of turbulence on charged particle mobility. The two-phase injector is used exclusively.

Spectral measurements of velocity and collector current are reported. These are used to determine the potential use of EHD in anemometry and to deduce particle size distributions. Measurements of charge distribution are also reported and a comparison is made between these and the spectral measurements.

Equations defining an axisymmetric, turbulent EHD flow have been derived. Also, the feasibility of flow separation control with an EHD interaction has been investigated.

Research plans for the coming year are outlined in this report.

FOREWORD

This is a continuation of the EHD Research program started on September of 1968 at the Naval Postgraduate School, Monterey, California. This work is sponsored by the Naval Air Systems Command under the technical cognizance of Dr. H. R. Rosenwasser.

The following personnel contributed to the work during the reporting year: Assistant Professor Oscar Biblarz (Principal Investigator), Professor T. H. Gawain, and Associate Professor K. E. Woehler.

The help of Mr. Patrick Hickey in the laboratory is gratefully acknowledged.

One Master thesis and one Aeronautical Engineer thesis were generated during this period and they are included as Appendices C and D of this report. Professor Biblarz' paper, "Analysis of Optimum Charged Particle Size Based on the Conversion Efficiency of Electrogasdynamic Generator" is to be published in the Journal of Energy Conversion. A paper titled, "Electrohydrodynamic Flows and Some Effects of Turbulence on these Flows," was given at the ENERGY 70 Conference in Las Vegas by Professor Biblarz.

Professor T. H. Gawain presented a paper entitled "Numerical Simulation of Transition and Turbulence in Plane Poiseuille Flow" at the Second International Conference on Numerical Methods in Fluid Dynamics in Berkeley, California in September 1970. In a second paper delivered to the Conference on Turbo Machinery at the Naval Post-graduate School in December 1970, Professor Gawain presented an

invited paper in which he discussed a proposed new unified heuristic model of fluid turbulence and also gave an account of recent work on computer simulation of turbulence. These papers did not refer specifically to EHD applications, but nevertheless dealt with turbulence fundamentals that relate significantly to the EHD problem.

TABLE OF CONTENTS

LIST OF FIGURES (MAIN TEXT)

LIST OF SYMBOLS (MAIN TEXT)

A = Area of collector

a = Amplitude of spectral component

C = Capacitance

E = Electric field

E_b = Breakdown field

e = Charge of an electron or elementary charge

f = Frequency

I = Current

I_c = Corona current

I_g' = EHD probe current

i = $\sqrt{-1}$

m_p = Mass of charged particles

N = Number density of droplets

n_P = Number density of charged particles

$n(R)$ = Density defined by Equation 25

$\hat{n}(R)$ = Density defined by Equation 38

P = Percentage of droplets that fission into two

Q = Charge on capacitor

Q_1 = Long time constant charge

Q_2 = Short time constant charge

$\bar{Q}$ = Average charge

q = Charge per particle

R = Particle radius; resistance

r = Particle radius

RH = Relative humidity

T' = Normalized RMS, spectral gas velocity

$T'_g(f)$ = Ratio of collector to anemometer spectral output, normalized

t = Time

U = Steady component of velocity

U_R = Signal at R_1

U_p = Steady component of particle velocity

U_∞ = Steady component of carrier gas velocity

u = Fluctuating component of velocity

u_p = Fluctuating component of particle velocity

u_∞ = Fluctuating component of carrier gas velocity

u'_p = Spectral magnitude of particle velocity

u'_∞ = Spectral magnitude of carrier gas velocity

V_o = Voltage applied to charge measuring probe

v_D = Drift velocity

v_p = Particle velocity

$v_p^{(0)}$ = Particle velocity for vanishing mass

$v_p^{(1)}$ = Perturbation particle "velocity" due to mass

z = Number of electronic charges

ϵ = Perturbation parameter (Equation 7)

μ = Mobility of particles

μ_∞ = Viscosity of carrier gas

ρ_c = Space charge density

ρ_p = Mass density of particles

τ = RC (time constant)

τ' = Time constant defined by Equation 50

τ_v = Equilibration time for particles

τ_∞ = Characteristic time of higher frequency fluctuations

I. INTRODUCTION

A. Method of Approach

Last year's Final Report[1] outlined broadly the motivations for this program. The approach is based on a fundamental study of fluid dynamic effects on the EHD process and in particular on the EHD generator. It has been proposed that if atmospheric air could be made into an efficient EHD working medium then the utility of the conversion principle could be expanded, particularly with regard to aircraft applications.

Heretofore, work in the field has focused in the development of a working generator with a relative neglect of efforts on fundamentals. This approach while expedient was risky because, unlike the internal combustion engine, the simple principles of EHD can combine in subtle ways to degrade markedly the optimum performance of a generator. Our approach has been to build an experimental generator, not necessarily an optimum one, and through detailed measurements diagnose its behavior and attempt to improve its performance. But experimental work alone is not sufficient since there are too many ways that the variables can interact, hence a concurrent analytical program has been also under way.

B. Summary of Previous Work

The fluctuating velocity components of the turbulent flow field influence the EHD process in at least two ways: First, there is an enhancement of the breakdown potential of the carrier gas and, second, there is an effect on the particle drift velocity itself. It has been shown[2] on the basis of some heuristic arguments that the

turbulent flow field could be expected to affect the charged particle motion on an equal basis with the electric field. The electrons, because of the Coulomb coupling, can be forced by the eddies through tortuous paths as they travel between electrodes and thus their ability to "burn" a path and cause breakdown is diminished. However, only a moderate increase of the breakdown potential of air has been observed, and we now believe that our present apparatus lacks the "complete" turbulent characteristics. The wake of the cylinder is indeed a region of intense vortices (with local velocity perturbations as high as 20% of the main flow) but these are in themselves typically laminar and lack the three-dimensionality of the fluctuating components of turbulence. The mere fact that we can measure twice the Strouhal frequency (see Part IIB and Appendix B) at the rear of the cylinder implies that laminarity persists. The truly intense, turbulent flow field with electronegative additives is still expected to increase the breakdown potential of atmospheric air by a factor of three or more.

Some concepts of optimum particle size are treated in Reference 3. For subsonic, viscous generators it appears as if particles (water droplets in air) of size between 10^{-7} and 10^{-5} m with up to 100 electronic charges are optimal. The fact that they typically have to be charged below the diffusion charging limit means that a scheme of growing droplets after an initial charging should be adopted. This has already been pointed out elsewhere[4]. The above definition of optimum particle size is somewhat too general since losses have been ignored but it does bracket the useful range of particle size and charge. Actually, it appears as if the range of

optima of particle size, charge, and number density are quite critical and that performance estimates should be based on a strict adherence to a fixed range of parameters. Thus, we must be able to measure actual particle size and charge distributions in order to assess why an analysis may or may not be deficient and why a generator performs below expectations. Part II and III of this report describe our efforts toward the measurement of such distributions.

The experimental facility used in Part II and III has been described in last year's report[1]. The channel cross section is 2" x 4" and the air flow is typically at 55 m/sec upstream of the cylinder and at atmospheric conditions. The cylinder itself is 2 cm in diameter and the steam enters through this cylinder and is discharged at the wake through a nozzle which contains the corona discharge. The exit diameter of the nozzle is .055 inches and it acts as a throat. The mass flow rate of steam is 0.001 lbm/sec at various degrees of supersaturation with a boiler pressure of 13 psig. The collector is a traversable needle typically stationed at the axis of the steam jet, about 5 mm downstream (see Figure 1). The droplets grow in the wake because of the mixture cooling with the eddies of the flowing air. For the charge distribution measurements (Part III) the collector is a ring also centered on the steam jet through which a probe could be inserted; the pressures for measurements reported in Part III are 13 psig and 8 psig. The ring was grounded directly through a microammeter.

C. Contents of this Report

Attempts at making a fluid dynamic diagnostic tool out of the EHD collector (closely related to the particle determination principles)

are the subject of a Master thesis included as Appendix B. If the drift velocity of the particles is low and if the electrical field does not appreciably disturb the fluid, then the collected charged particles bring with them information about the turbulent eddies. The EHD probe itself is more rugged than the hot wire anemometer and picks up electrical signals that need no further amplification. The frequency response of the EHD (or EGD) probe depends on particle size (i.e., only the small particles can react to high frequency oscillations) and this may also be higher than the hot wire.

An investigation was also carried out to determine if an EHD interaction could control flow separation. This is the subject of an Engineer thesis and is included as Appendix C. The electric pressure that may be exerted with atmospheric air is at the lower limit of values needed for flow separation prevention.

The theoretical aspects of this research, including the work on turbulence, has resulted in the development of a fairly comprehensive mathematical analysis. It is the subject of a separate report titled, "A Mathematical Model of the Basic EHD Process Including Effects of Turbulence," by Professor Gawain. For purposes of cross-reference, an abstract of this work is included as Part II A.

In Part II B, spectral measurements are analyzed for the purpose of estimating particle size distributions.

Part III reports on charge distribution measurements with an electrical probing technique.

IIA. "A Mathematical Model of the Basic EHD Process Including Effects of Turbulence" by T. H. Gawain

Abstract

A mathematical model of the basic EHD process is developed and described. The carrier fluid is treated as incompressible and turbulent. The injected particles are treated as uniform in mass and electrical charge. The analysis is broken down into three phases, namely, the basic flow, the perturbation due to injection of mass, and the perturbation due to introduction of electrical charge. This method greatly simplifies the analysis. A final system of nine basic partial differential equations is obtained. These equations, along with the appropriate boundary conditions, are shown to fix the fluid and particle velocities and particle density at all points in the field. The basic equations are developed in a fully non-dimensional form.

The mathematical model here presented is novel and unique in its analytical approach and in its treatment of turbulence effects. Thru computer simulation, it offers new possibilities for the study and development of EHD power generation.

The mathematical model has been developed to the point where it is ready for computer programming. Such a program would be useful for estimating optimum design parameters and performance possibilities for a wide variety of axi-symmetric configurations and a wide range of operating conditions.

IIB. Spectral Turbulence Analysis

In order to address ourselves to the behavior of charged particles in a turbulent field we will be concerned with spectral phenomena. As was mentioned earlier, the turbulent field may affect the particle

drift velocity and the breakdown of the carrier medium. The drift velocity is still the key parameter here and it must remain small in both its steady and fluctuating components in order for the coupling between the flow and electric fields to be significant.

The drift velocity can be obtained from a solution of the particle momentum equation. If we write this equation in its Lagrangian form neglecting pressure forces on the particle and assuming that the field direction is opposite to the mean fluid motion (we are really dealing with components of the fluid velocity and electric field along the direction of motion of the particle), we have, (see List of Symbols),

$$m_p \frac{dv_p}{dt} = \underbrace{6\pi R \mu_\infty (v_\infty - v_p)}_{\text{Stoke's Drag}} - \underbrace{qE}_{\substack{\text{electrical} \\ \text{force}}} \tag{1}$$

We assume Stoke's drag on a sphere throught the range of radii of interest even though the actual drag is higher for Reynolds numbers greater than one. This assumption is a valuable simplification and is consistent with other assumptions in this analysis. The electric force is shown as opposing the fluid motion as would be the case in an EHD generator.

If the electrical force on the particle is vanishingly small and if the fluid velocity is constant in time, we find that the equilibration or e-folding time is

$$\tau_v = \frac{m_p}{6\pi R \mu_\infty} \tag{2}$$

which for a spherical particle of density ρ_p becomes

$$\tau_v = \frac{2}{9} \frac{R^2 \rho_p}{\mu_\infty} \tag{3}$$

As the particles approach the size of molecular ions, however, we know that the electric field presence is usually dominant over the inertia effect (small enough mass) so that

$$m_p \frac{dv_p}{dt} + qE \approx qE = 6\pi R\mu_\infty (v_\infty - v_p) \tag{4}$$

and we have the usual[1] definition for the mobility

$$\mu E = v_\infty - v_p = \frac{qE}{6\pi\mu_\infty R} \tag{5}$$

where μE represents the drift velocity which is proportional to the electric field for a wide range of radii (i.e., the mobility is independent of the electric field).

For particles in the micron range, the effects of inertia begin to be felt and we shall include them as a perturbation. Rewriting Equation 1 as

$$\frac{m_p}{qE} \frac{dv_p}{dt} = \frac{m_p}{\tau_v} \frac{(v_\infty - v_p)}{qE} - 1 \tag{6}$$

we let ϵ be a small parameter defined by

$$\epsilon = \frac{m_p}{qE} \tag{7}$$

and $$v_p = v_p^{(0)} + \epsilon\, v_p^{(1)} + O(\epsilon^2) \tag{8}$$

Therefore, substituting (8) into (6)

$$\epsilon \frac{dv_p^{(0)}}{dt} + O(\epsilon^2) = \left[\frac{m_p (v_\infty - v_p)}{\tau_v qE} - 1 \right] - \epsilon \frac{m_p v_p^{(1)}}{\tau_v qE} + O(\epsilon^2) \tag{9}$$

Equating the terms according to the power of ε we get

$$(v_\infty - v_p^{(0)}) = \mu E \tag{10}$$

and

$$\frac{dv_p^{(0)}}{dt} = -\frac{m_p}{\tau_v}\frac{v_p^{(1)}}{qE} \tag{11}$$

Equation (10) represents the vanishing of the inertia term and, hence, we introduce the mobility defined earlier in Equation 5. The perturbation in the particle velocity is contained in Equation 11. Now, if the electric field is steady (the electric field is made up of an external field which is the drop across a load resistor and of the space charge field; the latter may be unsteady due to space charge oscillations but these disturbances travel at the speed of light which is much faster or higher frequency than fluid dynamic oscillations and hence we shall ignore them), then

$$\frac{dv_p^{(0)}}{dt} = \frac{dv_\infty}{dt} \tag{12}$$

and

$$v_p^{(1)} = -\frac{qE\,\tau_v}{m_p}\frac{d\,v_\infty}{dt} \tag{13}$$

Hence, going back to Equation (8) we get

$$\boxed{v_p = v_\infty - \mu E - \tau_v \frac{d\,v_\infty}{dt} + O(\varepsilon^2)} \tag{14}$$

or

$$v_D = v_\infty - v_p = \mu E + \tau_v \frac{d\,v_\infty}{dt} \tag{15}$$

Note that if v_∞ is steady we get the same result as when we ignored the inertia term. Good coupling between the electric field and the fluid still requires that v_D be small compared to v_∞, or

$$\frac{v_D}{v_\infty} = \frac{\mu E}{v_\infty} + \frac{\tau_v}{v_\infty} \frac{d v_\infty}{dt} \ll 1.0 \tag{16}$$

The first term is the familar no-slip condition. The second term arises from the need to have the particles follow the fluctuating component of the fluid velocity quite closely if turbulence is to have an effect. If the mass is small enough (i.e., small τ_v) then the coupling may be good at a particular frequency in question. In fact, we can cast Equation (16) in an order of magnitude form by replacing E by E_b (the breakdown value) and

$$\frac{1}{v_\infty} \frac{d v_\infty}{dt} < \tau_\infty^{-1} \tag{17}$$

where τ_∞ is some characteristic time of the high frequency fluctuations (which may range as high as 50 KHz in turbulent flows). Therefore, the inequality in Equation 16 is satisfied when the following is satisfied.

$$\frac{\mu E_b}{v_\infty} + \frac{\tau_v}{\tau_\infty} \ll 1.0 \tag{18}$$

We will look at the above relation and Equation (14) in more detail by specializing them respectively to the injector and the generator regions of the EHD generator.

A.1 Corona Injector Region

The region just outside of the corona-steam injector is one where the highest field of the conversion regions may exist. The charged particles

which have been forming and growing in the corona now emerge to mix with the main flow at the wake of the cylinder as shown in Figure 1. Depending on their size and charge, many will be lost to the corona attractor. In fact, the ratio of the corona current, I_c, to the current injected into the conversion region, I_g, is an indication of what range of particles are lost to the corona ring.

$$\frac{I_c}{I_g} \simeq \frac{A\rho_c\, v_D}{A\rho_c\, v_\infty} = \frac{v_D}{v_\infty} \tag{19}$$

ρ_c = space charge density (coulombs/m^3)

A = collection area (same for both)

or

$$\frac{I_c}{I_g} \lesssim \frac{\mu E b}{v_\infty} + \tau_v\, \tau_\infty^{-1} \tag{20}$$

Since the right-hand-side is a maximum, then the equality in Equation (20) represents the smallest radius that makes up the corona current (the dependance of μ and τ_v in this range is assumed to be monotonic in the radius).

The injector, as operated for data given in the rest of this section and in Appendix B, was typically running with the following parameters

$$\frac{I_c}{I_g} \approx 2 \tag{21}$$

$v_\infty \approx 430$ m/sec (sonic for emerging steam*)

$\tau_\infty^{-1} \approx 6$ KHz (steam jet maximum frequency)

*v_∞ is about 20 m/sec in the neighborhod of the probe.

so that Equation (20) becomes

$$2 \lesssim \frac{\mu E_b}{430} + 6 \times 10^3 \tau_v \qquad (22)$$

which satisfies the equality for water droplets in air charged to the diffusion charging limit and with a radius of 6×10^{-6} m ($\tau_v \approx 3 \times 10^{-4}$ sec and $\mu E_b \approx 30$ as shown in Figures 2 and 3). This implies that particles of radius 10^{-5} m and above will be essentially drifting to the corona electrode and not be injected into the flow.

The arguments given above are somewhat simplified and they do not really focus on all the inefficiencies of the injector. Apparently, the condensation and charging times are smaller than the travel time through the corona so that most particles grow much beyond a micron and can charge up to the diffusion limit (see Figure 4). Hence, much of the total current is lost to the corona because of this high drift velocity. There is a extra complication here in that the droplets emerging from the injector nozzle can grow further depending on the humidity of the air flow, so that the size "filtering" is by no means all restrictive.

A.2 Generator Region

The region in the wake of the cylinder, typically 5 mm away from the steam nozzle along its centerline, was surveyed with a hot wire anemometer and with the EHD collector grounded. These experiments pertain to fluid dynamic diagnostics (see Appendix B) and to charged particle size determination. Hot wire measurements of the spectral, normalized RMS velocity are shown in Figure 5. Air was injected through the steam system to simulate the steam jet conditions and to

obviate the two-phase complications. As can be seen from Figure 4 for frequencies above 500 Hz, the RMS velocity is insensitive to the spacing variation from the nozzle exit and the data seems altogether more reliable. The second peak of the curve is associated with twice the Strouhal frequency of the cylinders which characterizes the vortex shedding. This, incidentally, is what points out that the wake region may not be truly turbulent in spite of the high intensity of the vortices. The normalized, AC output from the EHD probe fed through a frequency analyzer is shown in Figures 6 and 7 for two different measurements each at 25% and 50% relative humidity. The two curves in Figure 7 are shown for different steam pressures. Roughly, the trends are the same, namely, a low frequency rise and a high frequency drop off. The rise is of course due to the vortex shedding at twice the Strouhal frequency. The difference in the high frequency response may be attributed to the charged particles size distribution as will be shown below.

The current arriving at the probe is given by

$$I_g = qn_p \, v_p \, A \tag{23}$$

A = probe collecting area

qn_p = total number of coulombs arriving per cubic meter

v_p = particle velocity

But, as we saw, both the particle velocity and the number and charge per particle are a function of the size of the particle, so that Equation (23) is more appropriately written

$$I_g = A \int_o^\infty v_p \, n \, (R) dR \tag{24}$$

where

$$\int_0^\infty n(R)dR = q\, n_p \tag{25}$$

The particle velocity is given by Equation (14), namely,

$$v_p = v_\infty - \mu E - \tau_v \, du_\infty/dt$$

Now, separating the fluctuating components out

$$v_p = U_p + u_p \tag{26}$$

$$v_\infty = U_\infty + u_\infty \tag{27}$$

where $\begin{cases} U = \text{Steady} \\ u = \text{Fluctuating} \end{cases}$

and assuming that μE is a steady component only, we get

$$u_p = u_\infty - \tau_v \, du_\infty/dt \tag{28}$$

or

$$u_p = u_\infty \left[1 - \tau_v \frac{d}{dt} (\ell n\, u_\infty)\right] \tag{29}$$

The spectral components u_p' and u_∞' should also obey the above equation and it is these components that we wish to display in their RMS form. Now, from a linearized form of the Navier-Stokes equations we know[8] that

$$u' = a \exp(-ift) \tag{30}$$

a = amplitude

f = frequency, $i = \sqrt{-1}$

so that

$$d/dt(\ell n\, u_\infty') = -i\, f \tag{31}$$

and

$$u_p' = u_\infty' \left[1 + if\, \tau_v\right] \tag{32}$$

Therefore, squaring both sides of Equation (32)

$$u_p'^2 = u_\infty'^2 \left[1 + 2i f \tau_v - f^2 \tau_v^2\right] \tag{33}$$

The RMS value is, taking the real part in the brackets,

$$u'_{pRMS} = u'_{\infty\,RMS} \left[1 - f^2 \tau_v^2\right]^{\frac{1}{2}} \tag{34}$$

Hence the spectral probe current becomes,

$$I'_g = A\, u'_{\infty\,RMS} \int_o^\infty \left[1 - f^2 \tau_v^2\right]^{\frac{1}{2}} n(R)dR \tag{35}$$

Normalizing the above we get

$$T'_g(f) = \frac{I'_g / An_p q}{u_{\infty RMS}} = \int_o^\infty (1 - f^2 \tau_v^2)^{\frac{1}{2}}\, \hat{n}(R)dR \tag{36}$$

where

$$o \leq T'_g(f) \leq 1 \tag{37}$$

and

$$\int_o^\infty \hat{n}(R)dR = 1.0 \tag{38}$$

Hence, the ratio of the EGD probe output divided by the corresponding $u_{\infty RMS}$ and normalized gives information about the injected particle radii. The data on Figure 6 ratioed to corresponding values on Figure 5 are plotted on Figure 8. The high frequency trend shown in the figure is typical. As can be seen, for frequencies above 16000 Hz the value of T'_g is zero and the value goes to one as the frequency drops to 500 Hz. The "filtering" function $(1 - f^2 \tau_v^2)^{\frac{1}{2}}$ is a strong function of the particle radius through τ_v as seen from Equation (3). We have then that no particles exist within the non-zero low-pass filter region at 16,000 Hz and that most particles exist within the region where the curve for 500 Hz is nearly one. These "band-pass" curves are shown in Figure 9; we may, therefore, deduce that the range of radii for the particles must be

$$2.2 \times 10^{-6} < R < 7 \times 10^{-6} \text{ meters} \qquad (39)$$

From information about the maximum of $-d\, T_g'(f)/df$ we can surmise that the maximum of the curve is somewhere to the left of 3×10^{-6} m. All of the above have been detailed for curve 1 on Figure 6. The other curve has a very similar shape. Figure 7 shows other data from which it can be seen that the high frequency response depends on the degree of supersaturation of the steam and relative humidity of the air.

The curve for the particle size times charge distribution, sketched on Figure 9, should be asymmetrical because there is higher charging at higher radii as seen from Figure 4. One would expect a Gaussian distribution of the number density if equilibrium prevailed and something close to the diffusion charging limit since there seems to be ample time through the corona. The resulting distribution is indeed devoid of particles in the 10^{-5} range and above, and it does not have particles below 10^{-6} m. Our model is, of course, new and we would like to compile evidence of particle size distributions independent of these measurements. The measurements of charge distribution (see Part III) could in principle provide such an independent check.

For the present injector, the high frequency coupling is not very good and in order to be able to see up to 50 KHz fluctuations we will have to inject particles between 10^{-7} and 10^{-6} m (see Figure 2). This will, incidentally, drop the μE_b product to something in the order of 1 to 10 m/sec. The injector nozzle, therefore, must be much shorter than the present one, or the velocity of the steam much greater. It

seem as if this is a good reason for the success of supersonic injectors[10] where the gas stream moves at high speed through the corona and thus does not have a chance to produce as large a droplet size as we can. Note, finally, that though the value of μE_b is low enough for a particle of radius 10^{-5}m, its ability to couple with the high frequency eddies is poor and the effective turbulent drift velocity, as given by Equation (15), is high.

III. DETERMINATION OF CHARGE DISTRIBUTION (by K. E. Woehler)

A. Performed Measurements

1. Objective

The objective of the measurements performed on the EHD-facility during the months July-August 1970 was to develop a technique to determine the droplet charges, determine the characteristics of the charge distribution as function of the position in the channel and to obtain some information how the charge distribution varies with the operating conditions.

A suitable measuring method of the charge distribution was developed. The distribution was scanned as a function of position in the channel under operating conditions for the present injector (see Introduction). A few orientation measurements at different conditions have been made.

In the following the measuring technique is described, the results are given, and an interpretation of the main features of these results is offered.

2. The Measuring Technique

(a) The principle of the measurement of droplet charge distribution is the collection of the charged droplets on a small, static metal probe which is connected over a suitable RC-circuit to ground. The arrival of a charge on the probe produces a pulse signal the height of which is proportional to the charge. The pulses are then registered by a multichannel pulse height analyzer.

(b) The probe consists of a 1 mm long cylindrical conductor of 1 mm diameter at the end of a conical plexiglas holder (see Figure 10). The probe was movable in axial and lateral direction in the channel pointing with its tip upstream.

(c) The pulse forming network is shown in Figure 11. The arrival of a charge Q at the probe side of the combined capacitor at the time t=0 causes both capacitors to charge up to $Q = Q_{10} = Q_{20}$. The charge Q_{20} flows off through R_1 with a short time constant. The discharge current through R_1 gives the pulse to be registered. The charge Q_{10} flows off with a much longer time constant and for the purpose of the pulse forming this discharge can be neglected. The 100 K resistance avoids the continuous charging of the probe which would soon cause electrostatic disturbance of the flow.

Neglecting this slow bleeding the charge $Q_{10} = Q$ remains constant. The charge on C_2 changes in time as

$$Q_2 = Q_{20}\, e^{-t/\tau} \tag{40}$$

where

$$\tau = R_1 C_2 = 2\ \mu\text{sec.} \tag{41}$$

The signal at R_1 is then

$$U_R = \frac{Q_2}{C_2} = \frac{Q}{C_2}\, e^{-t/\tau} \tag{42}$$

The pulses were amplified and then given to the inputs of an oscilloscope to monitor the pulses and to a 400 channel pulse height analyzer (see Figure 13).

The sensitivity of the circuit was such that pulses of 0.1 mV could be measured with acceptable signal to noise ratio. This corresponds to a charge Q of 10^6 elementary charges.

(d) Calibration of the circuit was done with a square wave generator of defined amplitude and 1 ms pulse width. The response of the circuit to a constant voltage applied at the probe side is slightly different than that due to a charge deposited.

A short calculation shows that the pulse height of the response remains the same but that the decay time is altered.

If the voltage V_o is applied to the probe side it is

$$V_o = \frac{Q_1}{C_1} + \frac{Q_2}{C_2} , \tag{43}$$

and because V_o = const.

$$\frac{\dot{Q}_1}{C_1} + \frac{\dot{Q}_2}{C_2} = 0 \tag{44}$$

On the other hand, the current is

$$I = I_1 - I_2 = \dot{Q}_1 - \dot{Q}_2 \tag{45}$$

where

$$\frac{Q_2}{C_2} = IR_1 \tag{46}$$

From these two we obtain:

$$\frac{Q_2}{R_1 C_2} = \dot{Q}_1 - \dot{Q}_2 = \frac{C_1}{C_2}\dot{Q}_2 - \dot{Q}_2 \tag{47}$$

which gives

$$\dot{Q}_2 = -\frac{Q_2}{R_1 C_2 (1+\frac{C_1}{C_2})} \tag{48}$$

with the solution

$$Q_2 = Q_{20}\, e^{-t/\tau'} \tag{49}$$

where

$$\tau' = R_1 C_2 (1 + \frac{C_1}{C_2}) \tag{50}$$

The initial charge is

$$Q_{20} = Q_{10} = Q = CU_o = \frac{C_1 C_2}{C_1 + C_2} U_o \tag{51}$$

And therefore the signal at R_1 is

$$U_R = \frac{Q_2}{C_2} = \frac{Q}{C_2} e^{-t/\tau'} = \frac{C_1}{C_1 + C_2} U_o\, e^{-t/\tau'} \tag{52}$$

(e) Measurements of the charge distribution along the axis of the channel where taken at a gas stream velocity of V_o = 55 m/sec. For the stream injection a pressure of 8.0 psig was maintained in the manifold. At higher pressures condensation phenomena in the expanding jet occurred which may be of interest in themselves but were not subject of this investigation. For a particular position of the probe signals were accumulated in the analyzer memory for 60 sec.

The conditions of the jet and the discharge were sufficiently steady over these lengths of time. The discharge voltage was 2.55 KV and the Corona discharge current was between 3 and 5 μA. Fluctuations of this current and spitting at the nozzle exist were not seen to have any influence on the counting rates.

3. Results of The Charge Measurements

Appendix A shows a comprehensive sample of the pulse height analyzer output. Interpretations of the data are given below except for that which refers to the onset of a condensation phenomenon.

(a) To verify that the pulses obtained with the probe and the described network were indeed unstructured pulses due to single droplets carrying the charge and not the integrated response of the probe to some vortex, or eddy type potential distribution carried by the flow past the probe the actual shape of a single signal was photographed. The probe was grounded over a 25K resistance and the signal at these 25K directly given into the oscilloscope. The cable represents a capacitance of 200 PF. (Time constant τ = 5 μs) The signals show a sharp rise to a peak and a exponential decay. (see Appendix A, data of 5 August labelled 24).

The peak does not show any structure. From the resolution we can say that the structure is certainly smaller than 0.5 μs. At a velocity of 50 m/sec this

indicates structures smaller than 2.5×10^{-3} cm. This is much smaller than any expected eddy seizes in this geometry.

We can therefore say with reasonable certainty we are not looking at eddies but at single concentrated accumulations of charge, i.e., droplets.

(b) As result of the measurements on the axis it was found that the distribution of the pulse heights and therefore the distribution of charge has the appearance of a Maxwellian distribution with a steeper slope at the lower and a clearly defined maximum around 1.5×10^{6} elementary charges and a longer tail. The charges correponding to the maximum of the distribution, the half-width of the distribution and the counting rate at the maximum were taken from the analyzer data and plotted in Figures 14 and 15 as function of the probe position on the axis.

The counting rates are corrected for analyzer dead times which the analyzer recorded internally.

As can be seen from Figure 14, the maximum charge near the nozzle exit is 1.8×10^{6} elementary charges and drops to 1.4×10^{6} on the first centimeter. It stays constant for the next 2 cm and then declines further but less steep than on the first drop.

The half width also declines from 3 arbitrary units to one unit on the first and along the axis and stays almost constant from then on (*).

The counting rate increases from 1000 counts/sec near the nozzle to about 1300 counts/sec at a distance of 1 cm. Further out it drops sharply with nearly a $1/r^2$ dependence (see Figures 15 and 16).

Some data taken at positions 1 cm off the axis in general showed the same pattern. The amplitudes were reduced by a factor 2 compared to the amplitudes for the corresponding on-axis positions.

(c) A possible explanation of these observation is that during the first cm after the nozzle exit a fragmentation of some of the droplets occurs.

The simplest assumption of a fission made is a separation into two equal parts from a initial dumbbell type excitation.

Initially the charge average is $\overline{Q}_i$. Let the number density be N.

A percentage P becomes fissioned into droplets each having a charge of $\frac{\overline{Q}_i}{2}$

What is the average charge then?

We have N(1-P) with $\overline{Q}_i$.

(*) 1 unit corresponds to 0.75×10^6 elementary charges.

Average charge final is $\bar{Q}_i$

$$\bar{Q}_f = \frac{N(1-P)\,\bar{Q}_i + 2PN\,\frac{\bar{Q}_i}{2}}{N(1-P) + 2PN} \tag{53}$$

$$= \frac{1}{1+P}\,\bar{Q}_i \tag{54}$$

The measurements show a ratio:

$$\frac{\bar{Q}_f}{\bar{Q}_i} = \frac{1.4}{1.8} \qquad 1 + P = 1.28 \tag{55}$$

$$P = 0.28 \tag{56}$$

The density of particles is expected to be

$$N_f = N(1-P) + 2PN = N(1+P) \tag{57}$$

With N proportional to the counting rate of 1000 counts/sec we could then predict with P = 0.28 a new counting rate of 1280 counts/sec.

This agrees well with the measurement which shows an increase of 20-30% within the first cm.

The half width drops then are consistent with this picture. The distributions show that the drop of the half width is essentially due to decrease of the high charge tail. One would expect that it is the higher charged droplets that are most unstable and tend to fission.

(d) Influences on the distribution from variation of the operating parameters were considered only with respect to change of vapor pressure in the manifold. Decreasing of the vapor pressure resulted in a rapid decrease of the signal.

Increasing the pressure a critical onset of appearance of large charges of the order 10^3e was observed. The distribution was nearly Gaussian and the maximum moves to higher q values with the distance of the probe from the nozzle exit.

The sudden appearance of large charges and the increase of the charges downstream suggests the occurence of a condensation phenomenon (see Figure 17).

Although these large charges are not of immediate interest in the EHD program it may be of interest to use them as a tool to study condensation phenomena in the expanding vapor jet.

B. Proposed Measurement of Droplet Masses

In order to make a model independent determination of q/m and to be able to check the validity of the existing models of the charging mechanism and the resulting charge to mass ratio the droplet masses have to be determined independently.

A survey of the existing small droplet measuring techniques which was made by B. J. Matthews et al and reported in a AFRPL-report[5] lists 7 methods:

1. Electrical or electronic systems
2. Deposition and collection
3. Light scattering
4. Fluorescent photography
5. Streak photography
6. Spark shadowgraph
7. Laser holography

The electrical systems operate with injection of charges on the droplets and a probe technique. These methods make already use of a charge-droplet size model and are therefore useless for the stated purpose here.

The deposition and collection method based on shutters or sieves and a freezing out technique. Besides being very cumbersome and not very convenient for large droplet numbers the possibility of coalescence on the collector makes it uncertain whether the measured droplet sizes are representative.

The light scattering is a definite possibility. It does not give a droplet seize distribution but the Sauter-Mean-diameter which would be an important information.

Limitations of this method due to sensitivity to changes in the surrounding medium and that it is not well applicable to rapidly evaporating droplets are of less concern in the EHD application than they would be in rocket engine.

Fluorescent photography with the use of Q-switched laser as light source has been used by some investigators but there were strong indications that in order to obtain fluorescence the laser energy has to be such that it has distorting effects on the droplet seize, even leads to vaporization.

Streak photography must be ruled out because the streaks are normally rather fuzzy on the film plate and it is difficult to assign a size to the trace. Also it is difficult to single out traces.

Spark shadow-graphs are obtained by high intensity arc flashes or laser flash lights which illuminate the test scene for short enough

time to eliminate effects from the motion. The droplets produce shadows on the recording film and their size can be determined with good accurracy. This technique has been used and droplet sizes down to 10 μ have been measured by investigators.

Laser holography is a very wide ranging technique with large possibilities. However the basic questions regarding the resolution and the data reduction are not solved. Employment of this powerful technique requires additional development.*

From this brief summary it appears that for purposes at hand the light scattering and the spark shadowgraph technique will be the appropriate choice. The light scattering will provide a mean diameter. The shadowgraph technique will allow the determination of the size distribution and the two techniques should coroborate each other.

---

*See Part V of this report.

IV. DISCUSSION AND CONCLUSIONS

A comparison between the hot wire anemometer data and the EHD probe data shows a deficiency in the high frequency output of the latter. Such a deficiency has been translated into a size distribution which is devoid of particles below 10^{-6}m. This seems consistent with the interpretation of results of charge distribution. If we ignored the contribution of turbulence in Equation 22, we could conclude that the representative particle radius is about 10^{-4}m, and this is also consistent with the results of Part III since the diffusion charging limit for the above radius is about 10^{8} electrons (see Figures 4 and 17). But, beyond the above, there appear to be significant differences between the two types of measurements.

The spectral analysis is expected to be good for small levels of turbulence since only a first order perturbation was used. The neglect of pressure forces is reasonable because the actual pressure drop is much less than one atmosphere per meter and hence there is very little effect on small particles. The use of Stoke's draf law underestimates the drag particularly for radii of the order of 10^{-4}m and this signifies that τ_v is smaller for a given mass or radius; the difference, however, is not expected to bridge the gap of the predicted mean radius as given by the two methods. The assumed time dependance of the spectral measurements is, again, derivable only if the level of the fluctuations is small.

On the other hand, the charge distribution measurements leave some open questions. The asymmetry of the curves shown in Appendix A is attributable to the increased charging with radius; as shown in

Figure 4, this charging is proportional to the 1.5 power of the radius for the stability limit of a droplet (Rayleigh limit). A quick calculation (quick because no correction was made of the shift of the maximum of the curve) showed that the exponent of the radius that causes the asymmetry must be greater than 2.0 and in an increasing way. One is thus tempted to postulate that the pulses arise not from single particles but from "clusters" which show a remarkable cohesion. The dilemma is presently unresolved and a more direct measurement of size distribution will be needed.

Turning now to the implications on the injector of the particle size measurements, we can say that the particles appear to be much larger than optimum. That is, the travel time through the corona seems to be much too long and it seems desirable to either reduce the size of the nozzle or to increase the degree of superheat, or both. We have noticed dramatic but as yet irreproducible effects attributable to the degree saturation of the steam entering the cylinder and to the relative humidity of the air. If the steam is too dry, the corona discharge will not work; if the relative humidity of the air is greater than about 30% the particles continue to grow after their injection into the air stream. We have no experience with relative humidities less than 15%. It is, therefore, clear that the resolution of these queries will require further work with more refined instrumentation.

V. NEW RESEARCH

In addition to continuing to study the fluid dynamic diagnostic use of the EHD probe with the present injector system several new items will be undertaken. First of all, a small nozzle is under construction and the accuracy and control of the degree of saturation of the steam and of the relative humidity of the air will be improved. Next, laser holograms of the present nozzle output will be taken and if, indeed, the particles are above 2.2×10^{-6} m in radius then we should be able to photograph them with this technique.

We now envision building a new type of injector which would consist of a corona discharge in the main air flow which would be supersaturated. The turbulence would be generated by wire grids so that it would be truly turbulent and more or less homogeneous. If it looks promising, we may also try an EHD spraying injector[6]. The space change in the conversion region will be analyzed so that shields may be placed in the flow and the output currents may be thereby increased[7].

VI. RECOMMENDATION

Attention is invited to the fact that the theoretical phase of the present research has succeeded in producing a mathematical model which can be used to study the performance of EHD systems by numerical simulation on a digital computer, but that cuts in funding are now forcing the discontinuance of this promising line of attack. In view of the potential value of this work, it is strongly recommended that the question of funding it be carefully reviewed by the Naval Air Systems Command.

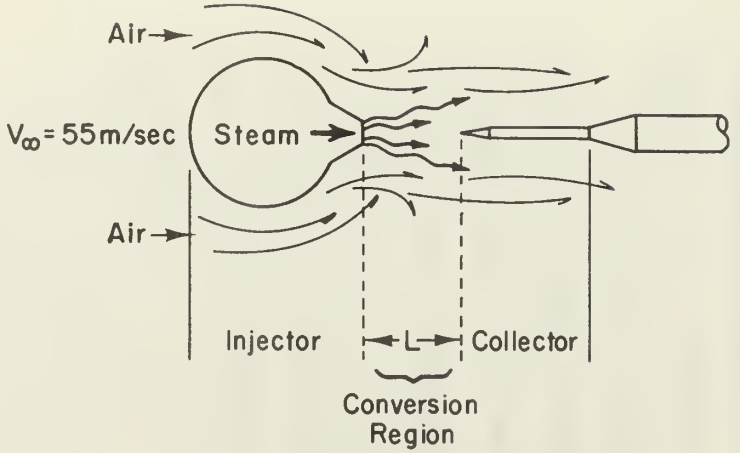

FIGURE I EHD PROBE DIAGRAM

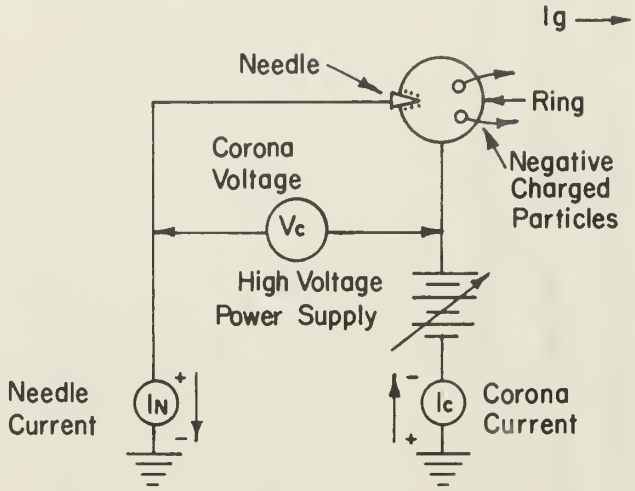

FIGURE Ia. ELECTRICAL SCHEMATIC OF INJECTOR

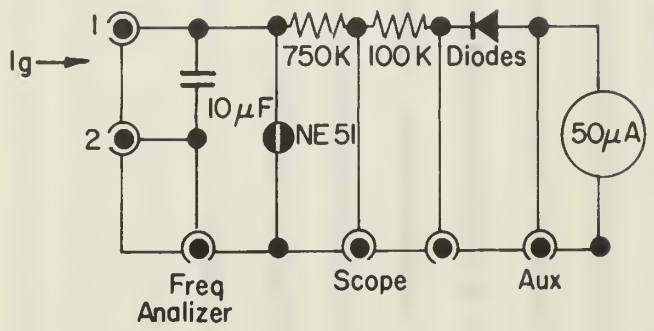

FIGURE Ib. ELECTRICAL SCHEMATIC OF COLLECTOR

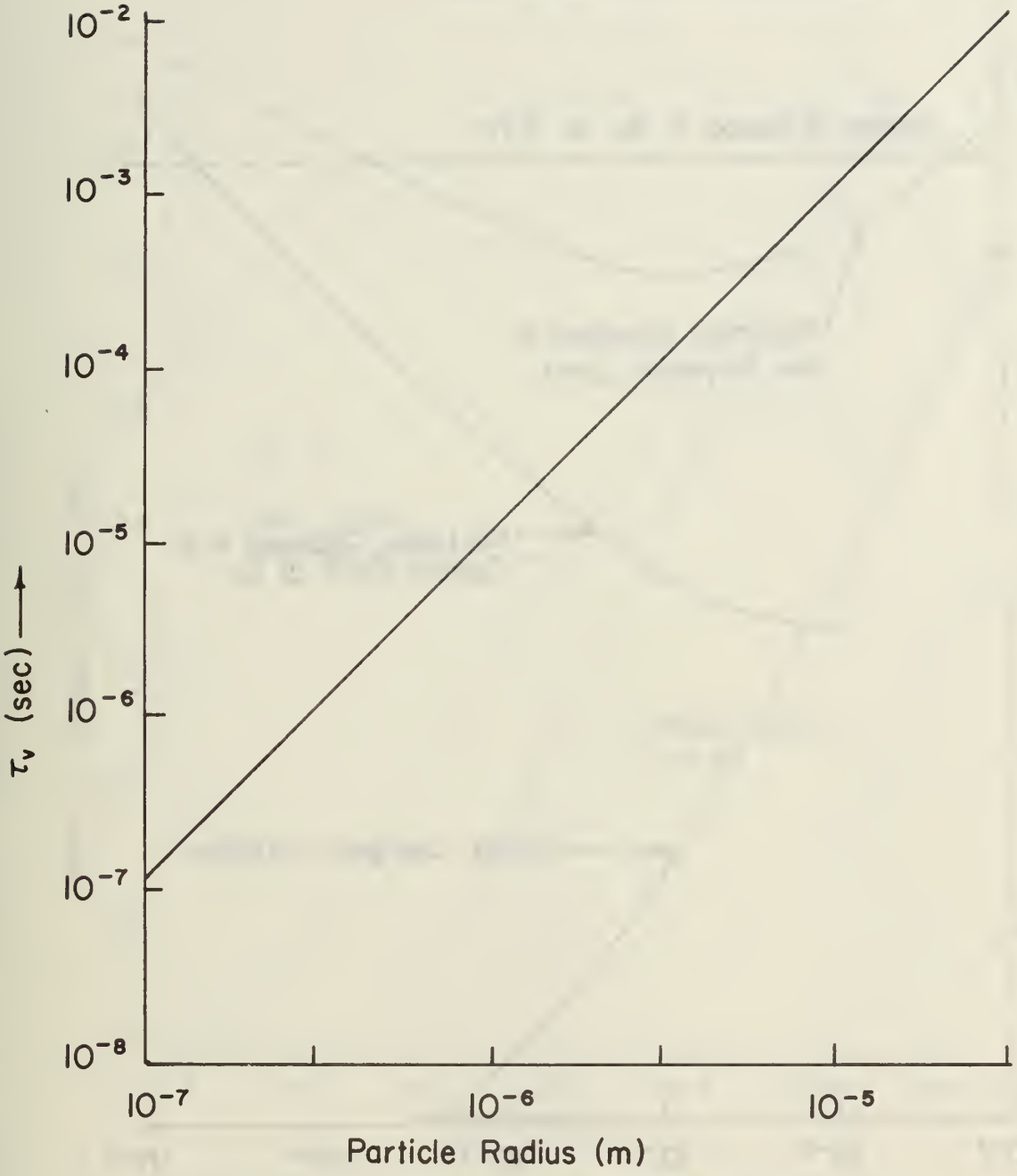

FIGURE 2. EQUILIBRATION TIME FOR SPHERICAL WATER DROPLETS AT STANDARD CONDITIONS

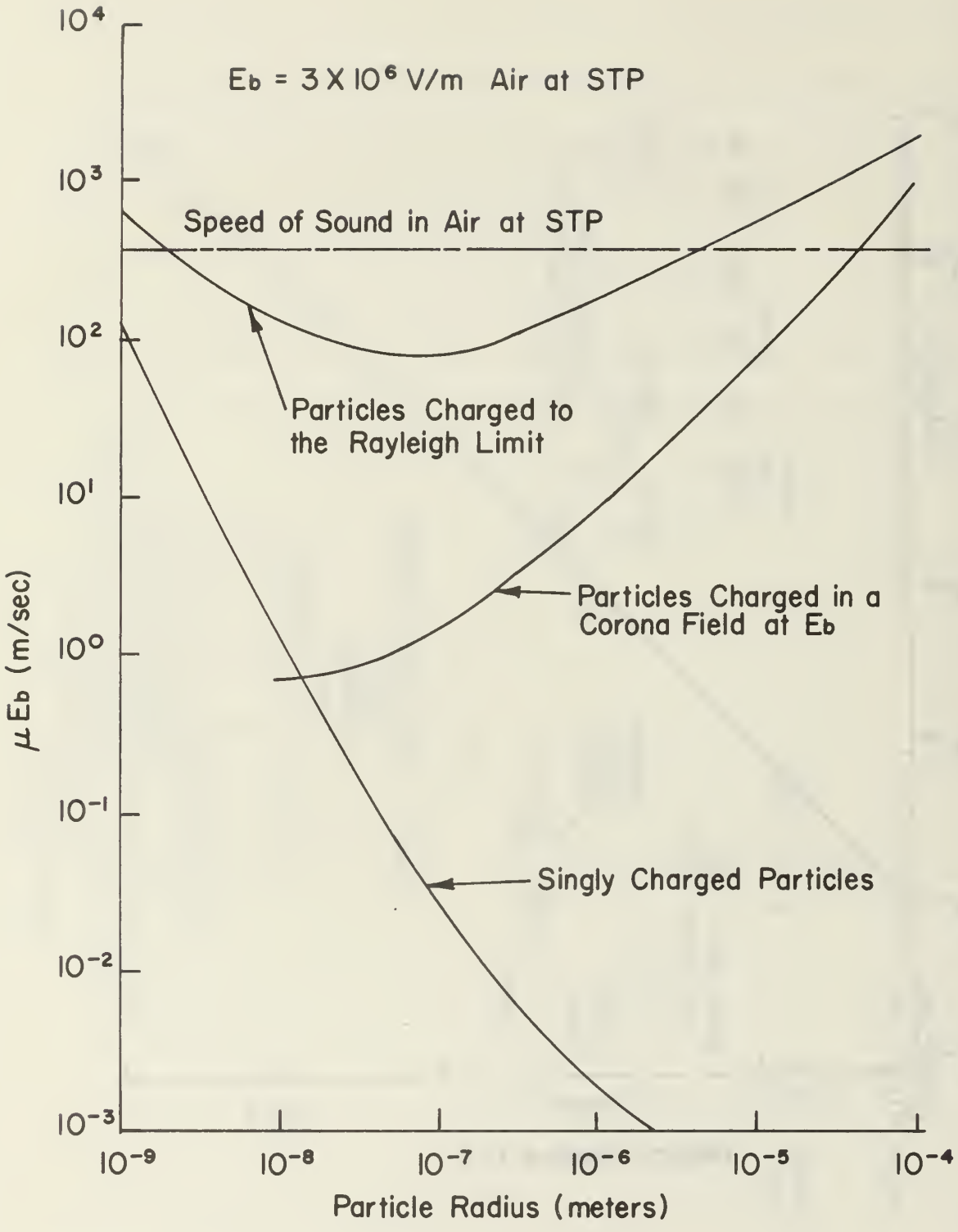

FIGURE 3. MAXIMUM DRIFT DUE TO ELECTRIC FIELD FOR WATER DROPLETS IN AIR AT 1-ATM AND 20°C

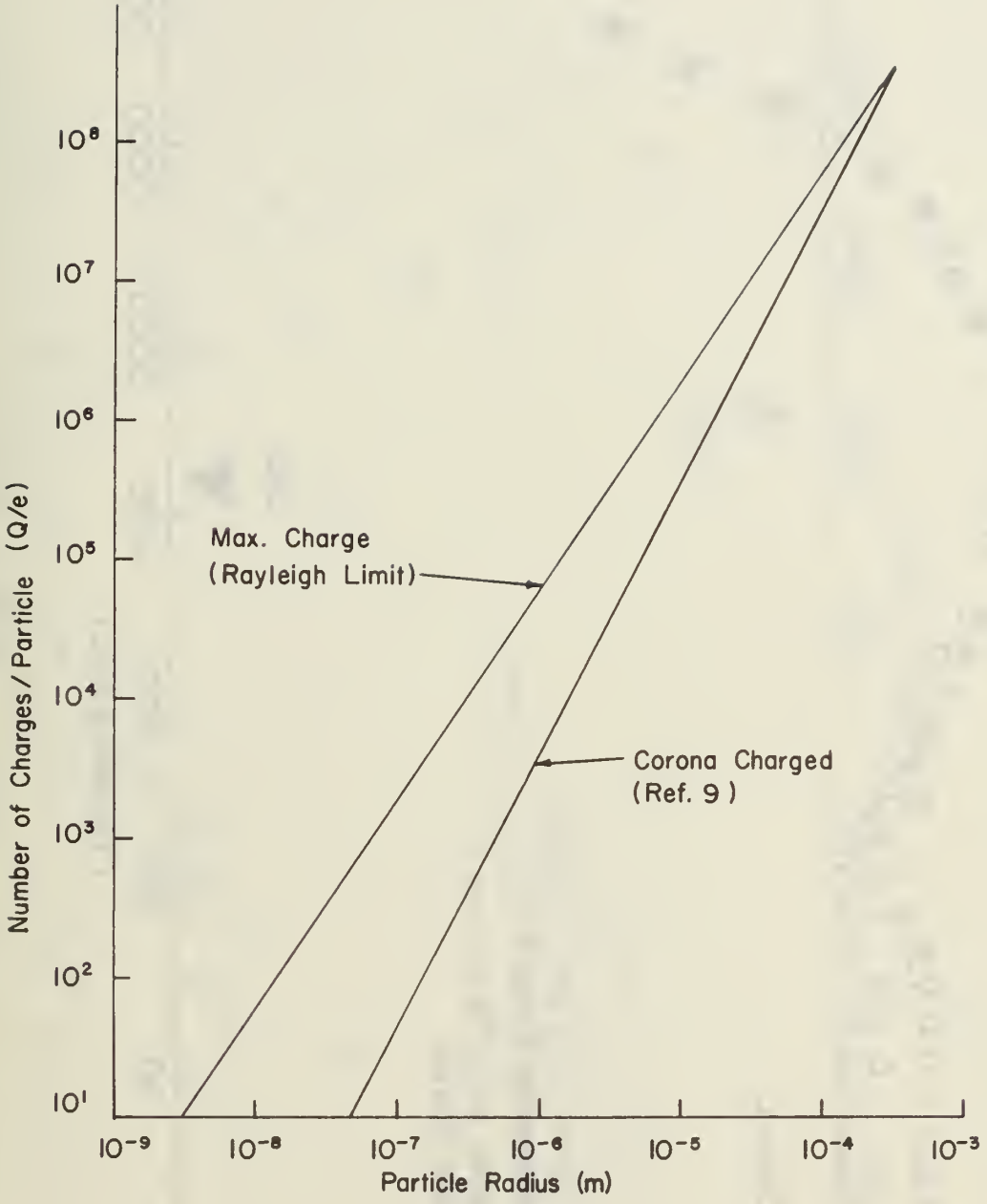

FIGURE 4. CHARGING OF DROPLETS AS A FUNCTION OF THE RADIUS

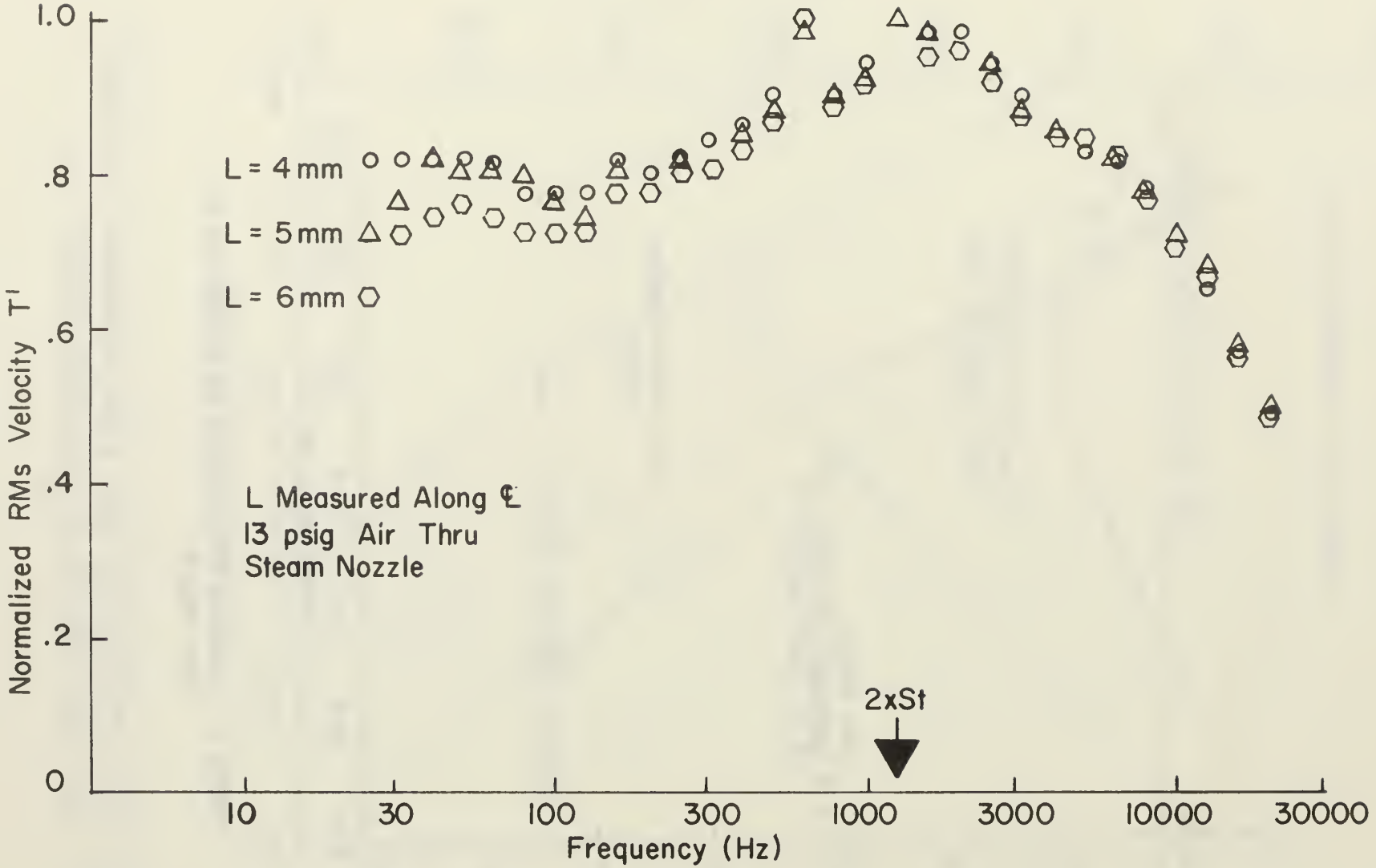

FIGURE 5. HOT-WIRE ANEMOMETER READINGS

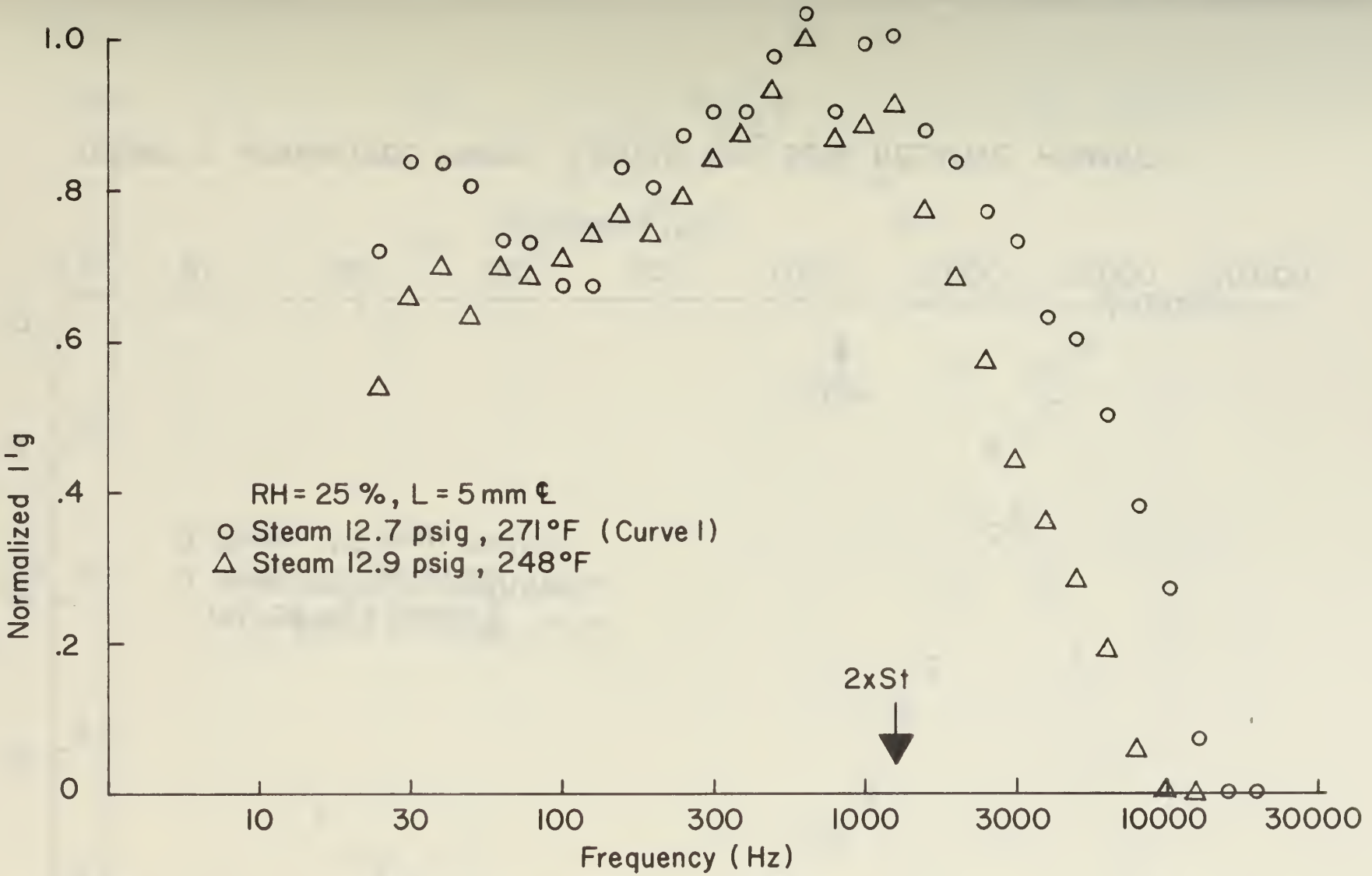

FIGURE 6. NORMALIZED PROBE CURRENT FOR 25 % HUMIDITY

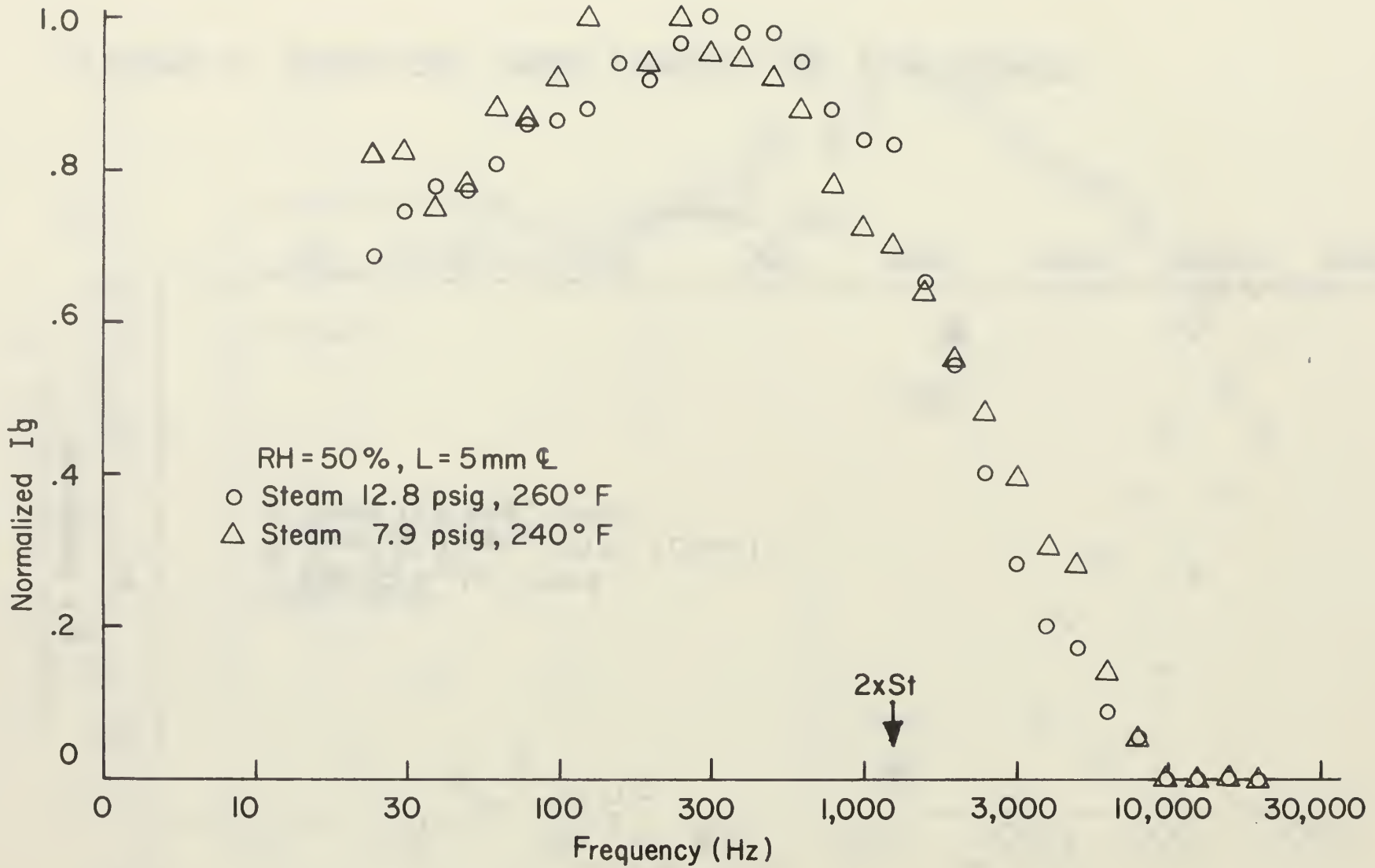

FIGURE 7. NORMALIZED PROBE CURRENT FOR 50% RELATIVE HUMIDITY

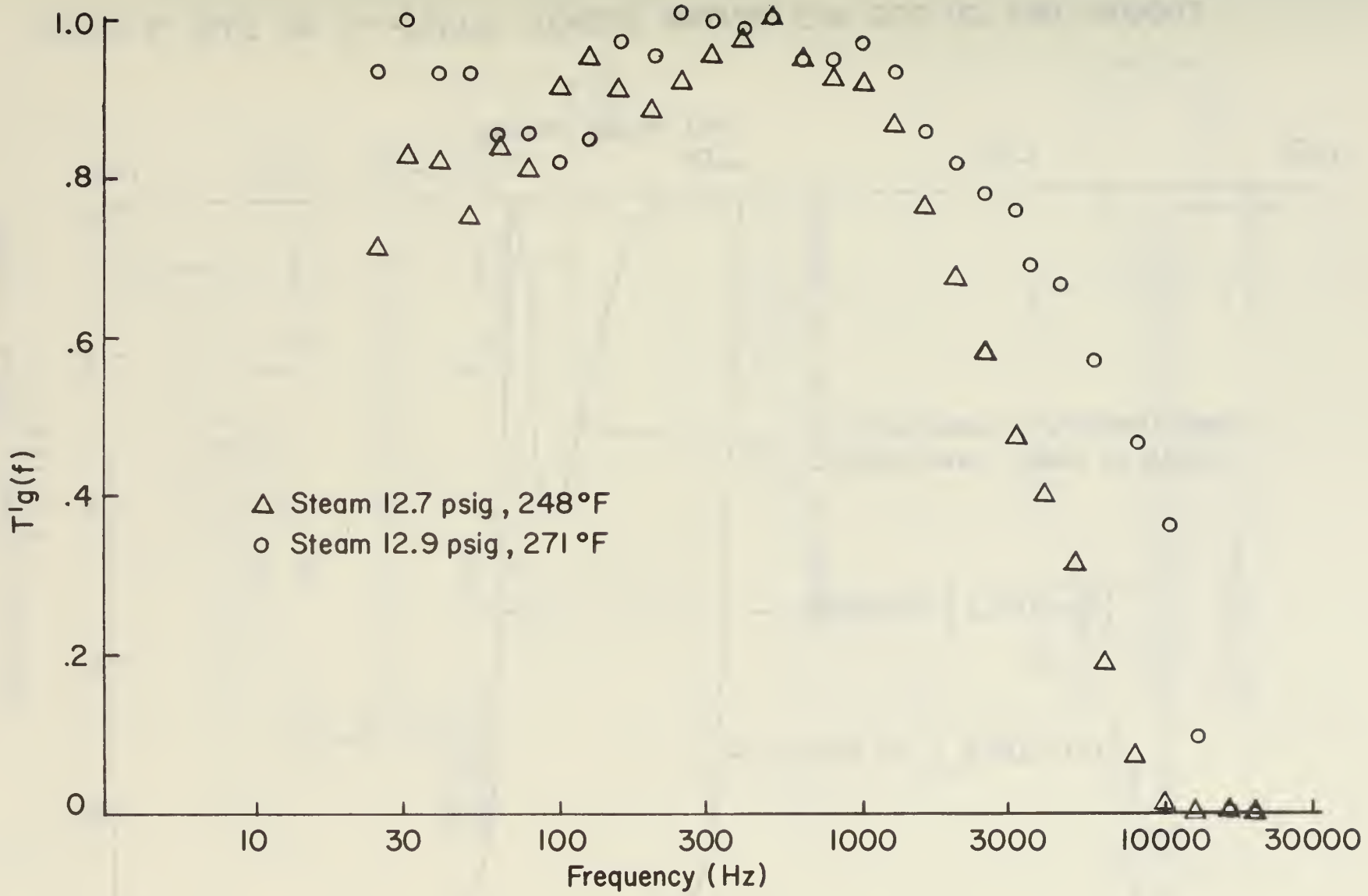

FIGURE 8. NORMALIZED RATIO OF COLLECTOR CURRENT TO RMS VELOCITY

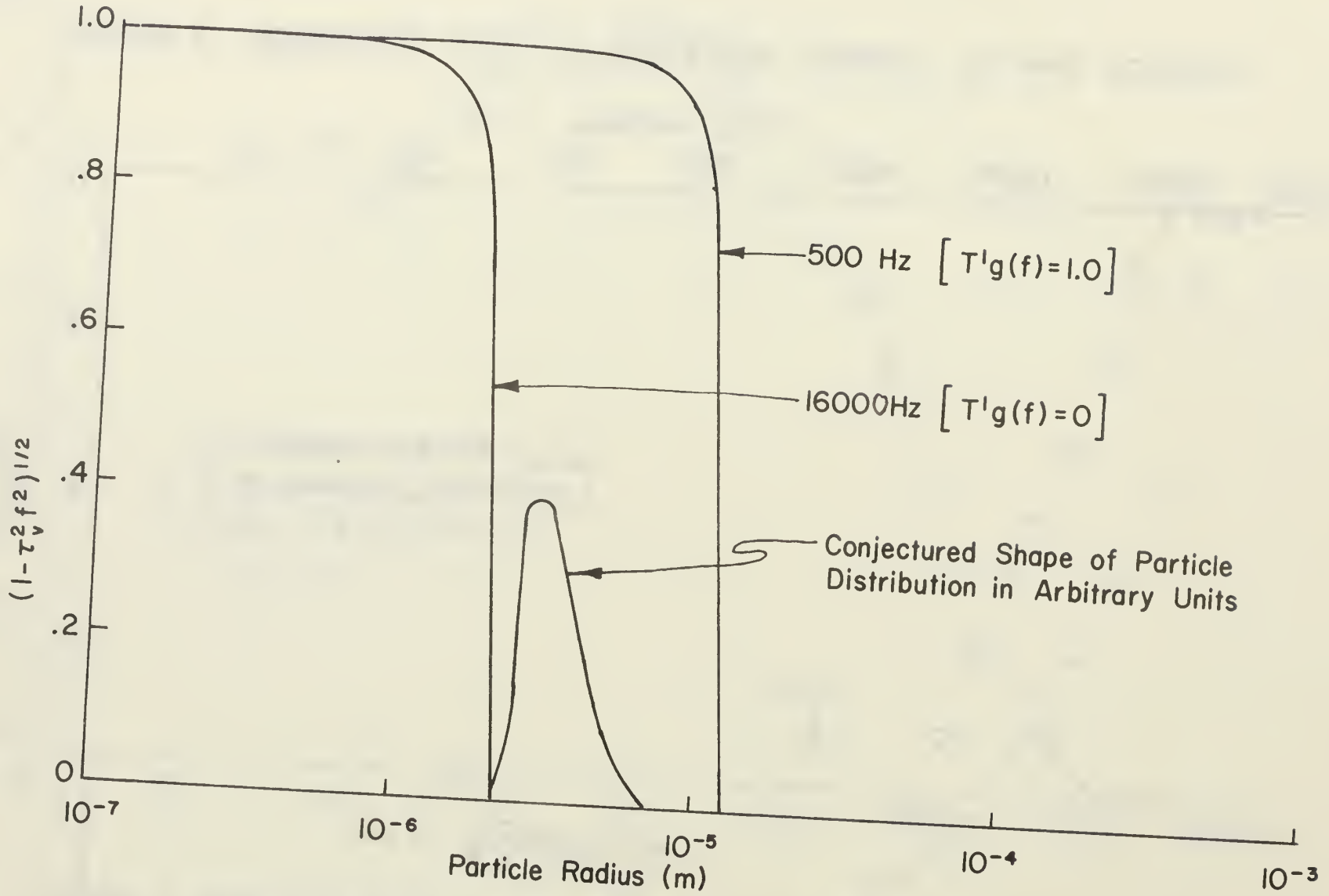

FIGURE 9. PLOT OF $(1-\tau_v^2 f^2)^{1/2}$ VERSUS RADIUS FOR 500 HZ AND 16000HZ

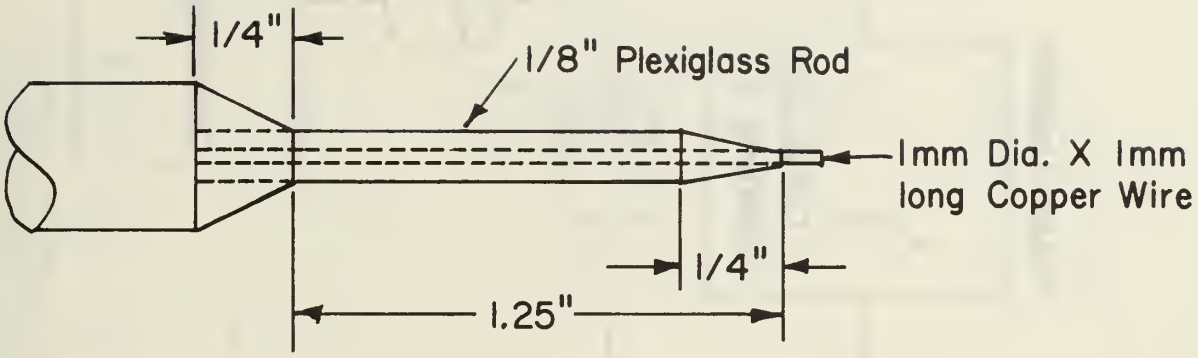

FIGURE 10. DETAIL OF PROBE

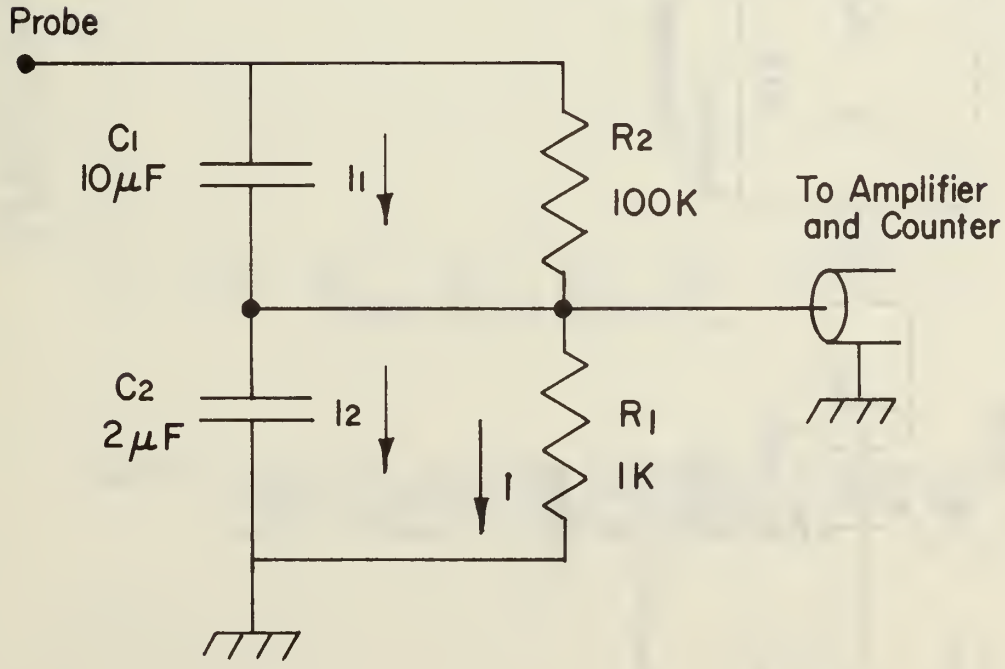

FIGURE 11. PULSE FORMING NETWORK

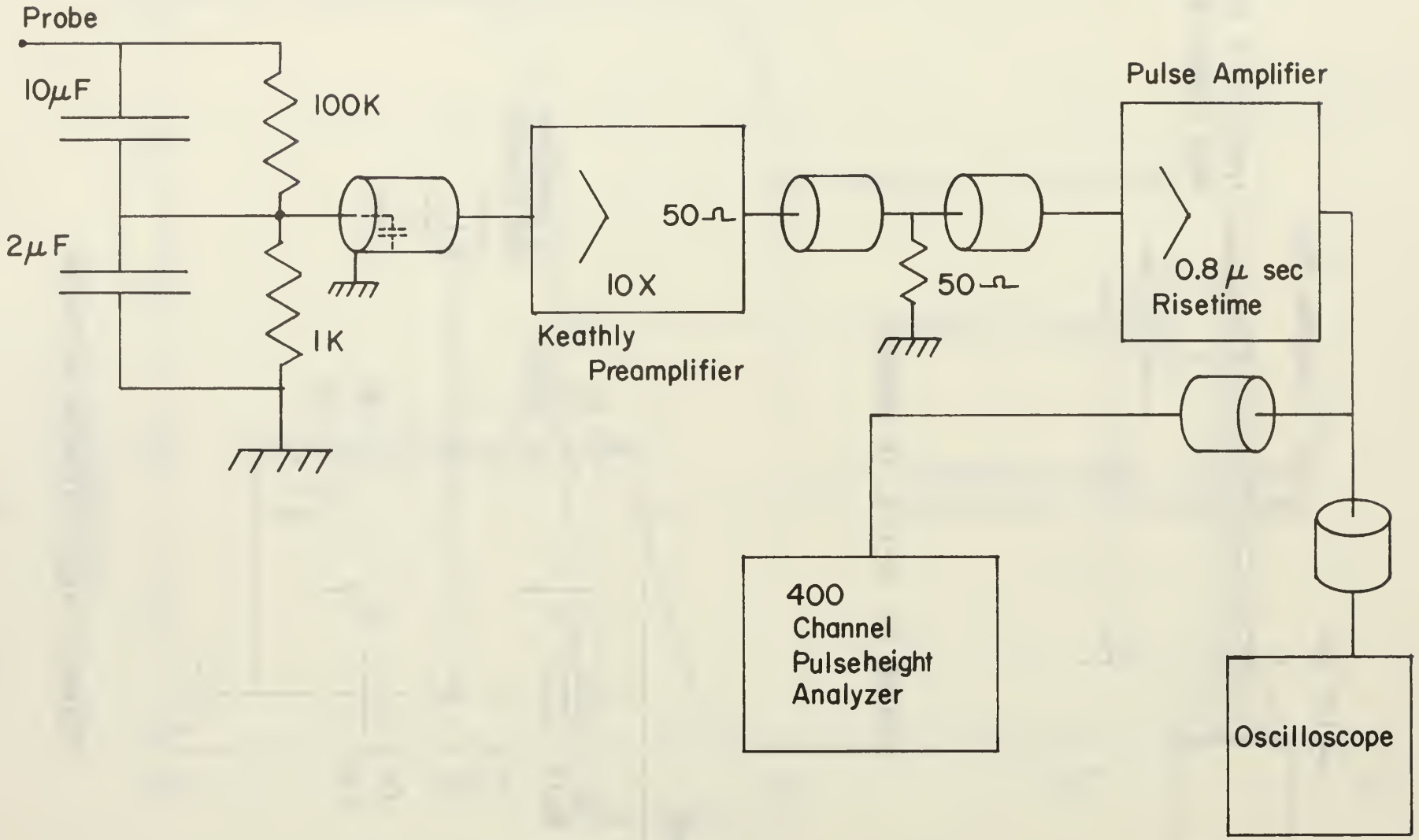

FIGURE 12. COMPLETE INSTRUMENTATION

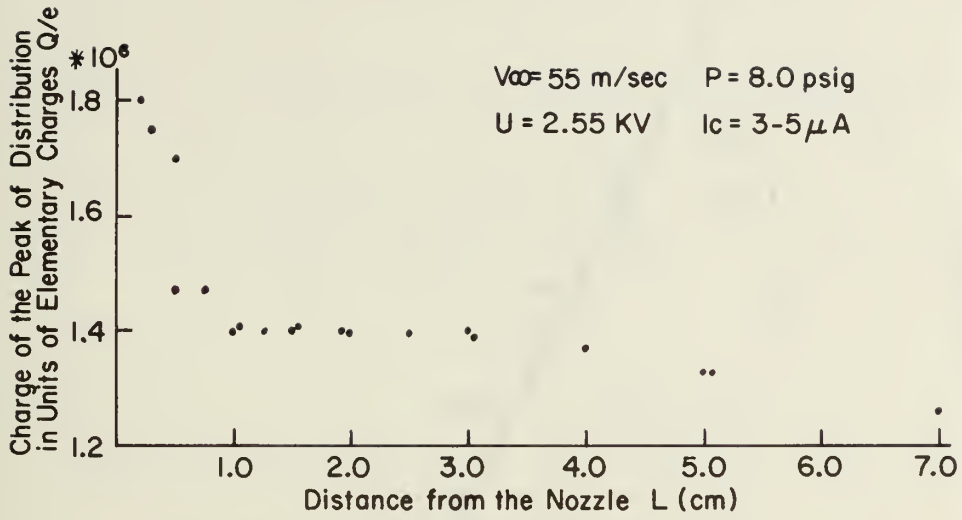

FIGURE 13. MAXIMUM CHARGE OF THE DISTRIBUTION IN UNITS OF ELEMENTARY CHARGES VS DISTANCE FROM THE NOZZLE EXIT ON THE AXIS AT NORMAL OPERATING CONDITIONS

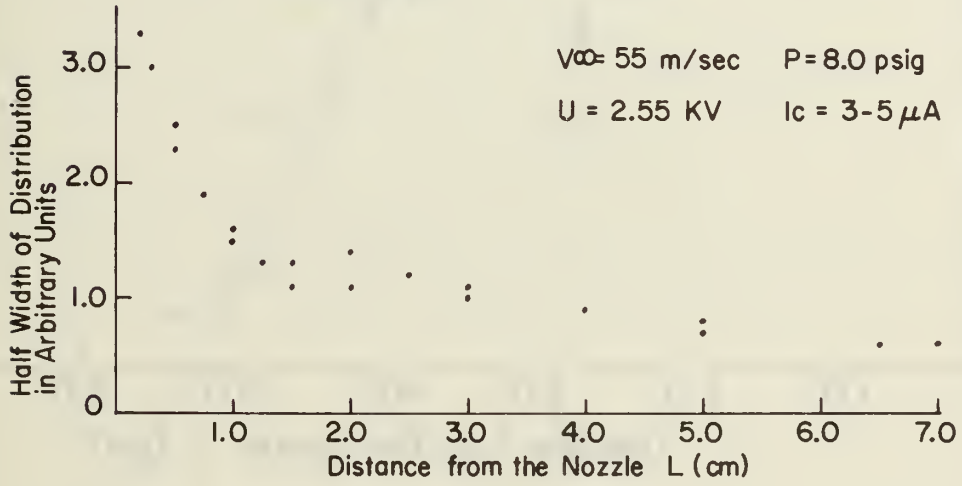

FIGURE 14. HALF WIDTH OF CHARGE DISTRIBUTION IN ARBITRARY UNITS VS DISTANCE FROM THE NOZZLE EXIT ON THE AXIS AT NORMAL OPERATING CONDITIONS

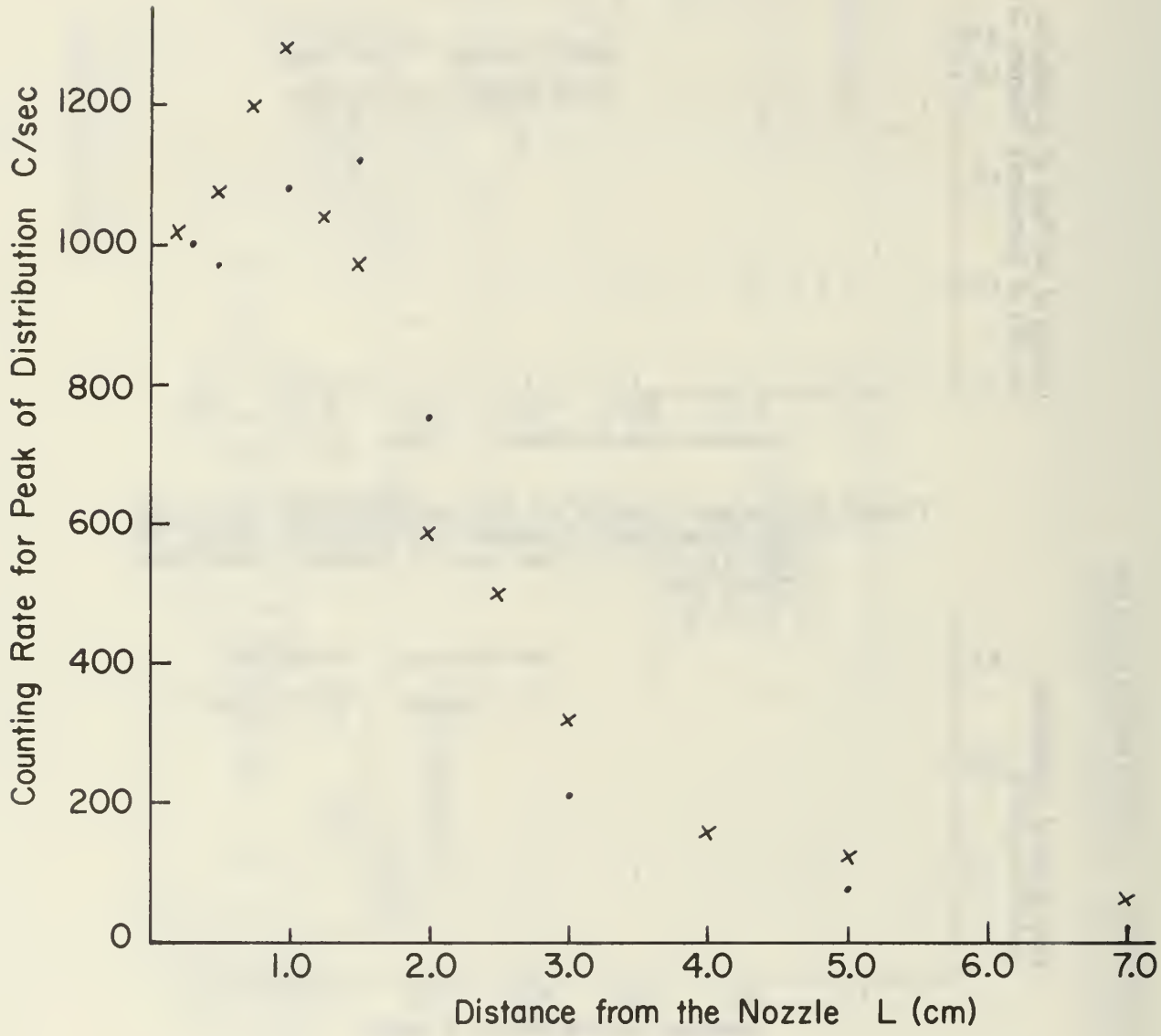

FIGURE 15. COUNTING RATE VERSUS DISTANCE

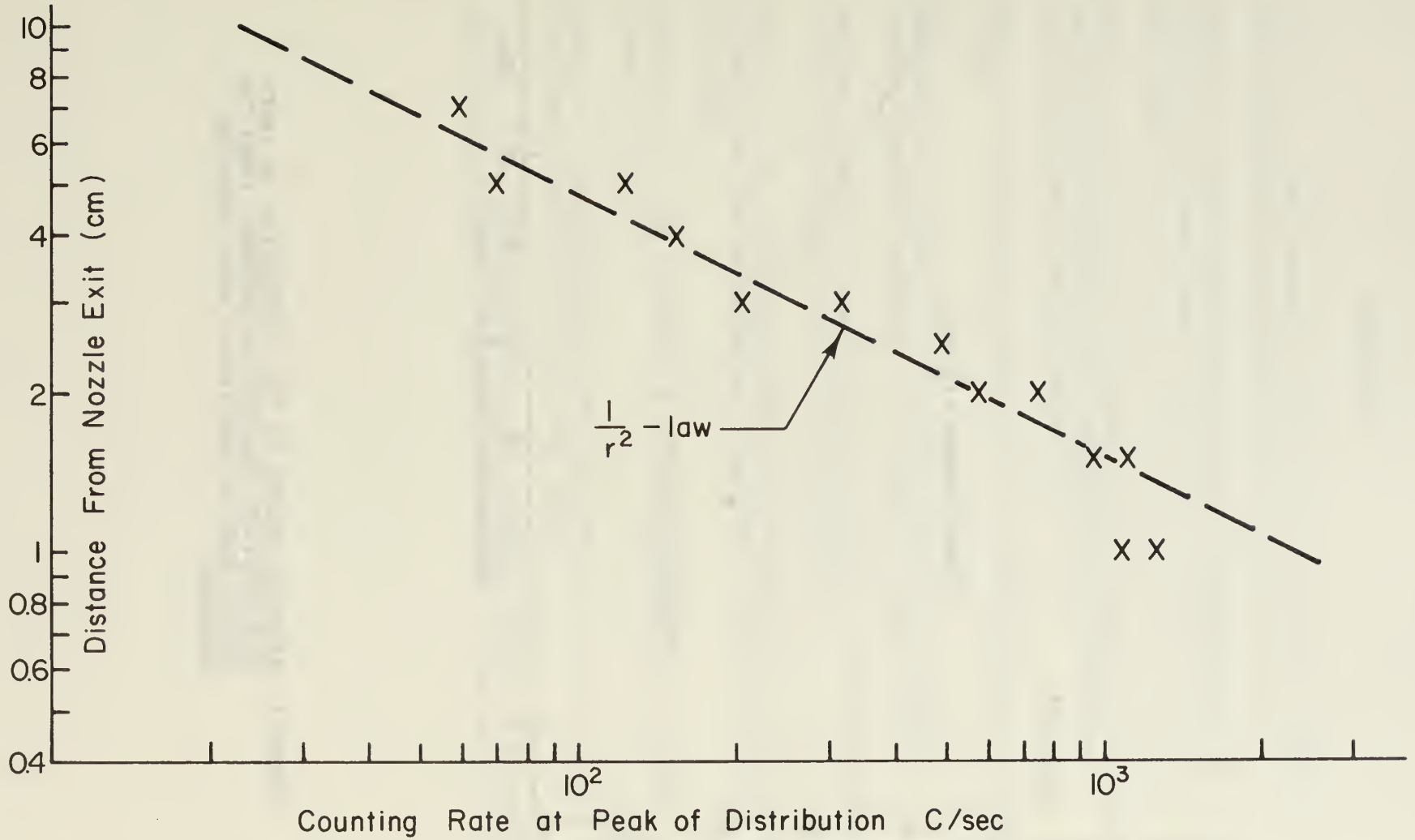

FIGURE 16 r^{-2} DEPENDANCE OF THE DROP FROM FIGURE 15

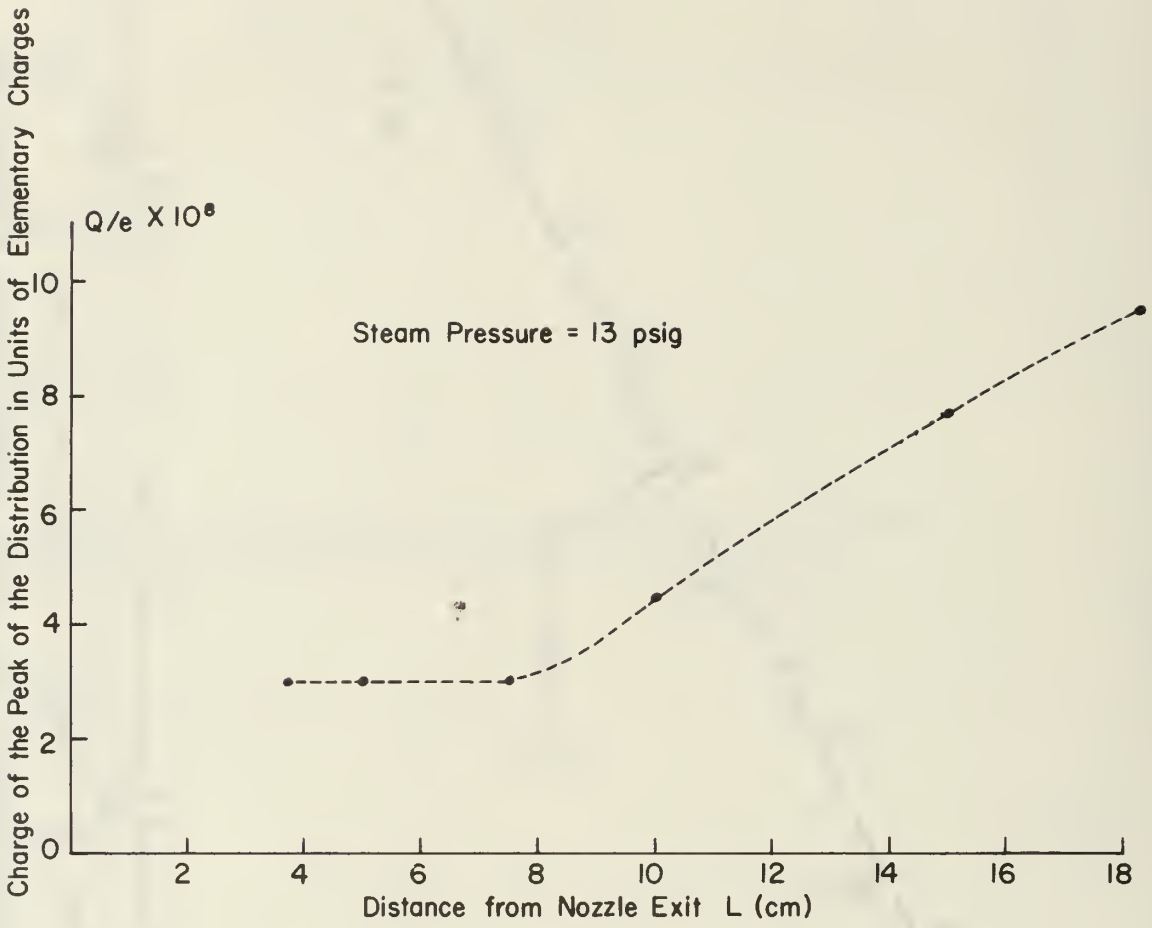

FIGURE 17 MAXIMUM CHARGE OF THE DISTRIBUTION IN UNITS OF ELEMENTARY CHARGES VS DISTANCE FROM THE NOZZLE EXIT ON THE AXIS AT HIGH OPERATING PRESSURE.

REFERENCES

1. Biblarz, O., "EHD Research - Final Report for the Year 1968-69," Naval Postgraduate School Report NPS-57ZI912IA, Dec. 1969.

2. Biblarz, O., "Electrohydrodynamic Flows and Some Effects of Turbulence on these Flows," ENERGY 70 Conference, Las Vegas, Sept. 1970.

3. Biblarz, O., "Analysis of Optimum Charged Particle Size Based on the Conversion Efficiency of Electrogasdynamic Generators," (to be published in Energy Conversion).

4. Marks, A. M., Barreto, E., and Chu, C. K., AIAA Journal 2, 45 (1964).

5. Matthews, B. J., Wuerker, R. F., and Harrje, D. T., "Small Droplet Measuring Technique," AFRPL-TR-67-295, Feb. 1968.

6. Shelton, H., et al, "Electrostatic Acceleration of Microparticles to Hypervelocities," J.A.P., 31, 1243 (1960).

7. Minardi, J. E., "Computer Program for the Calculation of Electric Fields in an Electrofluiddynamic Generator," Report ARL 68-0156 (Aug. 1968).

8. Landau, L. D., and Lifshitz, E. M., Fluid Mechanics, Pergamon Press (1959), p. 103.

9. Kahn, B., "A Continuation of the Basic Study of Slender Channel Electrogasdynamics," ARL 65-4 (Jan. 1965).

10. Lawson, M. and Wattendorf, F. (Ed), "Selected Topics in Electrofluiddynamic Energy Conversion," AGARDograph 122 (December 1968).

APPENDIX A

Pulse Height Analyzer Data

The data incorporated here are actual data taken in the laboratory.

The pages labeled 7, 28, are the calibrations in which signals of known amplitude were fed into the probe. The value of A gives the amplification factor in arbitrary units. The values marked at the abscissa are the corresponding signal amplitudes in mV.

The pages labeled 8-9 contain data at the higher steam pressure. The probe position is indicated as (distance from nozzle; distance from axis; azimut of position) or when on the axis by L = cm from nozzle. The note Ch 0-100 means the picture has the first 100 channels on full scale.

The pages labeled 20-21 give measurements at high pressure with the gas flow turned off. The counting rates clearly indicate the existence of a condensation along the axis.

The pages labeled 26-29 show the onset of condensation measured by the sudden increase of counting rate at a fixed position on the axis at a critical manifold pressure of near 8.3 psig.

The pages labeled 57, 58, 62, 63, 67, 68, 69, 70 give the measurements of the distribution on the axis at different positions, with the gas flow off and on at the low steam pressure.

29 July 70

Calibrations

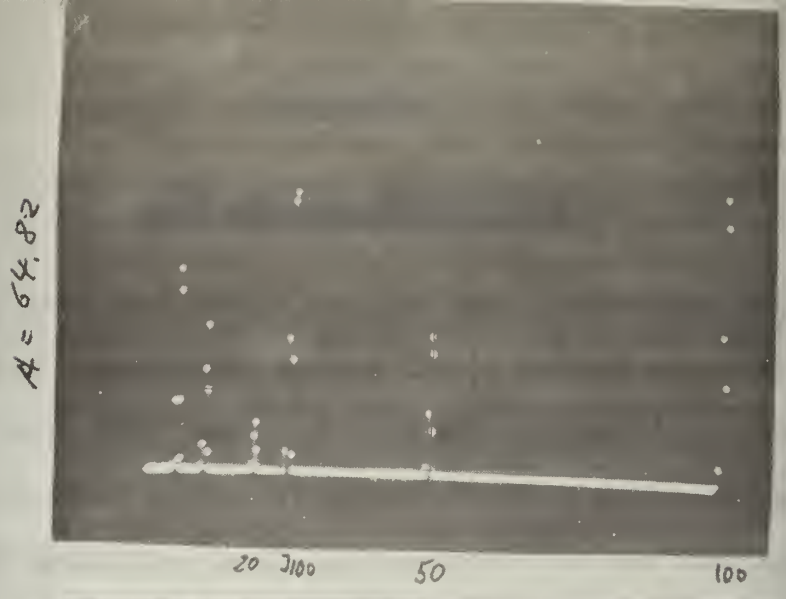

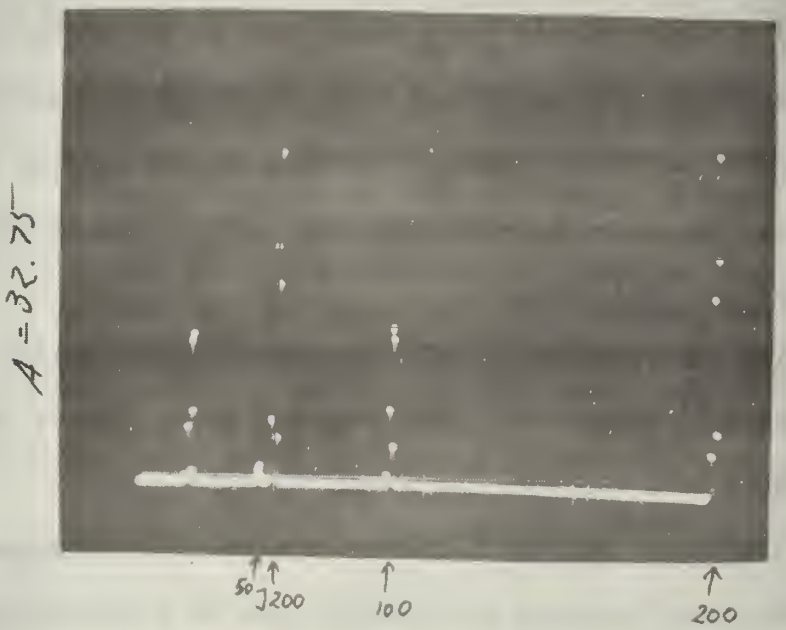

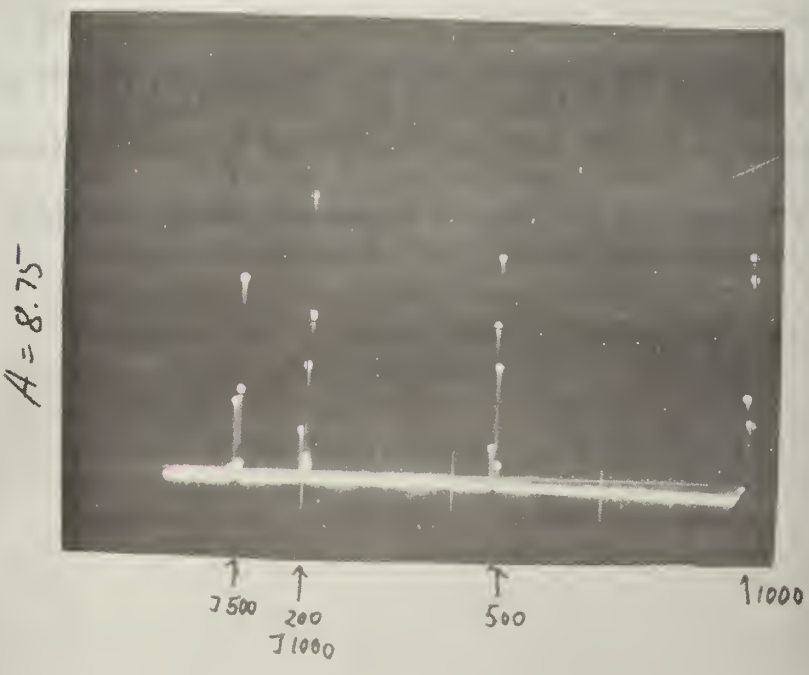

(7)

Variation with Probe Position in Pressurizer

29 July 70

Steam: 11.2 psig
A = 64.82
Countingtime 60s.
Fullscale 4000

(9)

Probe:
(3.75, 0 -)

(7)

Probe:
(5, 0 -)

(8)

Probe:
(7.5, 0 -)

(8)

Variation with Probe Distance from Nozzle

29 July 70

Steam: 11.2 psig
A = 64.82
Counting 60 sec.

(10)

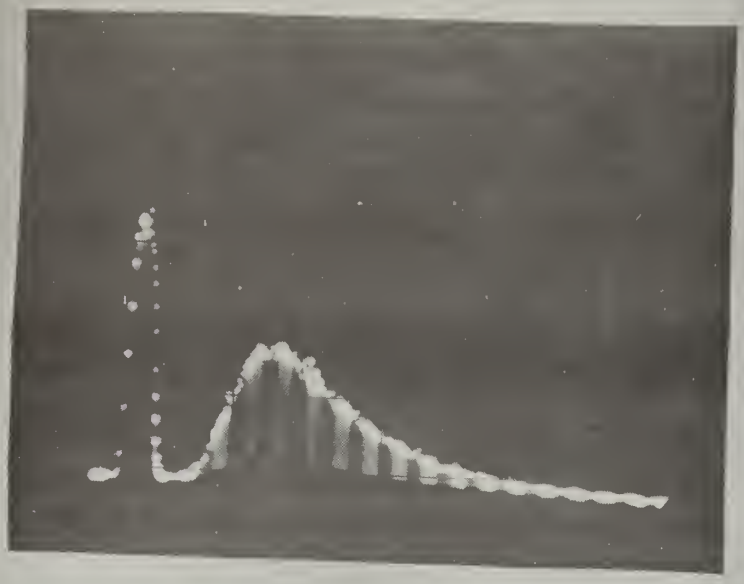

Probe
(10, 0 -)

(11)

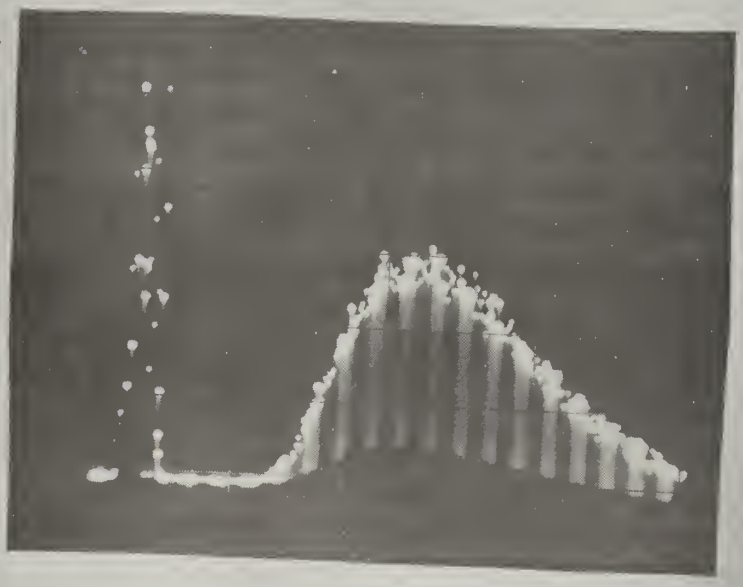

Probe:
(15 0 -)

(12)

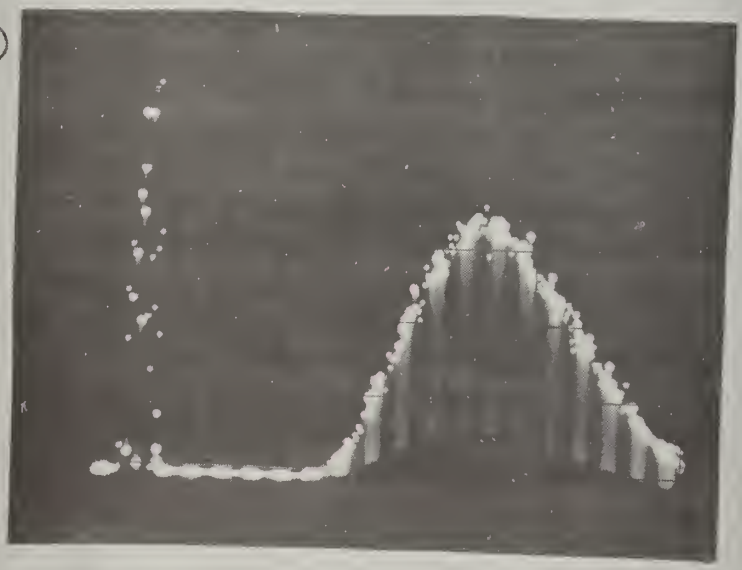

Probe:
(18.5, 0 -)

(9)

Dependence on Distance from Nozzle

5 August 1970
A = 64.82
No gas flow
Steam: 11.0 psig
Probe on axis
L = distance from nozzle

(5)

L = 1.9 cm

↑ 0.2 v/cm

(6)

L = 2.5 cm

(8)

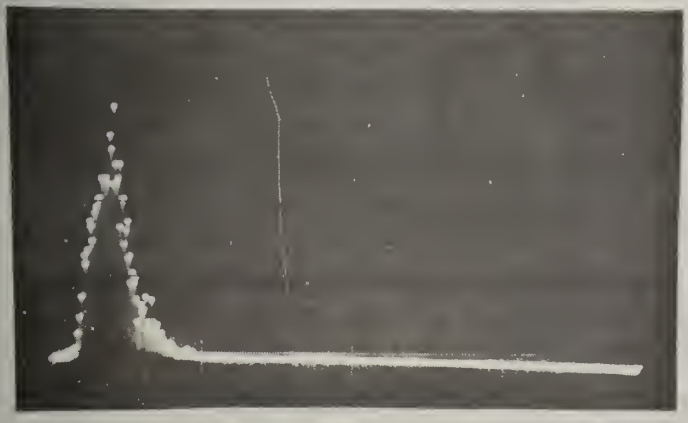

L = 3.1 cm

L = 3.8 cm

(7)

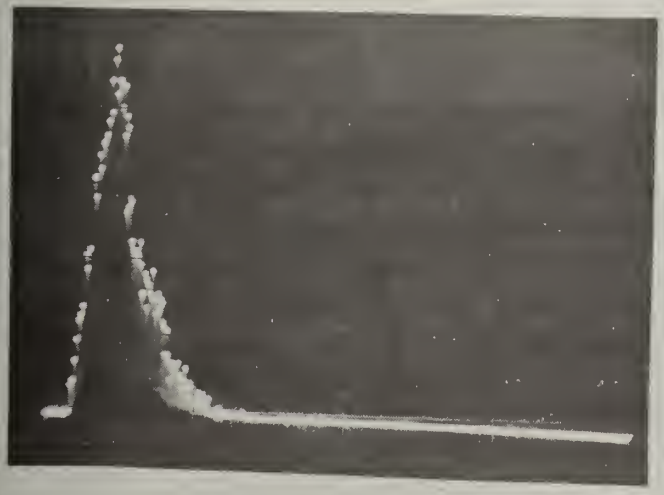

(9)

5 August 1970

A = 64.82
No gas flow
Steam: 11.1 psig
Probe on axis
22 c/sec cm

(10)

L = 5.0 cm

↑ 22 c/sec cm

(11)

L = 7.5 cm

(12)

L = 10 cm

(13)

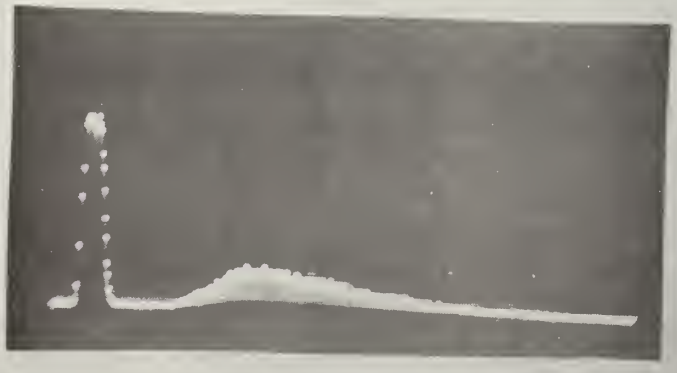

L = 12.5 cm

Real Pulse Shape

5 August 1970

(19)

Multiple trace Auto trigger

5 ms/cm

↑ 0.2 V/cm

Probe at L = 3.8 cm

(20)

5 ms/cm

↑ 0.2 V/cm

Probe at L = 7.5 cm

(21)

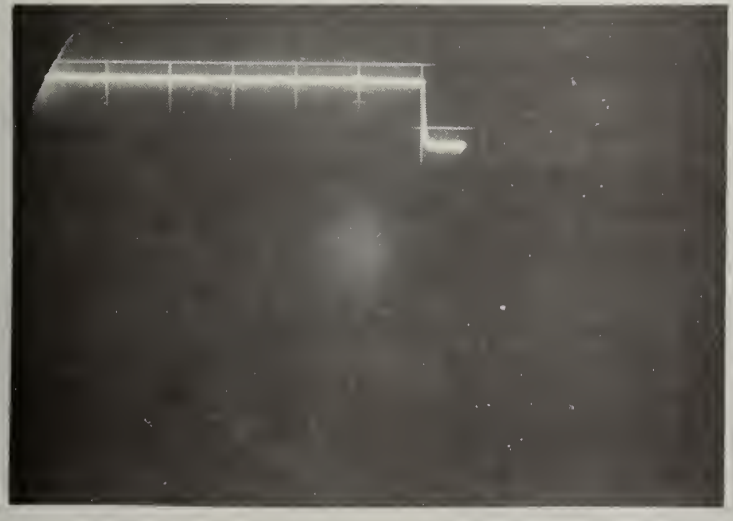

50 ms/cm

Square wave 0.2 V

↑ 0.2 V/cm.

The skip couldnot be brought on the scope for faster sweep.

the circuit time constant is smaller than 5 ms

(24)

6 August 1970

Determine Onset of Condensation
No gas flow
A = 64.82
Probe L = 5 cm

(9)

0.28 C/sec cm

P = 8.0

(10)

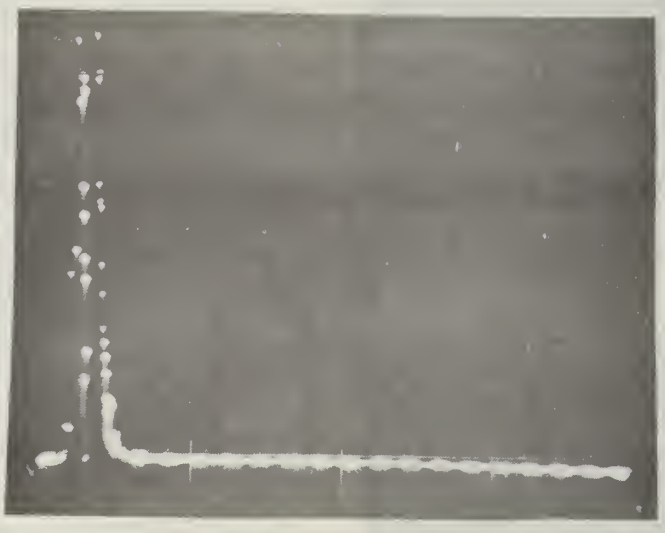

8.3 C/sec cm

P = 8.3

(11)

83 C/sec cm

P = 8.5

(12)

83 C/sec cm

P = 8.8

Determine Count of Contamination

6 August 1970

No gas flow
A = 64.82
Probe L = 5 cm

(13)

8.3 c/sec cm

P= 8.25

(14)

8.3 c/sec cm

P= 8.3

(15)

8.3 c/sec cm

P= 8.5

6 August 1970

Calibration:

A = 64.65

(28)

Onset of Condensation

6 August 1970

No gas flow
A = 64.99
Probe L = 5 cm

(16)

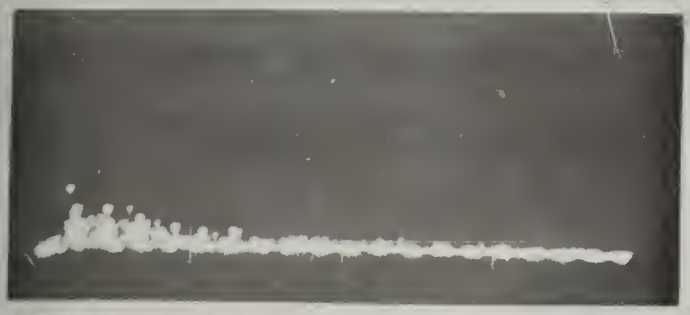

0.55 c/sec 6 cm

P= 8.2

(17)

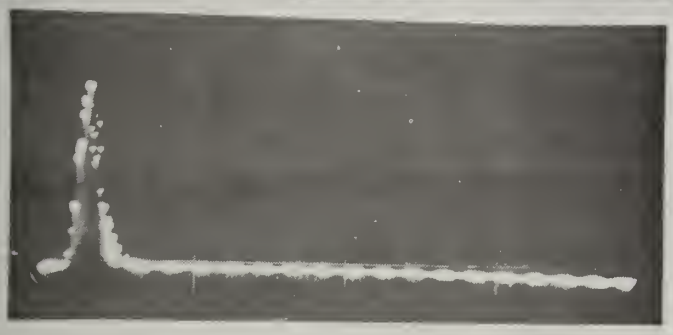

3.3 c/sec cm

P= 8.25

(18)

3.3 c/sec cm

P= 8.3

(19)

8.3 c/sec cm

P= 8.3 +

(20)

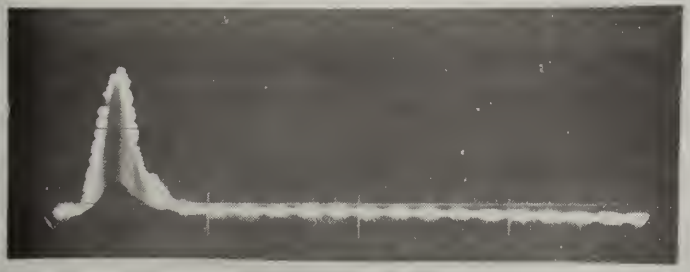

83 c/sec cm

P = 8.5

(29)

19 August 1970

Position Dependence of Spectrum

P = 8.0 psig
Countingtime 90 sec.

①

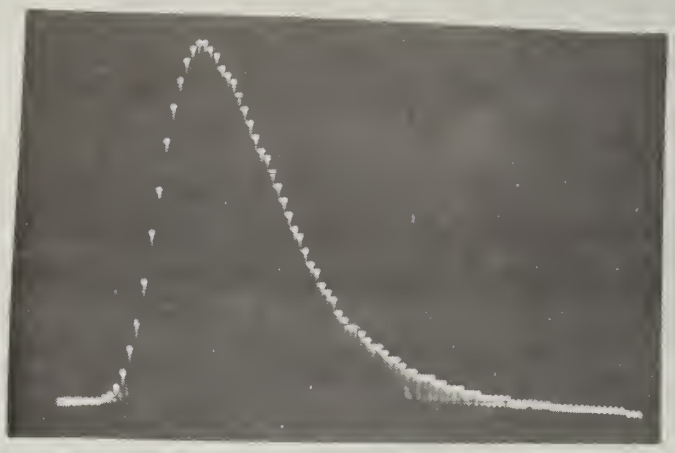

No Gas flow

L=0.5 cm
A - 32.82
Ch 0 - 100
1.6×10^4 c/cm

Gas flow on

③

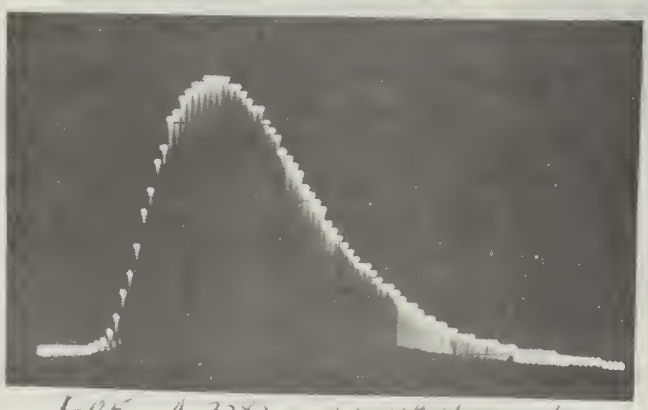

L=0.5 A = 32.82 1.6×10^4 c/cm Ch 0-100
0-0.5 mV

②

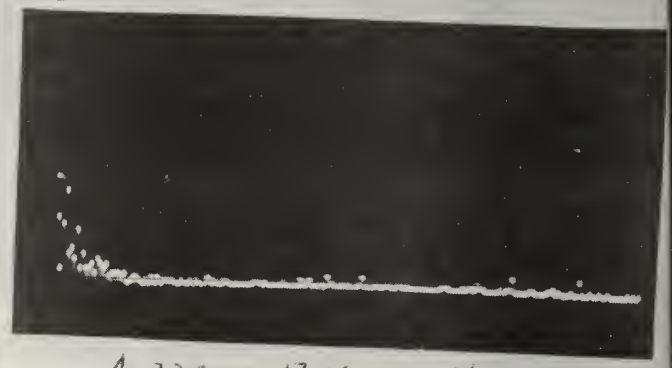

A = 32.82 17 c/cm Ch 200 - 400
1 mV - 2 mV

④

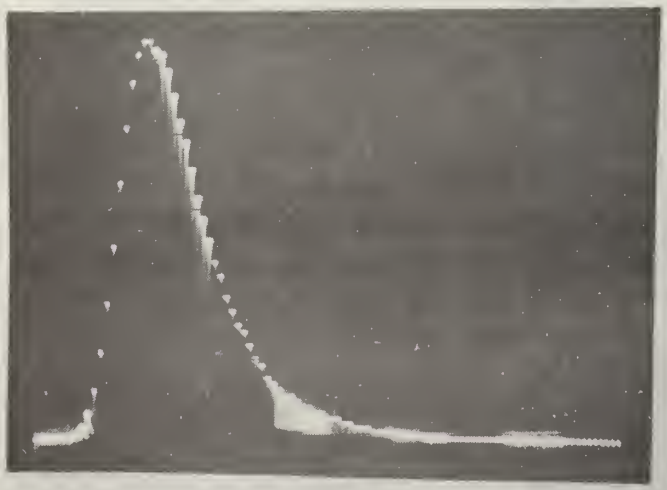

L=1.0 cm
A = 32.82
Ch 0-100 0-0.5 mV
1.6×10^4 c/cm

Position Dependence of Spectrum

19 August 1970

P = 8.1 psig
Countingtime 90 sec.

L = 2.0

A = 32.82 1.6×10⁴ c/cm ch 0-100
0-0.5 mV

(6)

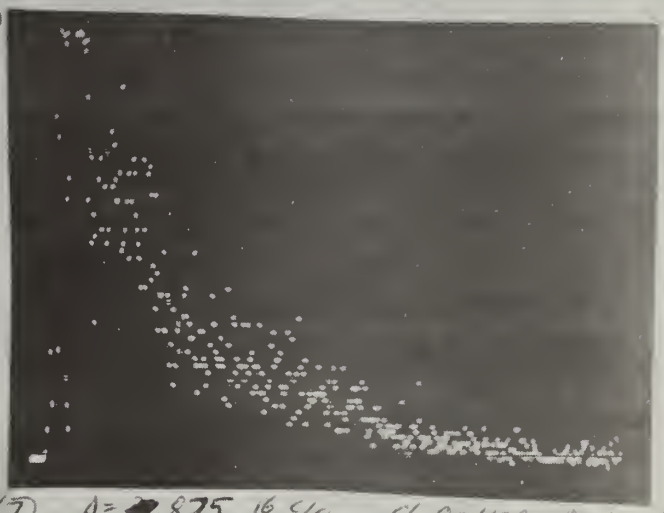

(7) A = 8.75 16 c/cm ch 0-400 0-10 mV

A = 8.75 100 c/cm ch 0-400 (0-10 mV)

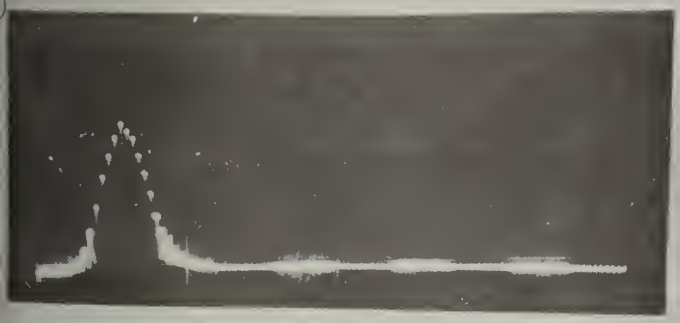

L = 3.0

A = 32.82
6700 c/cm
ch 0-100
0-0.5 mV

L = 4.0

A = 32.82
1600 c/cm
ch. 0-100 (0-0.5 mV)

24 August 1970

Positions on Axis
No gas flow
P = 8.0 psig

2)

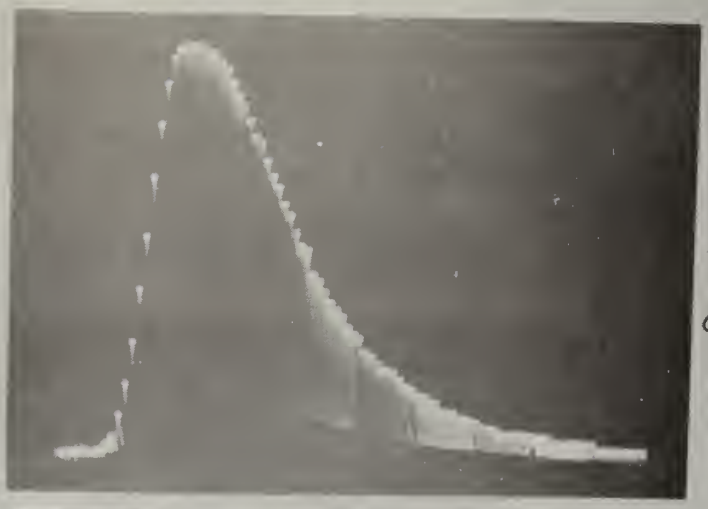

L = 0.3
A = 32.82
Ch 0-100
0-0.5 mV

110 c/cm sec

3)

L = 0.5
A = 32.82
Ch 0-100
0-0.5 mV

280 c/cm sec

4)

L = 1.0
A = 32.82
Ch 0-100
0-0.5 mV

280 c/cm sec

5)

L = 1.5
A = 32.82
Ch 0-100
0-0.5 mV

280 c/cm sec

6)

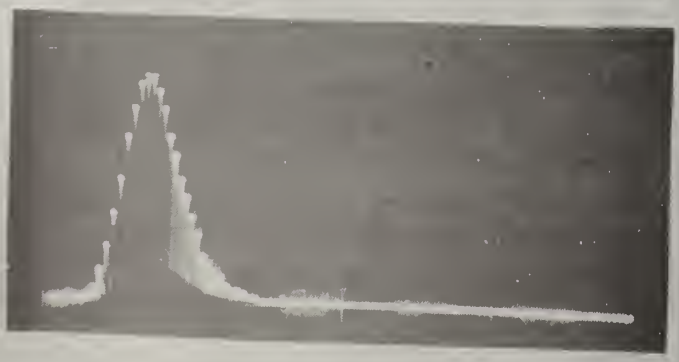

L = 2.0
A = 32.82
Ch 0-100
0-0.5 mV

110 c/cm sec

(62)

24 August 1970

Probe on Axis
No gas flow
P = 8.0 psig

7)

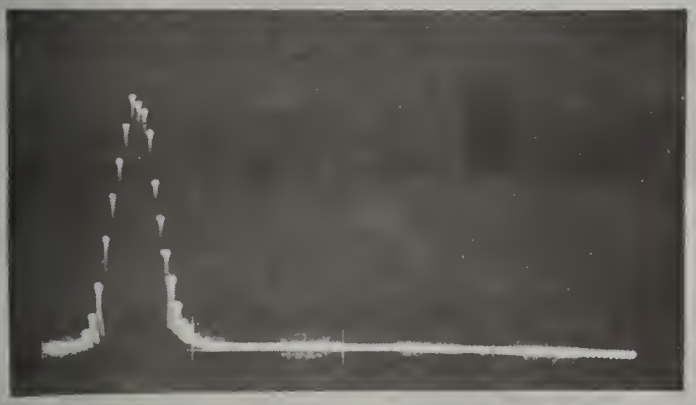

L = 3.0

A = 32.82

0 - 0.5 mV

28 c/cm sec

8)

L = 5.0

A = 32.82

0 - 0.5 mV

2.8 c/cm sec

L = 5.0

9)

A = 8.75 0 - 10 mV 1.1 c/cm sec

24 August 1970

Positions 1 cm off axi
Gas flow on
P = 8.0 psig
A = 32.82
0 - 0.5 mV

21)

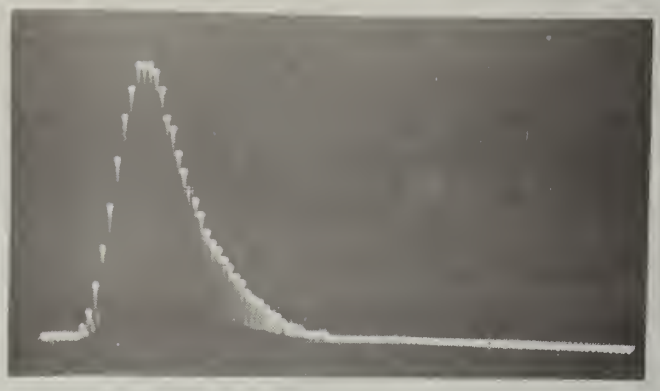

L = 1.0

110 c/cm sec

22)

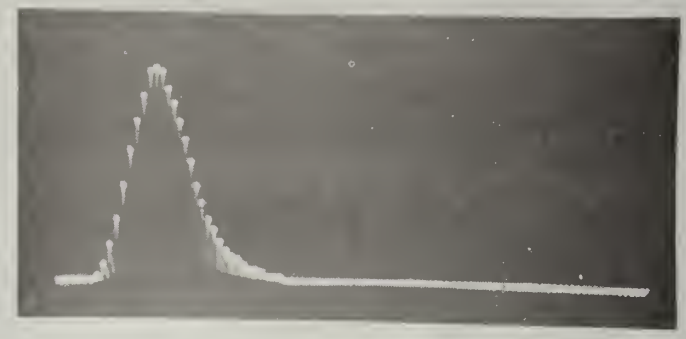

L = 2.0

110 c/cm sec

23)

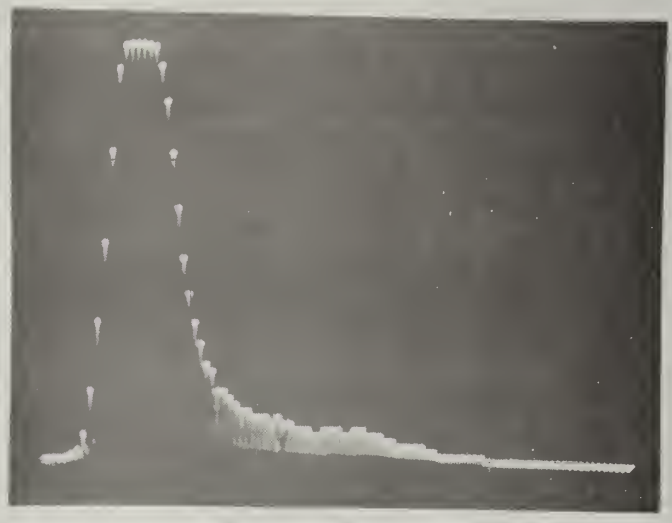

L = 3.0

28 c/cm sec

24)

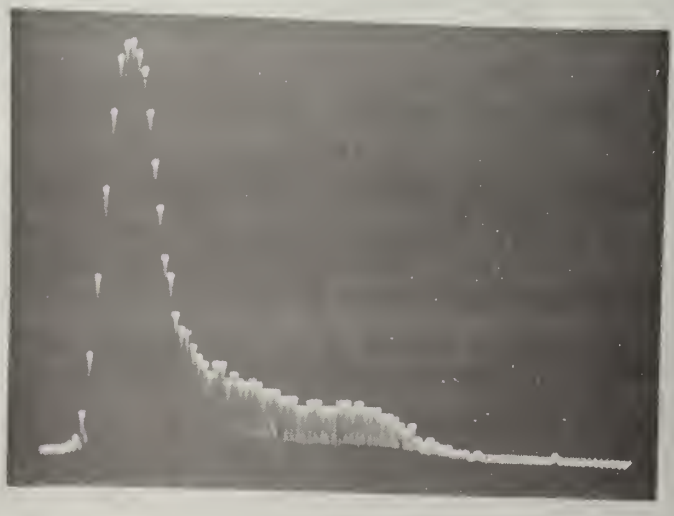

L = 5.0

11 c/cm sec

26 August 1970

Spectrum on axis with
gas flow
Circuit C
P = 8.0 psig
A = 32.82
Channels 1 - 100
0 - 0.5 mV

4)

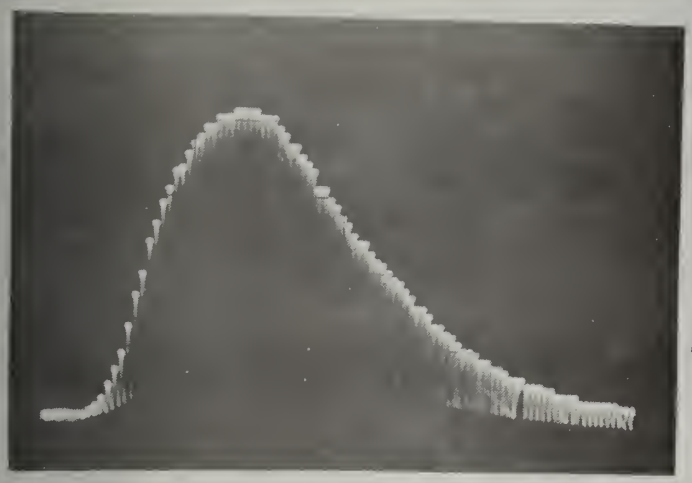

L = 0.2
180 c/cm sec
DT 56%

5)

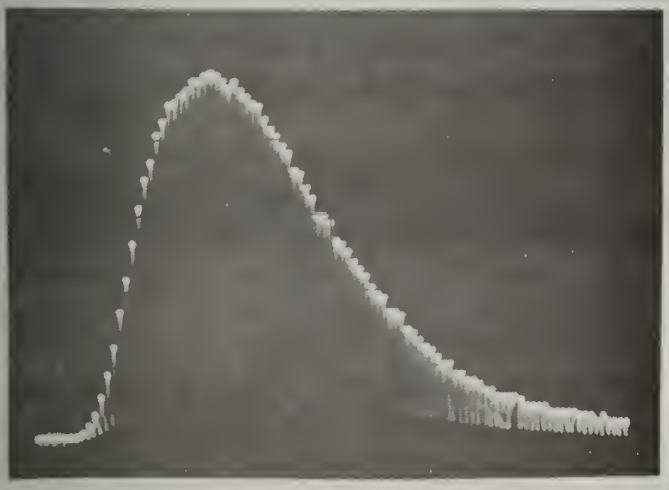

L = 0.5
110 c/cm sec
DT 50%

6)

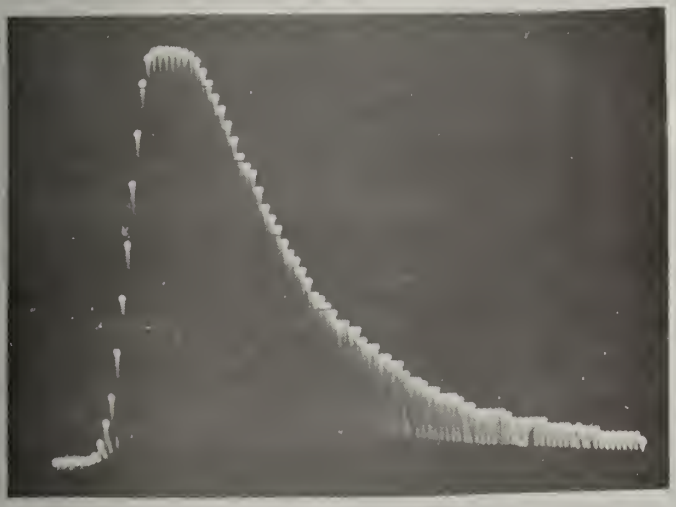

L = 0.75
110 c/cm sec
DT 45%

7)

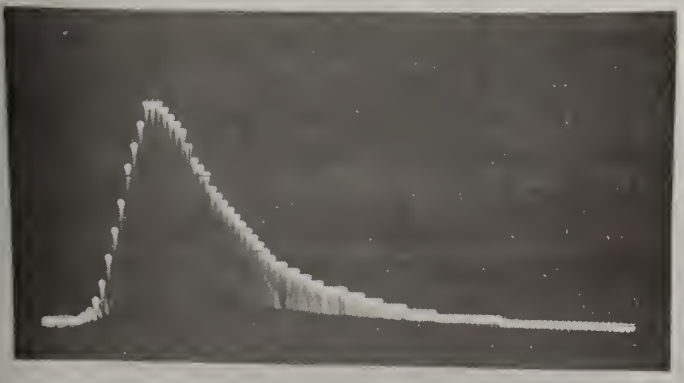

L = 1.0
280 c/cm sec
DT 35%

26 August 1970

Spectrum on Axis with gas flow
Circuit C
P = 8.0 psig
A = 32.82
Channels 1 - 100
0 - 0.5 mV

8)

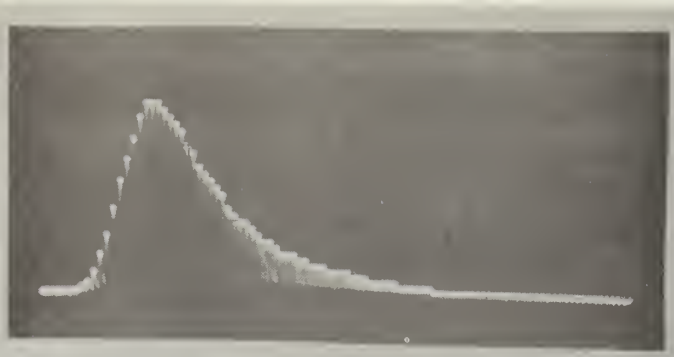

L = 1.25
280 c/cm sec
DT 30%

9)

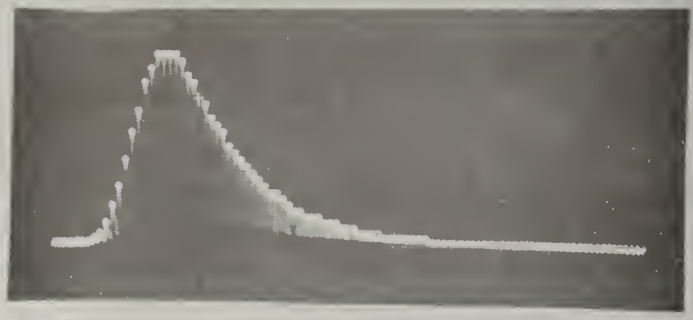

L = 1.5
280 c/cm sec
DT 25%

10)

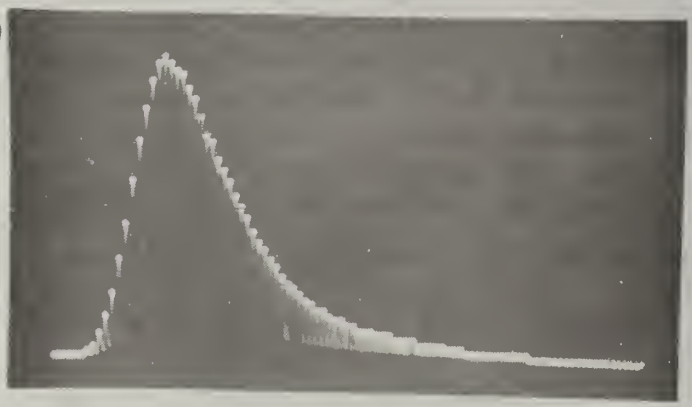

L = 2.0
110 c/cm sec
DT 25%

11) DT 20% 28 c/cm sec

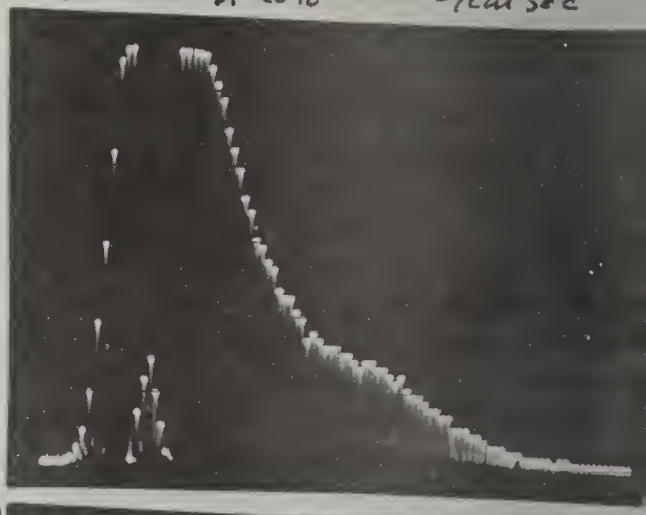

DT 20% 110 c/cm sec L = 2.5

17)

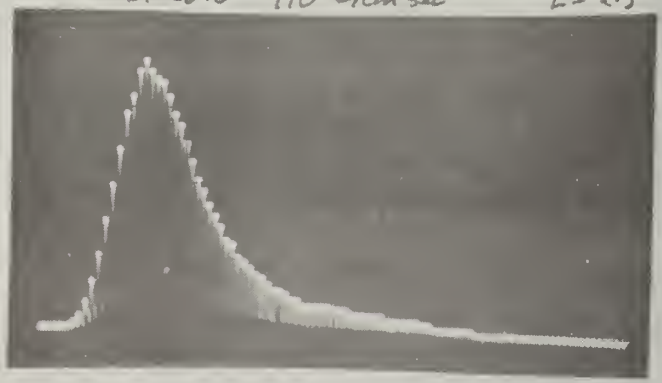

12)

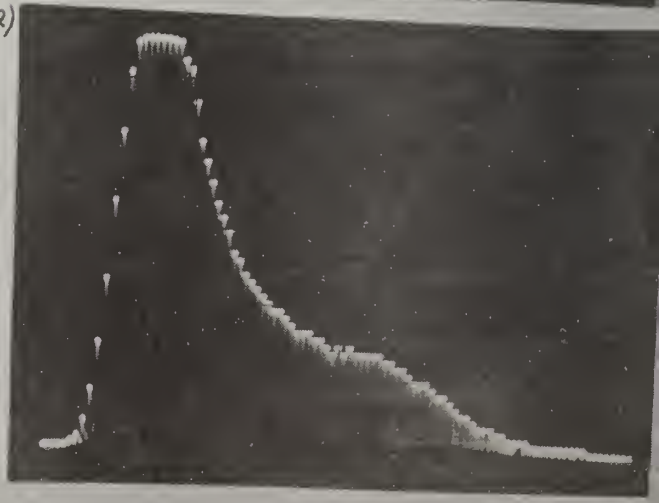

DT 15% 110 c/cm sec L = 3.0

18)

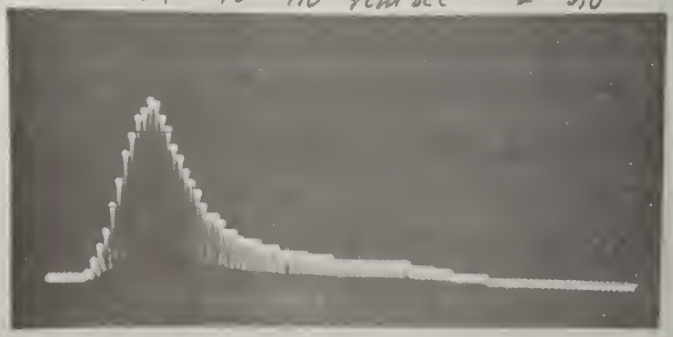

26 August 1970

Spectrum on Axis with
gas flow
Circuit C
P = 8.0 psig
A = 32.82
Channels 1 - 100
0 - 0.5 mV

13)

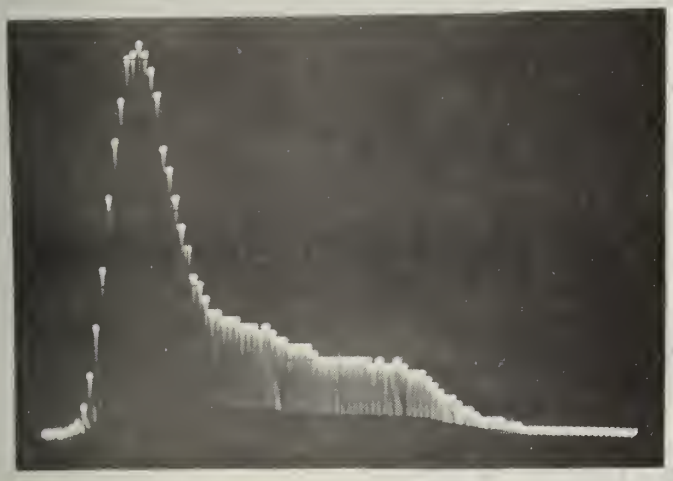

L = 4.0
28 c/cm sec
DT 10%

14)

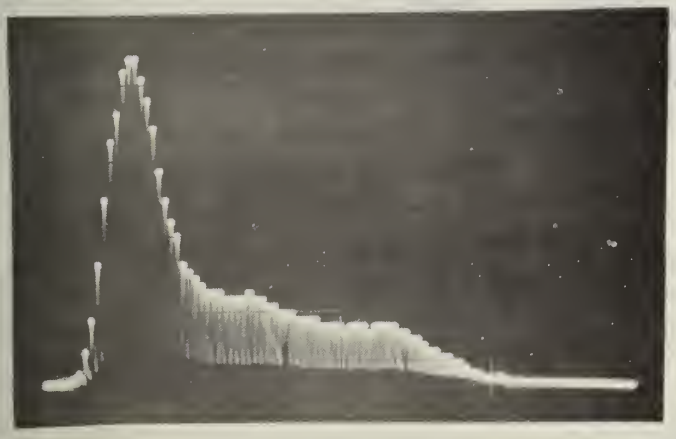

L = 5.0
28 c/cm sec
DT 5%

15)

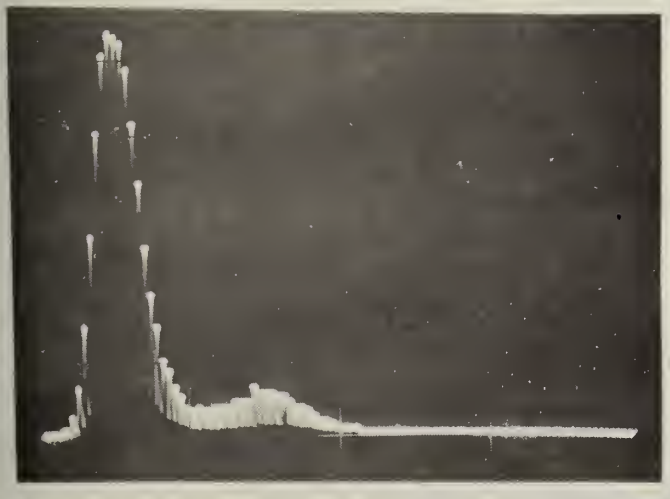

L = 7.0
11 c/cm sec
DT = 0

United States Naval Postgraduate School

THESIS

INVESTIGATION OF THE FEASIBILITY OF AN ELECTROGASDYNAMIC PROBE FOR MEASUREMENTS OF MEAN AND RMS VELOCITIES

by

Richard Alan Christianson

April 1970

ABSTRACT

This study involves the investigation of the feasibility of an electrogasdynamic (EGD) probe to measure mean and turbulent velocities. The free stream velocity was 185 ft/sec and measurements were made in the wake of a circular cylinder 2 cm in diameter. Readings made with a hot-wire anemometer at the same location and in the same spectral range were used as the standard of comparison.

The initial data indicated that investigations should be restricted to the region from 2 mm to 10 mm aft of the injector nozzle along the center line. Spectral data for both the hot-wire and the EGD probe measurements were obtained with a frequency analyzer and photographed from an X-Y display.

The use of an EGD probe for measurements of mean and rms velocities may be feasible since the results indicate a definite correlation. The utility of the probe, however, is yet to be demonstrated since both the spatial and spectral comparisons with the hot-wire results show some lack of correspondence. The EGD unit proved to be considerably more rugged than the hot-wire probe.

TABLE OF CONTENTS

LIST OF ILLUSTRATIONS

LIST OF SYMBOLS

Symbol	
A	ampere
cm	centimeter
dc	direct current
^{o}F	degree Fahrenheit
EGD	electrogasdynamics
F	farad
ft	feet
ft/s	foot per second
ft^3/min	cubic feet per minute
Hz	hertz
h	height
I_c	corona current
I_G	collector current
I'_G	collector current per frequency band
I_N	needle current
in	inch
k	kilo
L	collector-to-ring distance along centerline
lbf	pound force
mm	milimeter
ms	milisecond

P_S	stagnation pressure
P_1	static pressure
psig	pound per square inch gage
q_o	dynamic pressure
rms	root-mean-square
T	percentage of rms velocity to free stream velocity
T'	percentage of rms velocity to free stream velocity per frequency band
U_∞	free stream velocity
V	volt
V_c	corona voltage
v	temporal mean velocity over an arbitrary point
vs	versus
w	weight
μ	micro
ρ	density
Ω	ohms

I. INTRODUCTION

Electrogasdynamics (EGD) is the study of the interaction of a non-neutral gas with an electric field. The charged particles within the gas are moved against the resistance of an electric field much as in the Van de Graaff generator, thus performing electrical work. In this case, however, the belt of the Van de Graaff generator is replaced by a moving gas stream. As pointed out by W. E. Bennett [1], a somewhat greater charge can be carried in a volume than on a surface (the Van de Graaff belt) and the charge transfer rate can be much higher with a moving fluid flow. Consequently, the EGD generator promises higher currents and greater efficiency. These theoretical possibilities do exist and are the subject of much research [1, 2, 3].

This thesis deals with a comparison of EGD probe readings of collector current with mean and rms velocities measured by a hot-wire anemometer in the turbulent wake of a circular cylinder. The study was undertaken to determine if there is any correlation between the two. This probe is a separate application from the EGD power generator [2]. The probe consists of a simple, rugged stainless steel rod used to collect the charged particles. These particles are highly coupled to the gas flow by virtue of their low mobility. The use of the turbulent wake of a cylinder is not restrictive. Presumably any high or moderate intensity turbulent

field can be handled, and the cylinder is one important application. As stated by Biblarz [2] a highly turbulent flow may yield favorable results in increasing the breakdown potential of the carrier gas so that it may improve the performance of the EGD probe.

There are three prominent features of the EGD probe which may make it more attractive as an anemometer than the hot wire. First, the EGD probe is considerably more rugged; therefore, very highly turbulent fields can be probed. Second, it may have a higher frequency response since charged particles (depending on size) can follow turbulent eddies better than the hot-wire system. Third, the probe tip comprises a small area which may yield a better or more symmetrical spatial resolution than the hot wire. But there are also disadvantages, the main ones being a requirement for a high-voltage source (which carries with it the ever enduring high-voltage safety precautions) and the need for a source of charged particles for optimum ion size to cover the desired frequency range.

This investigation is a continuation of a more comprehensive, long-term project being carried on by Professor Oscar Biblarz, Department of Aeronautics, Naval Postgraduate School, Monterey, California.

II. REVIEW OF PREVIOUS WORK

Numerous experimental studies involving the two-dimensional wake behind a circular cylinder have been performed. Those done by Schlicting and Reichardt [4] have proved to be standards in this field, hence the turbulent wake of the cylinder is reasonably well defined.

In the study of flow around bodies in air, it is useful for some purposes to deal with air as a perfect fluid owing to its low viscosity, since this leads to considerable mathematical simplification. However, perfect fluid theory does not apply to the experimentally observed boundary layer on the body, or to the flow separation and turbulent wake behind the body. Because of the complexity of turbulent fluctuations, a completely theoretical formulation of turbulent flow has not so far proved possible and investigations in this field are thus semi-empirical in nature. By the consideration of suitable time-averages of turbulent motion, however, a certain measure of correlation can be obtained between theoretical prediction and experimental observations.

Since the present investigation is concerned with the correlation between the EGD probe measurements and the standard data obtained with a hot-wire anemometer, the review will slant toward the EGD work and not expound on the more conventional aspects [5].

Hinze [6] states that P. Thomas was probably the first to apply an electric discharge for a technical purpose, namely, for designing a diaphragmless microphone for radio broadcasting. He further states that in 1934 F. C. Lindvall used the sensitivity of the glow-discharge potential to gas velocity for measuring turbulence. To measure turbulence, Lindvall used platinum electrodes of 1.5 mm diameter separated by a distance of about 0.1 to 0.2 mm. The total potential difference across the electrodes amounted to about 300 to 400 V.

Hinze mentions that there is a sensitive response to gas velocity. It is possible to obtain a potential difference of one volt for a difference in velocity of one meter per second. This is considerably more than is obtainable with the hot-wire anemometer, where the potential difference is of the order of 0.01 volt per meter per second. Lindvall considered this a very important advantage, because a less strong amplification is needed. Another important advantage is that effects corresponding to the thermal inertia of the hot-wire anemometer are very insignificant.

Other investigators of electrical-fluid interactions are F. D. Werner [7], K. J. Nygaard [8], and H. R. Velkoff [3] to name but a few. Werner investigated the possible use of the glow discharge as a means for measuring air flow characteristics, Nygaard looked at the anemometric characteristics of a wire-to-plane electrical discharge, and Velkoff carried on an extensive study

of electrostatic interactions with fluid flows. They concluded that the EGD system holds great promise as a velocity or mass flow measuring method.

The background for this present investigation is given in Ref. 2 and is demonstrated with early models by W. T. Ober [9] and D. W. Wallace [10].

Ober [9] describes a colloidal ion generator and states that an important consideration in the design of an effective EGD generator is the mobility of the charged particles which are to be forced out to the collector. Mobility is a measure of the velocity of a charged particle under the influence of an electric field. A high mobility indicates that it would be difficult to force the ions away from their migration path in the electric field (from the needle tip to the ring) and, therefore, a low mobility is desirable. The method used by Ober to produce these low mobility ions was by condensing saturated steam in a corona discharge by means of expansion through a nozzle.

III. TEST FACILITY

Air is supplied by a Carrier three-stage centrifugal compressor (Figure 1) with a 4000 ft^3/min maximum flow rate and a maximum pressure ratio of two. The test channel is preceded by a cooling bank and a main plenum, as shown in Figure 2. The cooling bank is used to keep the temperature of the air flow close to ambient and to hasten the temperature stabilization. The main plenum and the EGD flow channel plenum (Figure 3) serve to reduce the level of free stream turbulence in the test section.

A teflon cylinder two inches long with a two-centimeter diameter was placed in the test channel in a vertical position four inches prior to the outlet. This cylinder houses the aerosol injector [9]. The injector nozzle (Figure 4) was placed at the trailing edge of the cylinder. The EGD flow channel and injector (Figure 5) is described by Biblarz [2].

The EGD system wiring diagram is shown in Figure 6. A Sorensen High-Voltage dc Power Supply is used to provide corona power. The corona voltage is monitored with a Sensitive Research Electrostatic Voltmeter. Various Simpson microammeters are used to read the needle and corona current and a Keithley Pico-ammeter is used to measure the collector current. A 100 k Ω resistor is used to develop a voltage for an input to an oscilloscope. The input to a frequency analyzer is made through a 0.5 μF

capacitor, and the analyzer is grounded. It was found that shielding of the resistor is required along with absolute certainty of solid, smooth connections in all parts of the circuitry, especially a good ground circuit. As described by Wallace [10], three International Rectifier Corporation diodes are used to prevent any reverse current. For 10 μA of collector current the voltage drop across the diodes is about 21 V so that the frequency analyzer floats 21 V above ground, which means care must be taken to prevent damage to the equipment. Thus, a neon-bulb safety circuit was installed.

Preliminary work involved applying this resistor voltage drop to a Type 1A6 Differential Amplifier Plug-In Unit of a Type 551 Tektronix Dual-Beam Oscilloscope. Typical results of this are shown in Figure 7 where V_c was 2.2 kV, L was 8.1 cm and 1.02 cm to the right of the center line. I_G was 1.3 μA while I_N was 19 μA. The oscilloscope was set at 0.2 V/cm and 0.5 ms/cm. The figure shows the range of frequencies which are present in the EGD system.

A General Radio Company, Type 1921 Real-Time Analyzer was used as a frequency analyzer for both the hot-wire and EGD investigations. The 1921 analyzer consisted of a 1925 Multifilter and a 1926 Multichannel RMS Detector. The 1926 detector processes signals from the multifilter digitally. The outputs of the filters are sampled, the sample data converted to digital binary form,

and the rms level computed from this. Averaging is by true, linear integration, which is not only faster than running-average analog circuits (that may also miss transients) but it helps identify what events in time have contributed to the answer. The computed band levels are stored in a digital memory and are available at outputs simultaneously with analog data. Peterson and Gross [11] describe the specifications along with variations of use for this versatile piece of equipment. A Hewlett-Packard X-Y display was connected to the Real-Time Analyzer to get a rapid graphic output of the collector current. Figures 8 and 9 show some of this equipment. As stated, the analyzer indicates spectral rms values as measured by either the hot wire or the EGD probe.

Measurements of pressure, temperature, and humidity were made with conventional metering equipment.

The collector probe was a 0.125 in stainless steel rod with a smooth pointed tip. It is rugged and was easily constructed. It can be placed in any position of the flow and was mounted on an insulated traversal unit allowing vertical and horizontal movement for any axial position to within $\pm$ 0.5 millimeters.

A steam generator supplies steam to the cylinder through a heated line to prevent condensation of the steam while it is in the line. The cylinder acts as a reservoir and feeds steam to the nozzle.

IV. EXPERIMENTAL PROCEDURE

The first portion of this investigation consisted of determining the standard airflow properties of the wake behind a circular cylinder. All the tests were made at a Mach number below 0.3 and at atmospheric conditions. A constant temperature hot-wire anemometer, Security Associates, Model 200, with a 0.00015 in diameter tungsten wire in the probe was used to determine the velocity and turbulence in and around the wake as shown in Figure 10. When using the hot-wire anemometer, the symmetry of the cylinder was exploited and probes were made only from the center line to the right side outward. Various spot checks were made in other portions of the wake to validate this use of symmetry. Both overall rms-turbulence and individual band turbulence was obtained by a Balantine True RMS Voltmeter and the frequency analyzer respectively. To reduce breakage of the hot wires, the air flow was no higher than 185 ft/s as computed in Appendix A. Moreover, all the data were obtained at this speed. Both mean and turbulent velocities within the wake were read as a percentage of free stream velocity.

The second portion of this investigation consisted of taking the EGD system readings. Again the air flow was at 185 ft/s and the same locations were used for probing here as with the hot-wire anemometer. Charged particles were injected into an air stream

first by the use of a molecular ion device and later a corona-aerosol device. These particles were then collected by a small, rugged metallic probe at the desired position. The EGD interaction using molecular ions was too weak. The use of an aerosol flow consisting of charged water droplets in air increased the collector current. Steam at a pressure of 14 psig and 250°F was used through the injector; ambient temperature was 72°F. Preliminary work showed very little difference in the hot-wire anemometer readings with and without steam as long as the steam remained dry. But it was decided not to use the steam with the hot wire because of the uncertainty of interpreting results in the two-phase system. Instead, air at the same reservoir pressure as the steam was used (this matches the momenta of the two).

Prior to applying the high voltage, a visual check of the circuitry was performed along with a continuity check on the needle and ring of the injector. This corona unit was cleansed with freon for each run to reduce surface breakdown. Following each run, after high voltage shut down, all main connections were grounded with a grounding rod to insure against electrical shock.

The EGD system was connected as shown in Figure 6 and the readings were taken for comparison with the hot-wire anemometer data. Biblarz [2] discusses the principles of operation of this EGD system in some detail and notes that the collector probe retrieves the charges and causes a buildup of a potential between the collector

and ground, with the resulting current flow through the collector circuit representing the work done by the air flow, or the output of the EGD system. The EGD probe is basically a short-circuited EGD generator.

The frequency analyzer was set for four-second integrations from band 14 to band 43, 25 Hz to 20 kHz in one-third octave bands. Eight-second integrations were also used to compare the results of the same conditions to the four-second integrations. No discernible difference was detected. The analyzer results were portrayed on the X-Y Display and photographed.

V. DISCUSSION OF RESULTS

EGD probe readings of collector current and mean and rms velocities measured by a hot-wire anemometer were made to determine the spatial correlation of the three, and then spectral measurements were taken in regions of good correlation. The results of this investigation will be discussed from an analysis of Figures 10 through 28.

Figures 11 through 15 show the actual data of mean velocity, turbulence and collector current measured at the probe positions shown in Figure 10. The mean velocity is expressed as a ratio of mean velocity to free stream velocity (v/U_∞) while the turbulence (T) is expressed as a percentage of the rms velocity to free stream velocity. Figures 16 and 17 depict scattergrams of these data and were used to determine where the EGD collector current compares favorably with the hot-wire measurements. These results indicate an acceptable correlation of collector current and turbulence over a portion of the region investigated. This region is within a plane oriented with the flow, one cm on either side of the center line running from the nozzle to the exit of the test section. The mean velocity did not compare favorably, and near the center line there was somewhat of an inverse correlation. Further investigations were restricted to comparisons of collector current and turbulence along the center line. The highest collector currents occurred at

about two centimeters aft of the cylinder on the center line; this can probably be attributed to the characteristics of the charged aerosol. The scattergrams (Figures 16 and 17) show a somewhat regular pattern between the EGD collector current and both mean and overall rms velocities.

Figures 18 through 25 show the spectral data from both the hot-wire anemometer and the EGD probe at different positions behind the cylinder on the center line. These data were obtained from the frequency analyzer and photographed on the X-Y Display. The horizontal scale is a frequency scale running from 25 Hz to 20, 000 Hz; the analyzer outputs in 30 discrete bands. The vertical scale is a voltage proportional to the rms value. Figure 18 shows the reference value and an internal calibration. The residual free-stream turbulence can be seen in the upper picture. Figure 19 shows the EGD probe reference without air flow. Note the absence of high frequencies in Figures 18 and 19. Figures 20 through 25 show measurements at three different locations behind the cylinder (4 mm, 5 mm and 7 mm). Zero is always the lower left-hand blip. First the hot-wire turbulence measurements were made with just the main air to establish a local reference, and then with both main and nozzle air. The nozzle air permits the simulation of the EGD probe flow field but without the steam. Subsequently, the EGD probe current readings were taken at the same location so that spectral comparisons could be made. The next task is to better

define the comparable features of these curves.

Figure 26 is a normalized curve of the hot-wire (nozzle and main air) and EGD results at L = 5 mm. This curve is typical of the data obtained. The bands corresponding to the vertical grid lines are identified there. A peak at twice the Strouhal frequency [4] of the cylinder can be seen here, as well as in all of the spectral data obtained. (The Strouhal number for this cylinder is 0.21.) Also in this figure, the hot-wire readings lie below the EGD probe at the low frequencies, but at the high frequencies they lie above. Figure 27 is a scattergram of the collector current per frequency band (I'_G) and the turbulence per frequency band (T') for the same data as Figure 26. This graph shows the result that the collector current is a function of turbulence at the higher frequencies (1,250 - 10,000 Hz).

Figure 28 indicates the ratio of I'_G/T' vs frequency for all three spacings reported. Because of the small scatter of the data, the figure displays a definite functional dependence between I'_G/T' and frequency. A relative minimum lies close to twice the Strouhal frequency, but otherwise a smooth curve can be drawn through the points.

VI. CONCLUSIONS AND RECOMMENDATIONS

The use of an EGD probe for measurements of mean and rms velocities is feasible since the results of Figures 16, 17, 27 and 28 indicate a definite correlation. The utility of the probe, however, is yet to be demonstrated since both the spatial and spectral comparisons with the hot-wire results show some lack of correspondence.

As seen from Figures 18, 19 and 26 the high frequencies are contributed by a range of vortices shedding off the cylinder, centered about the Strouhal frequency. The reason for seeing twice the Strouhal value is because readings were taken along the center line of the cylinder. This octave above the Strouhal frequency shows as a definite peak in all the data, although the EGD probe readings indicate a slightly higher value.

The conjuncture that the EGD probe may have a higher frequency response than the hot-wire anemometer is not validated by Figure 28. This may be due to the large droplet size issuing from the injector (this situation was brought about by the necessity to run the steam injector at its highest wetness in order to maximize the collector current). This fact may also explain the low frequency discrepancy, since relatively large droplets would enhance the low frequency spectrum. It is recommended, therefore, that more tests be run with dryer steam to check out the frequency dependence of the charged aerosol. This hopefully would raise the high frequency

end in Figure 28. In this figure, a horizontal band is desired but not necessary since a definite correlation can be expressed algebraically and used to interpret the EGD probe data.

The EGD probe was indeed more rugged in that it did not break, whereas at least 20 hot wires did, even though tests were at the low velocity of 185 ft/s. The particular hot-wire anemometer used gave the greatest problem by drifting, so care must be exercised here. Since both the same traversal unit and probe mount were used for the EGD and hot wire systems, it is believed that the frequencies introduced from probe vibrations are the same.

The spatial resolution in these experiments was undetermined, and it is hoped that this item can be looked into in future work.

A possible way to improve results may be to increase the amount of collector current while retaining the ability to change the wetness of the vapor. This might be accomplished through a more carefully constructed injector unit in which the spacing between needle and ring can be varied. Obviously, more work is needed to optimize the injected particle sizes for a given frequency range.

A practical EGD probe would require the development of an injector which is small and can be traversed with the collector, perhaps with a fixed spring. This would permit the probing of more arbitrary flow fields.

APPENDIX A

Determination of Free Stream Velocity

A pitot-static tube located in the front of the test channel was utilized to obtain the readings for this determination and applied as described by Pao [12].

$$q_o = P_S - P_1 = 1/2 \rho v^2 = wh$$

$$q_o = \frac{(62.4 \text{ lbf/ft}^3) \times (h(\text{cm})\text{cm})}{(2.54 \text{ cm/in}) \times (12 \text{ in/ft})} = 2.045\ h(\text{cm})\ \text{lbf/ft}^2$$

$$U_\infty = (2q_o/\rho)^{1/2} = \frac{(2 \times 2.045\ h(\text{cm})\text{lbf/ft}^2 \times 1 \text{ slug-ft})^{1/2}}{(0.002378 \text{ slug/ft}^3 \times \text{lbf-s}^2)^{1/2}}$$

$$U_\infty = 41.5(h(\text{cm}))^{1/2} \text{ ft/s}$$

$$U_\infty (h = 20 \text{ cm}) = 185 \text{ ft/s}$$

APPENDIX B

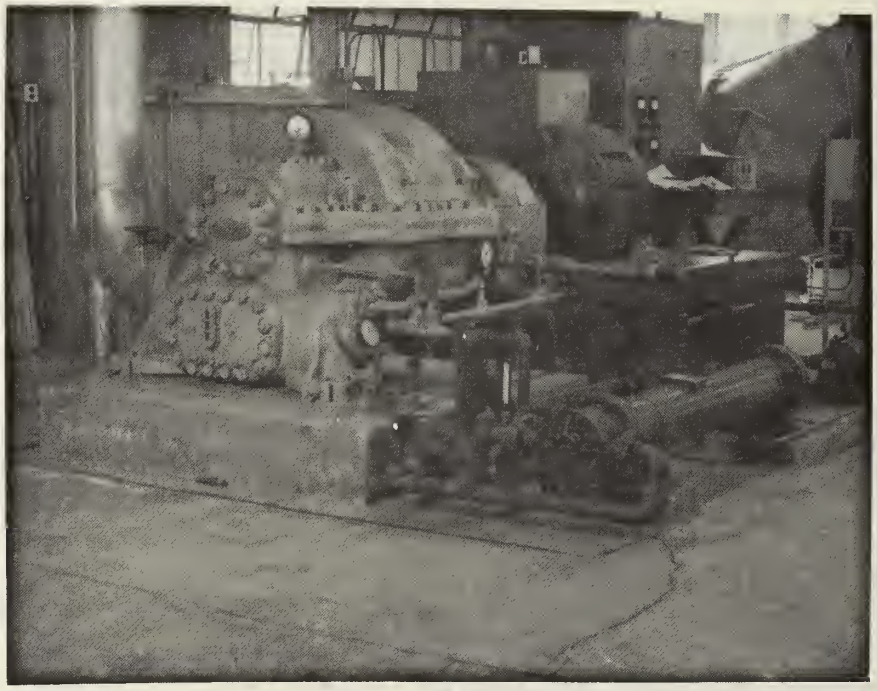

FIGURE I. AIR SUPPLY COMPRESSOR

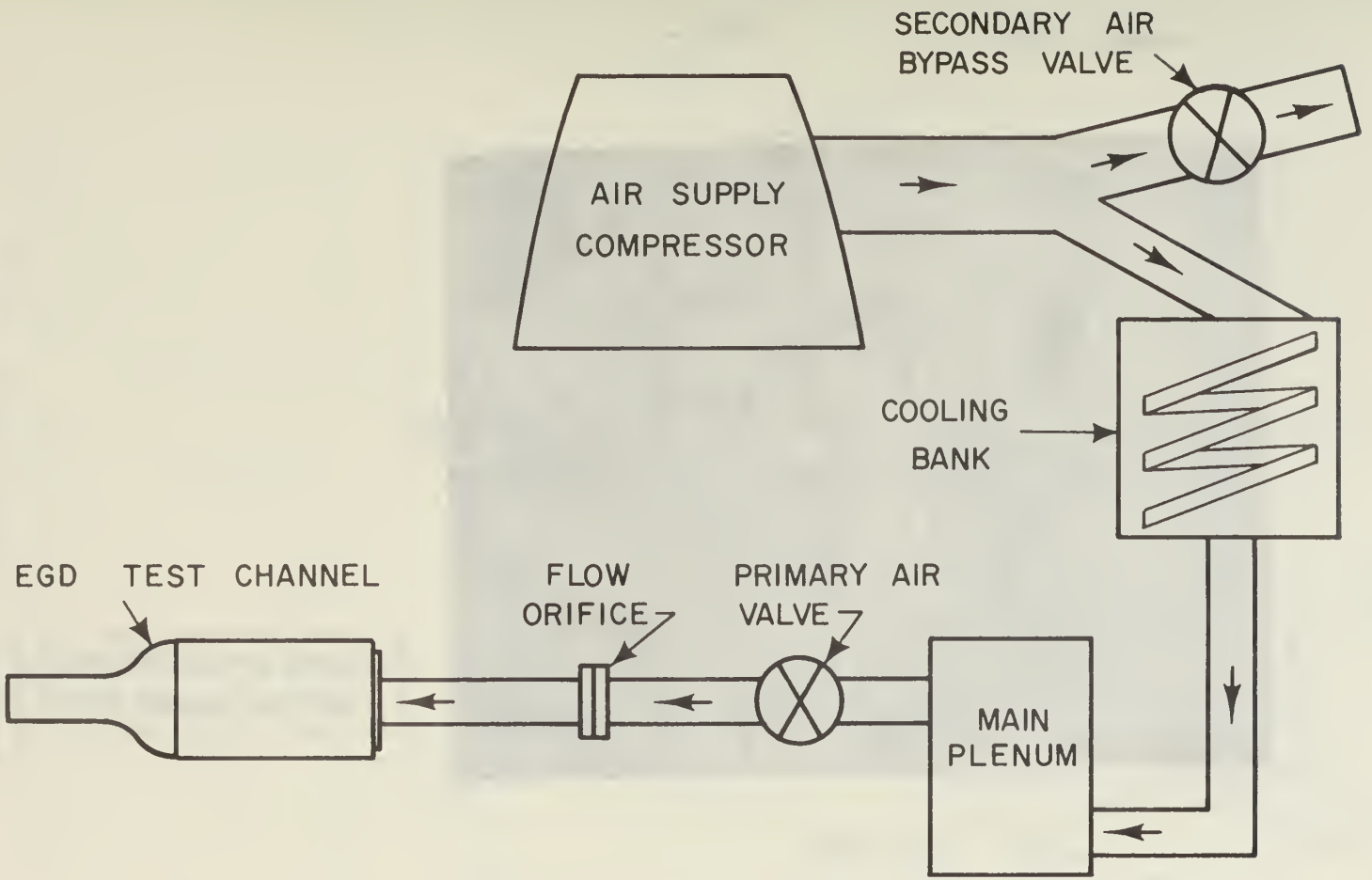

FIGURE 2. EGD SYSTEM FLOW CHART

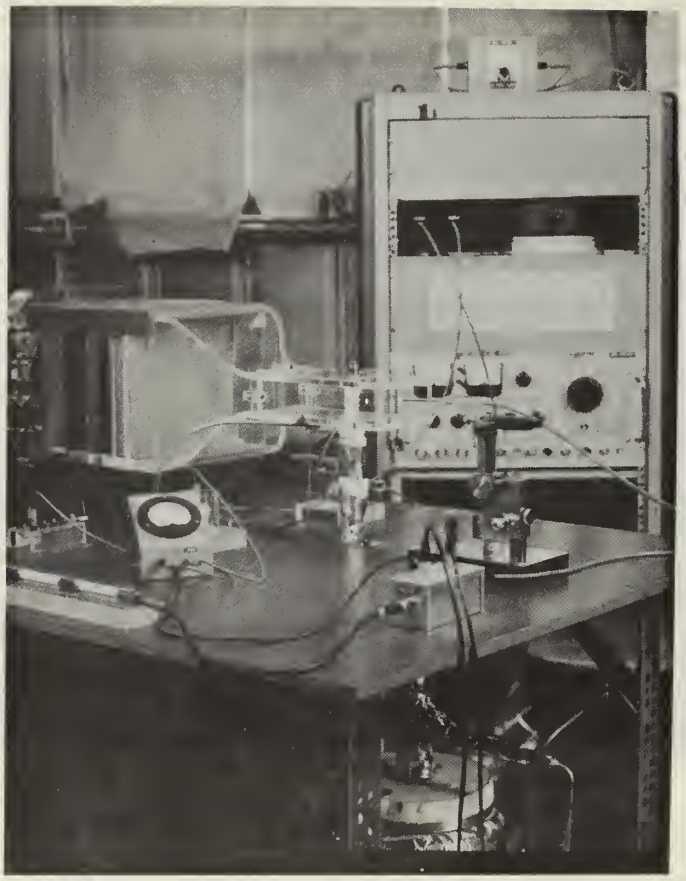

FIGURE 3. EGD TEST SETUP

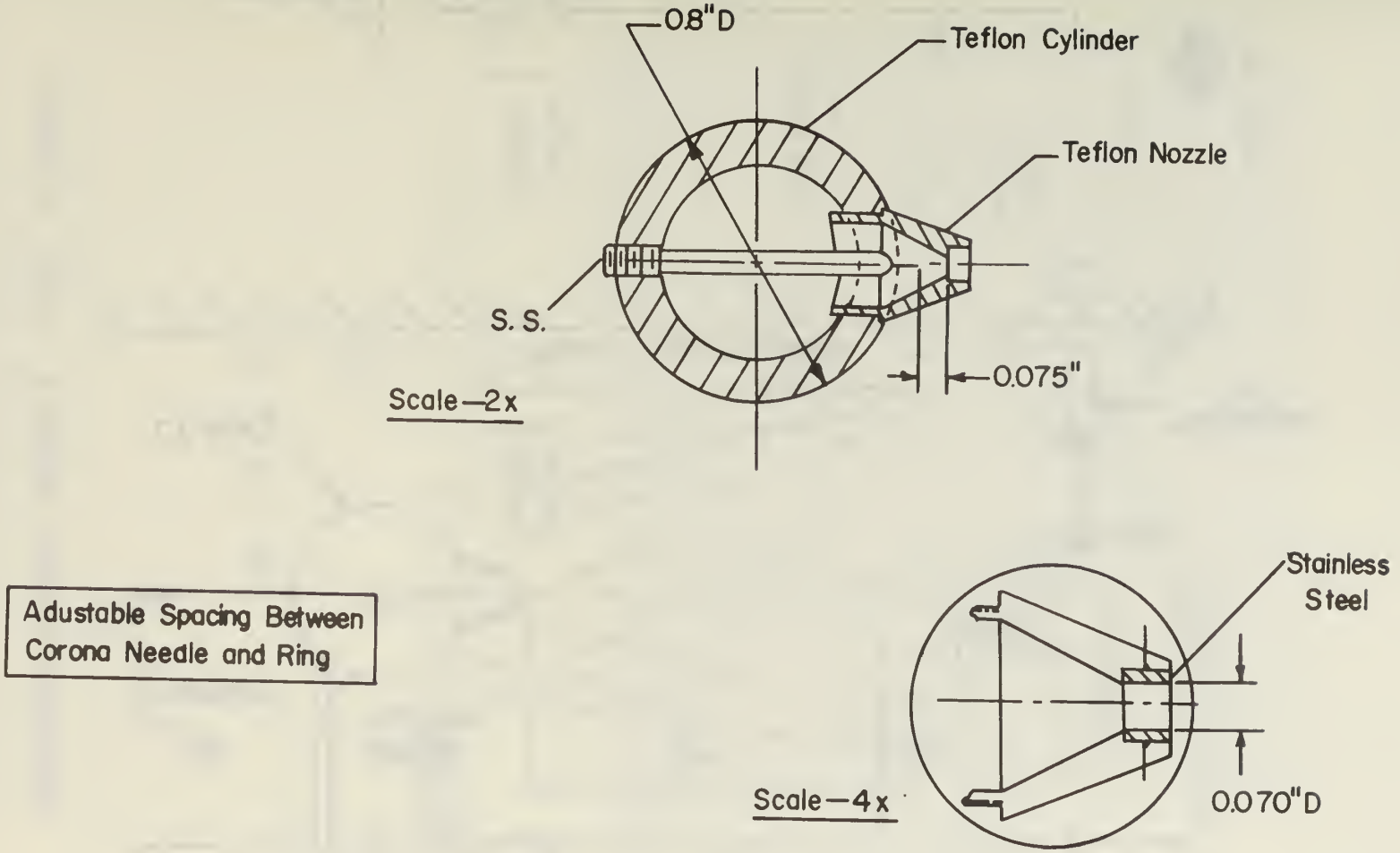

FIGURE 4. AEROSOL INJECTOR

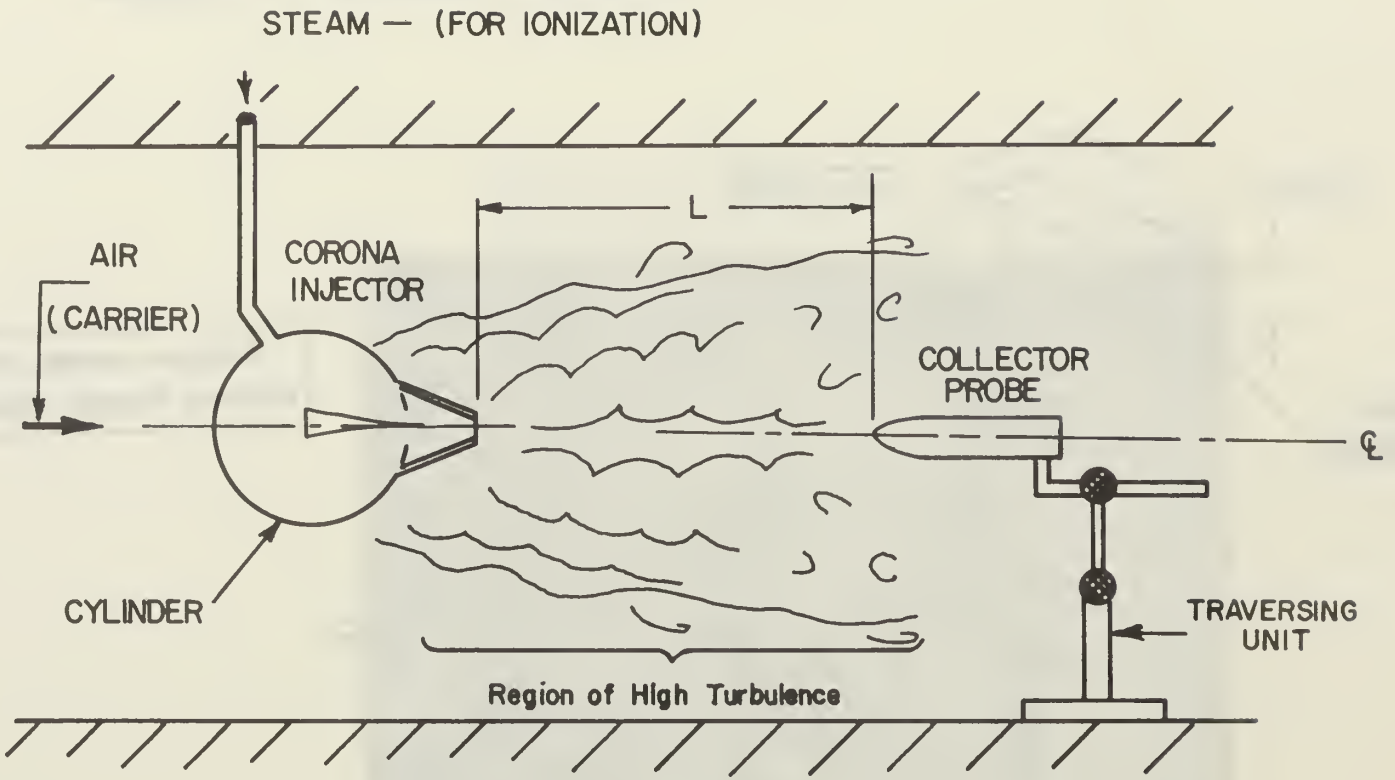

FIGURE 5. EGD FLOW DIAGRAM

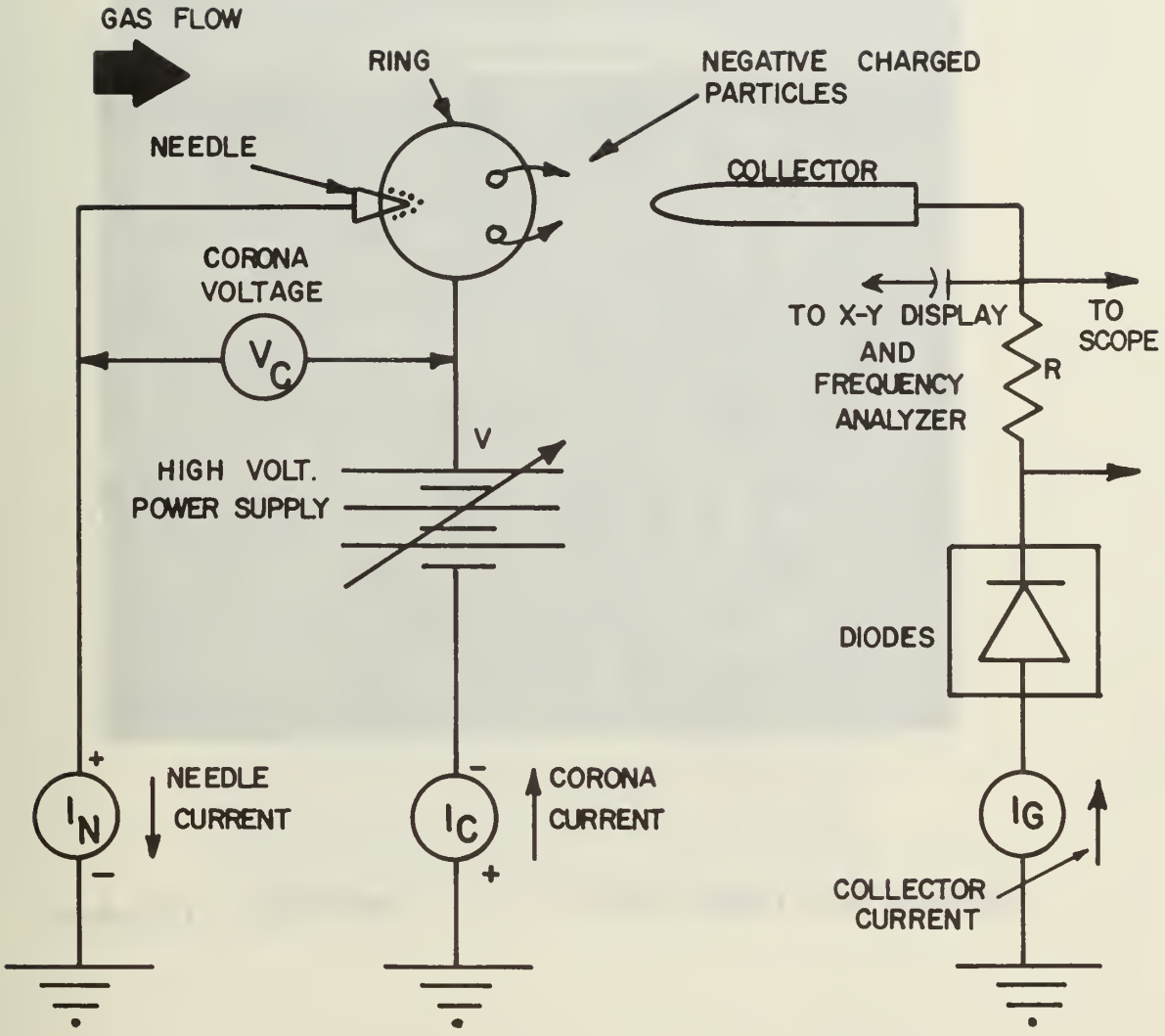

$$I_N = I_C + I_G$$

FIGURE 6. EGD SYSTEM WIRING DIAGRAM

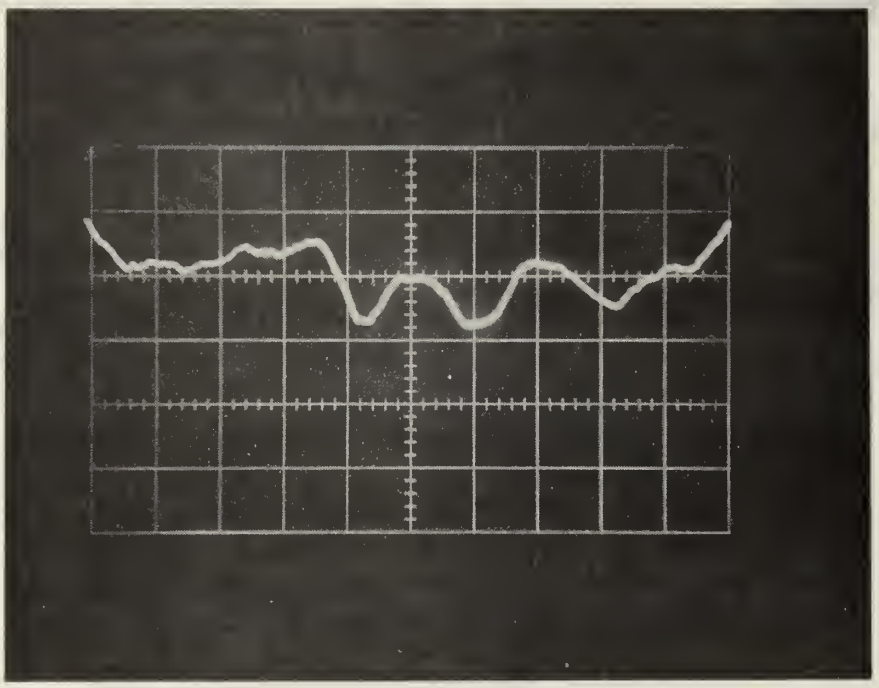

HORIZONTAL : 0.5 ms / cm VERTICAL : 0.2 V /cm

FIGURE 7. A.C. COLLECTOR CURRENT OSCILOSCOPE PATTERN.

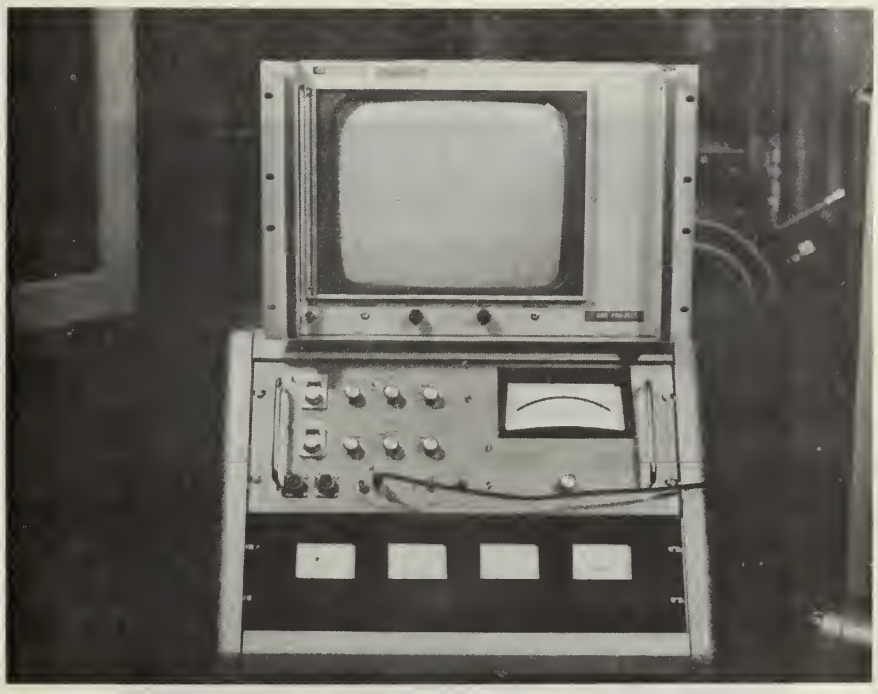

FIGURE 8. X-Y DISPLAY AND HOT-WIRE ANEMOMETER

FIGURE 9. ELECTROSTATIC VOLTMETER (TOP)
PICOAMMETER (CENTER)
FREQUENCY ANALYZER (BOTTOM)

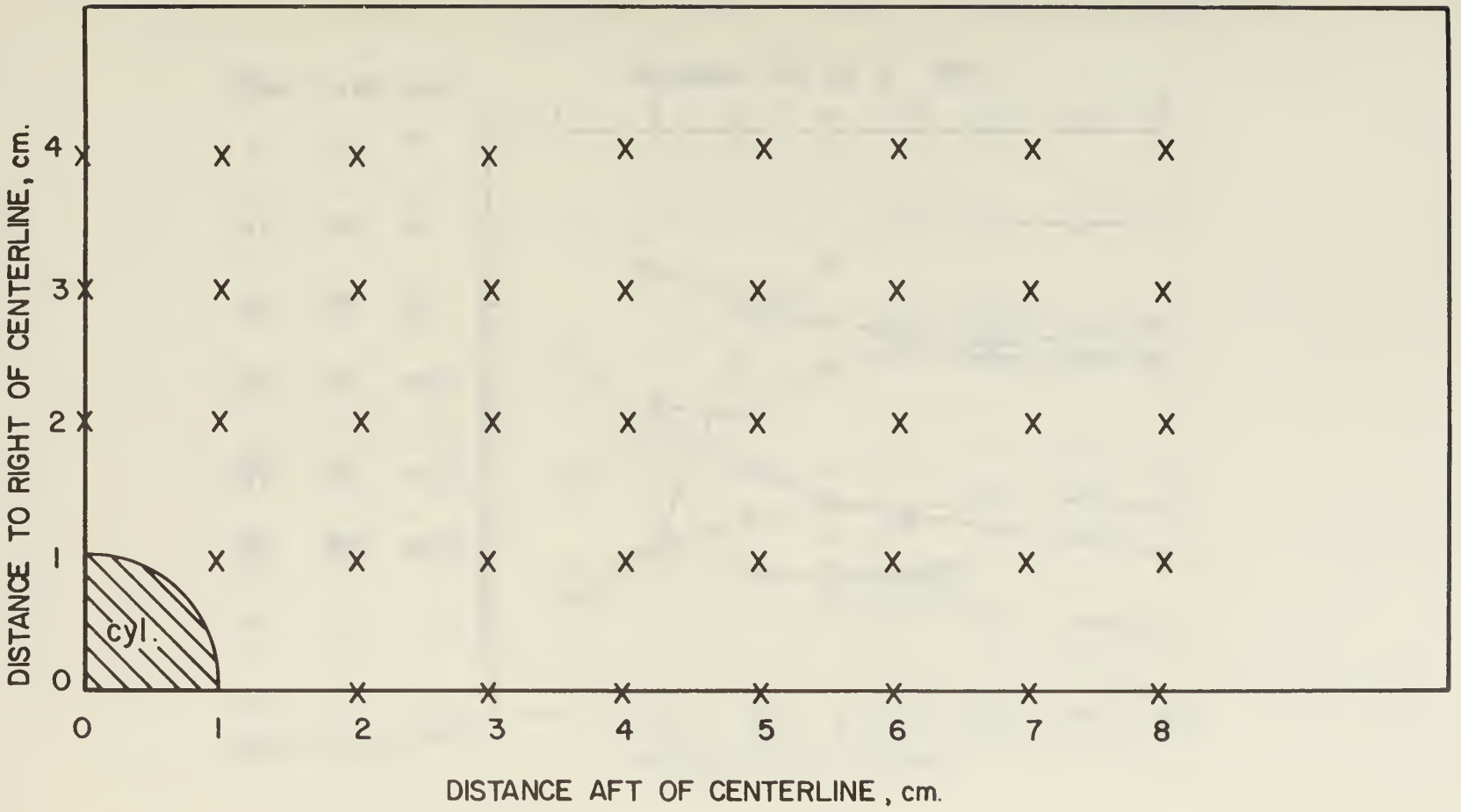

FIGURE 10. DATA POINT PROBE POSITIONS

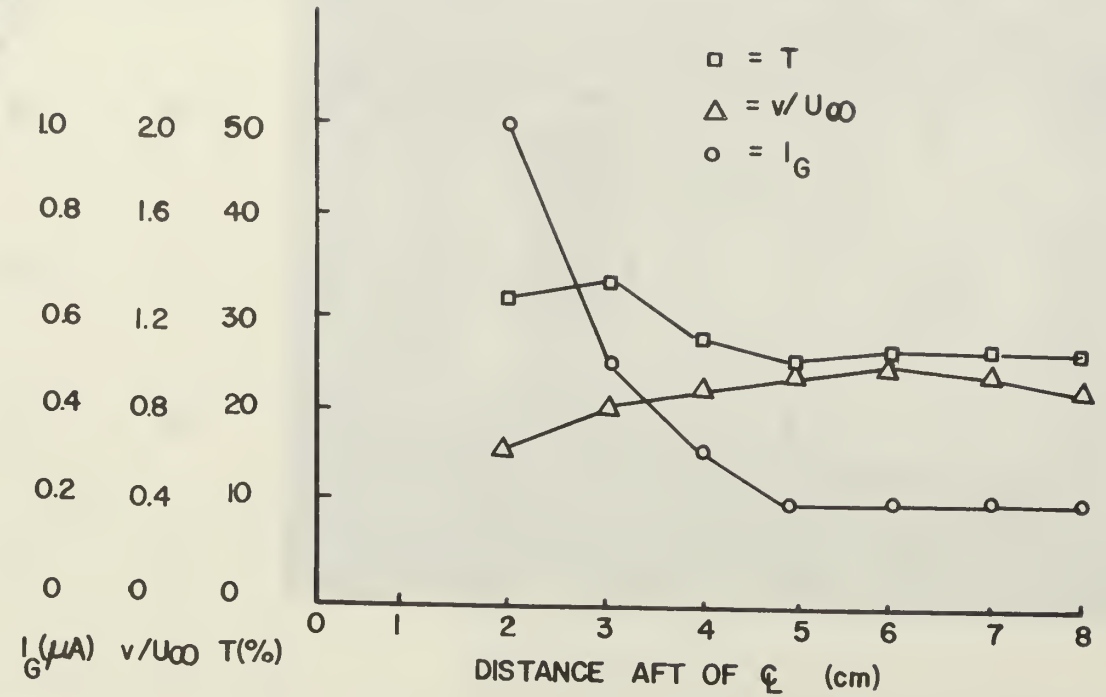

FIGURE 11. VELOCITY, TURBULENCE AND COLLECTOR CURRENT (ON CENTERLINE)

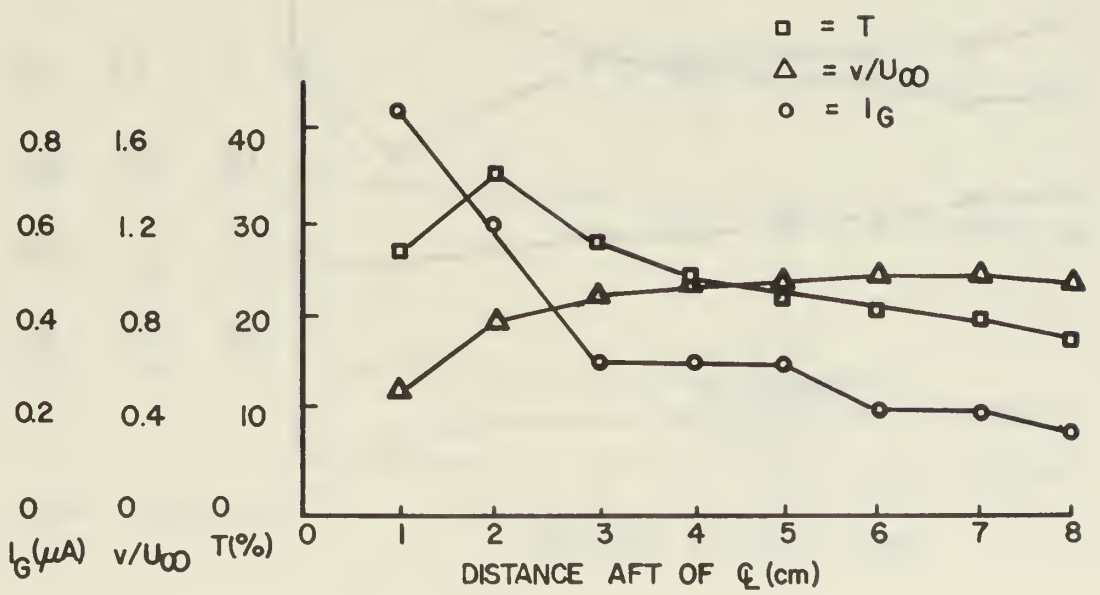

FIGURE 12. VELOCITY, TURBULENCE AND COLLECTOR CURRENT (ONE CM. TO RIGHT OF CENTER LINE)

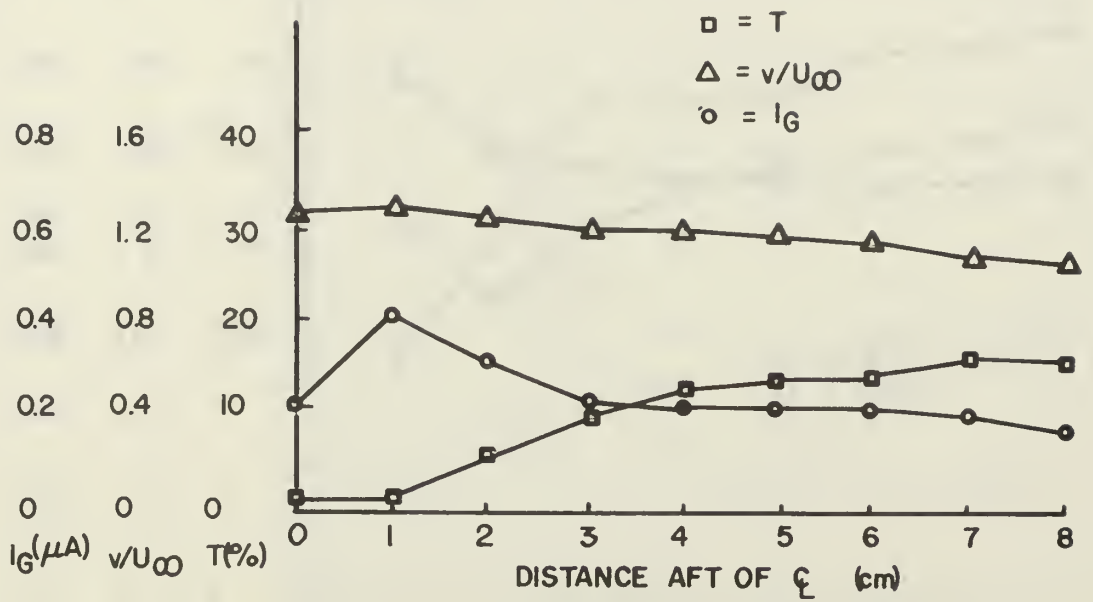

FIGURE 13. VELOCITY, TURBULENCE AND COLLECTOR CURRENT (TWO CM. TO RIGHT OF CENTERLINE)

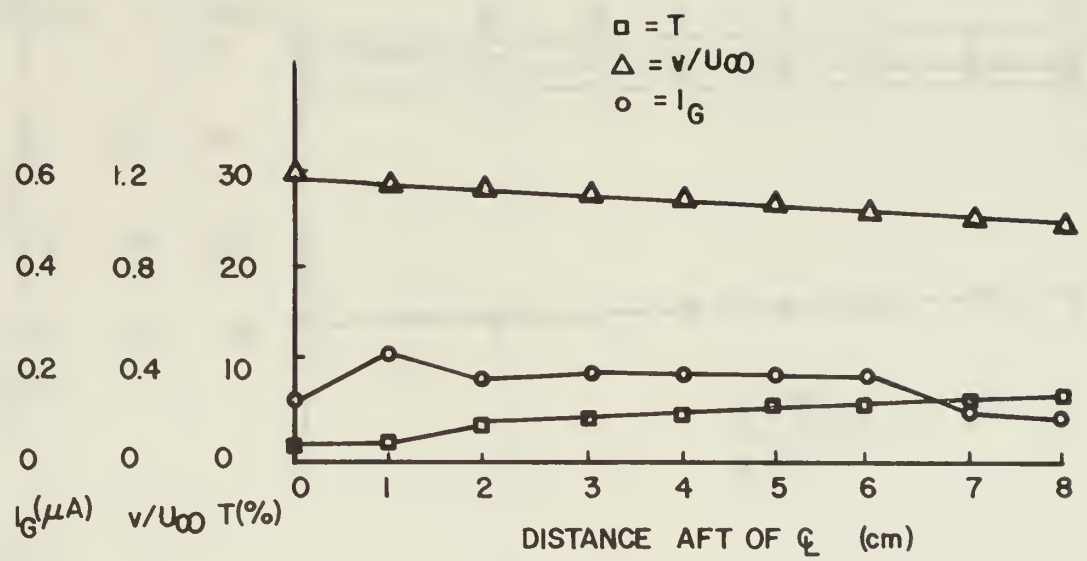

FIGURE 14. VELOCITY, TURBULENCE AND COLLECTOR CURRENT (THREE CM. TO RIGHT OF CENTERLINE)

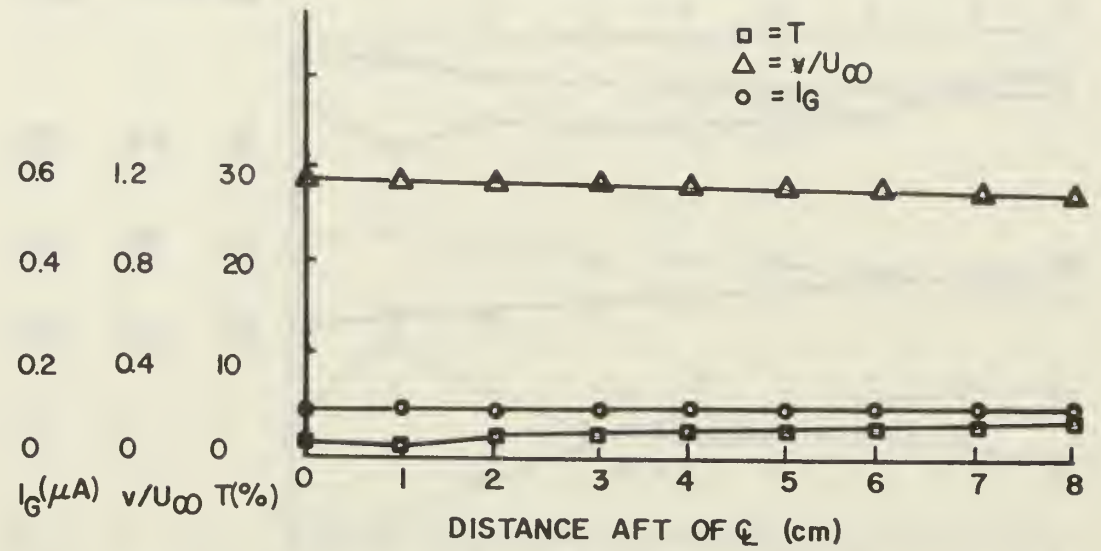

FIGURE 15. VELOCITY, TURBULENCE AND COLLECTOR CURRENT (FOUR CM. TO RIGHT OF CENTERLINE)

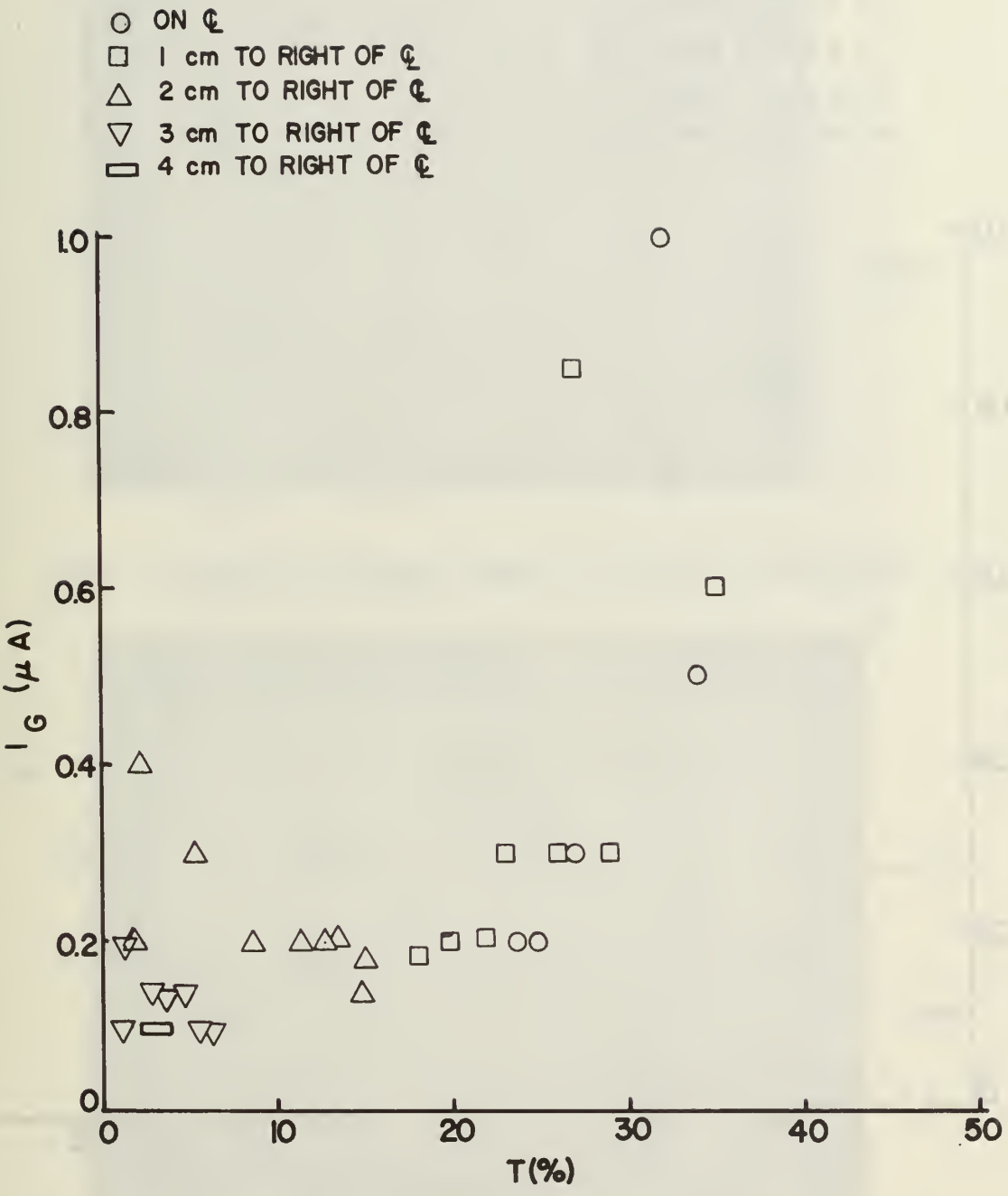

FIGURE 16. SCATTERGRAM OF COLLECTOR CURRENT AND TURBULENCE

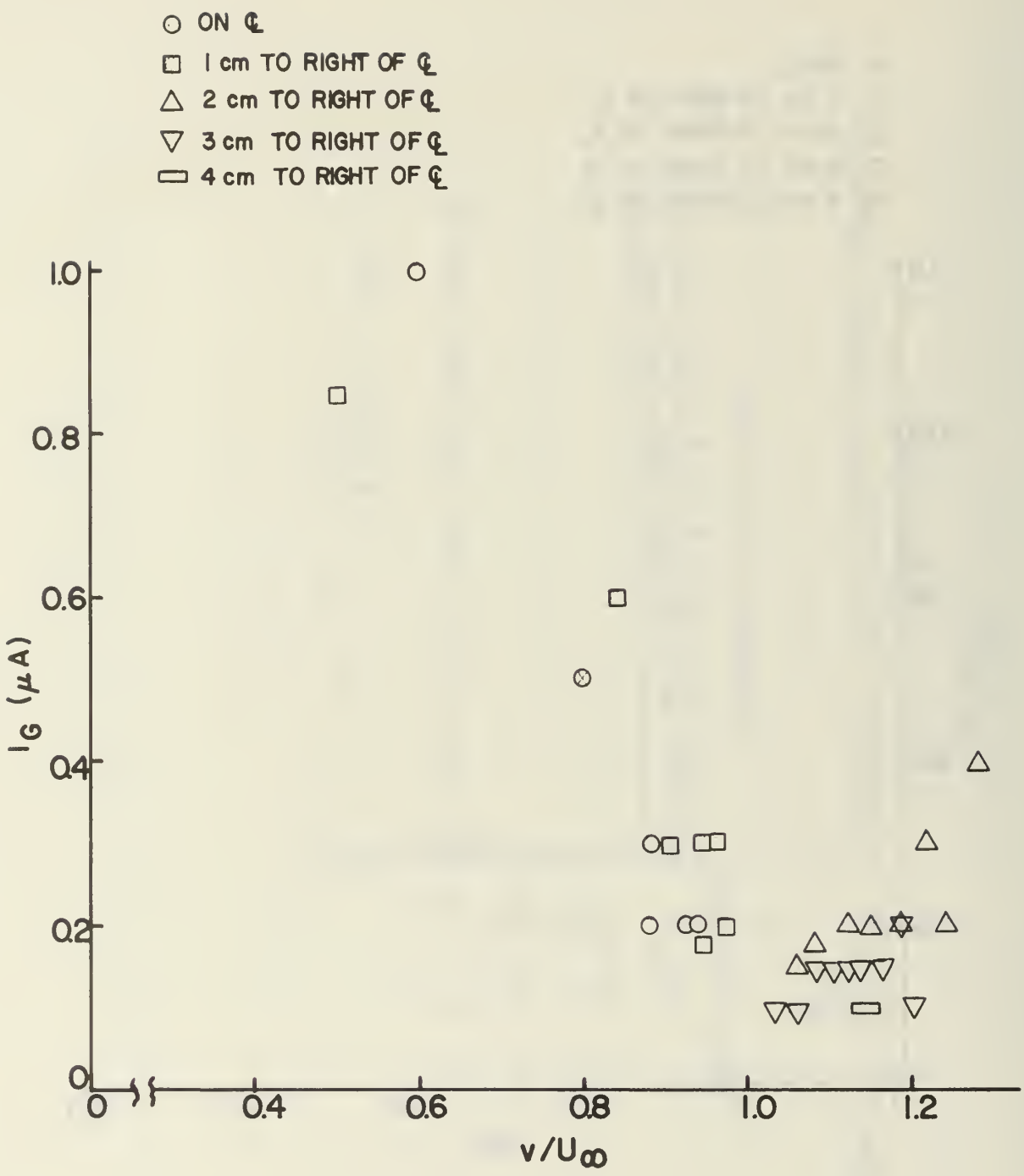

FIGURE 17. SCATTERGRAM OF COLLECTOR CURRENT AND MEAN VELOCITY

FREE STREAM REFERENCE FROM HOT-WIRE ANEMOMETER

INTERNAL CALIBRATION (0.5V)

FIGURE 18. X-Y DISPLAY

REFERENCE FOR STEAM ONLY
L = 3mm (℄) , I_G = 0.1μ A

FIGURE 19. X-Y DISPLAY FROM EGD PROBE

MAIN AIR ONLY (185 ft/s), (v/U_∞ =0.6)

MAIN AIR(185 ft/s), (v/U_∞=.6), NOZZLE AIR (13 PSIG)

FIGURE 20. X-Y DISPLAY FROM HOT-WIRE ANEMOMETER
L = 4mm (℄)

I_G = 0.3μA, MAIN AIR(185ft/s), STEAM(14 PSIG)
4 SECOND INTEGRATION TIME

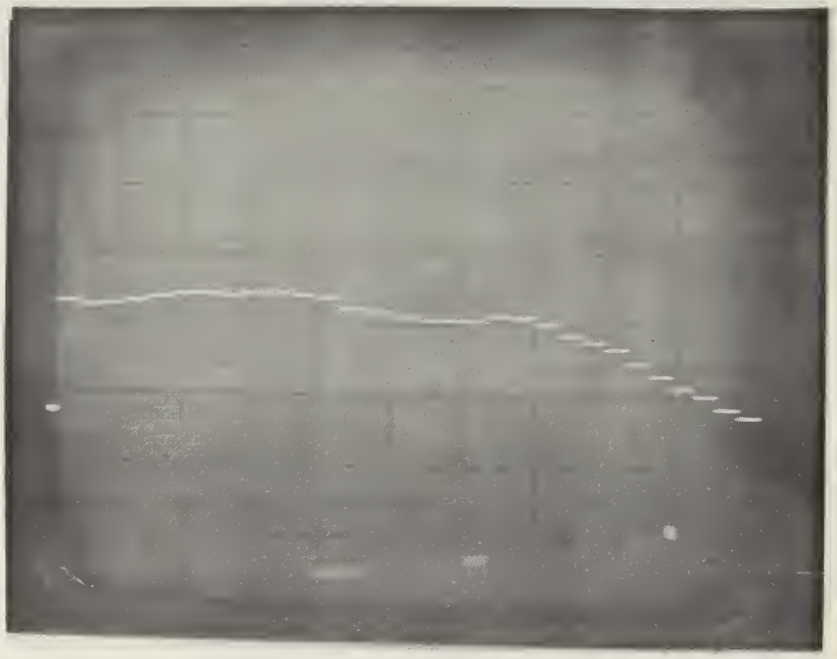

I_G = 0.3 A, MAIN AIR(185ft/s), STEAM(14 PSIG)
8 SECOND INTEGRATION TIME

FIGURE 21. X-Y DISPLAY FROM EGD PROBE—L=4mm (℄)

MAIN AIR ONLY(185ft/s), (v/U_∞ =.6)

MAIN AIR(185ft/s),(v/U_∞=.84) , NOZZLE AIR (13 PSIG)

FIGURE 22. X-Y DISPLAY FROM HOT-WIRE ANEMOMETER
L = 5 mm (℄)

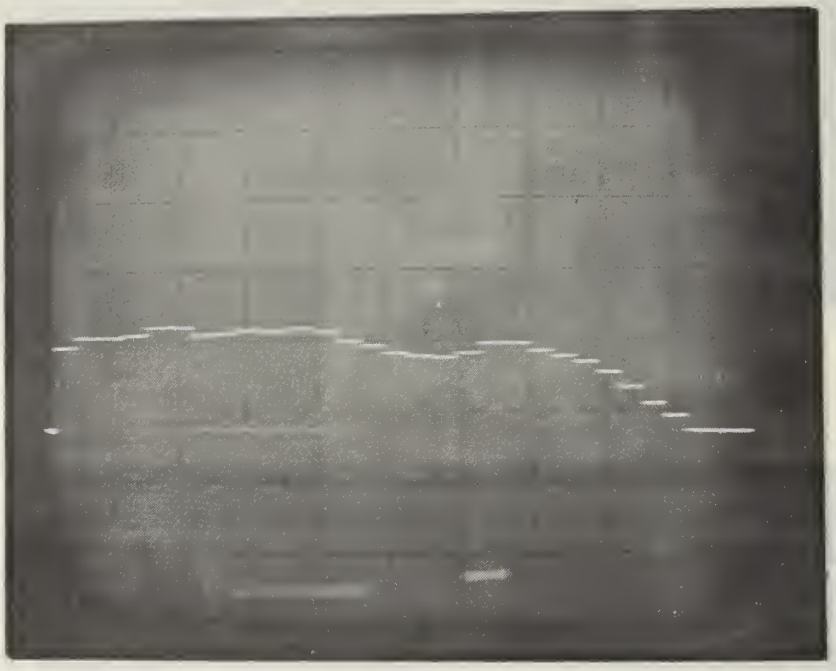

I_G = 0.2μA, MAIN AIR(185 ft/s), STEAM(14 PSIG)

FIGURE 23. X-Y DISPLAY FROM EGD PROBE
L = 5mm (℄)

MAIN AIR ONLY (185 ft/s), ($v/U_\infty = .54$)

MAIN AIR (185 ft/s), ($v/U_\infty = 1.14$), NOZZLE AIR (15 PSIG)

FIGURE 24. X-Y DISPLAY FROM HOT WIRE ANEMOMETER
L = 7mm ($\mathbb{Q}$)

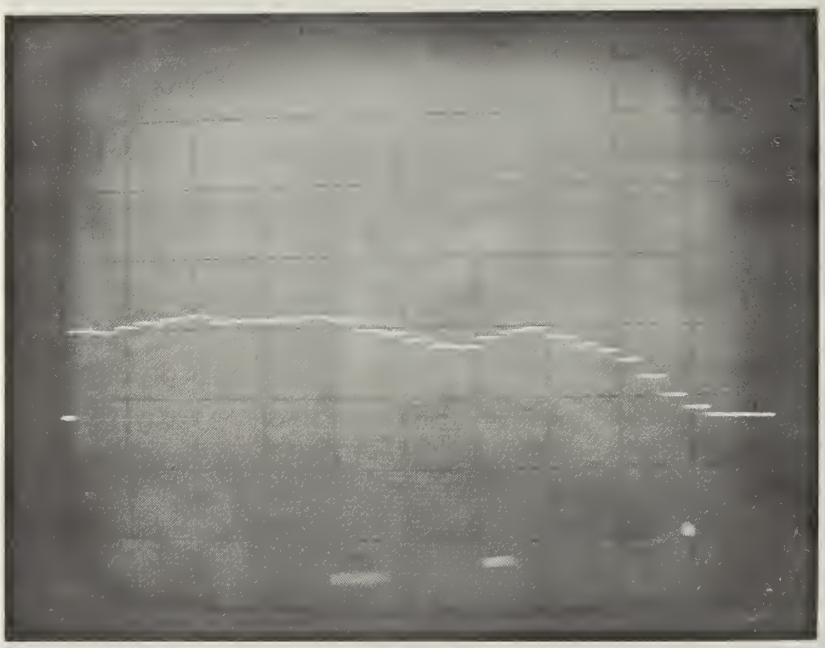

MAIN AIR (185 ft/s), I_G = 0.2μA, STEAM (14 PSIG)

FIGURE 25. X Y DISPLAY FROM EGD PROBE
L = 7 mm (℄)

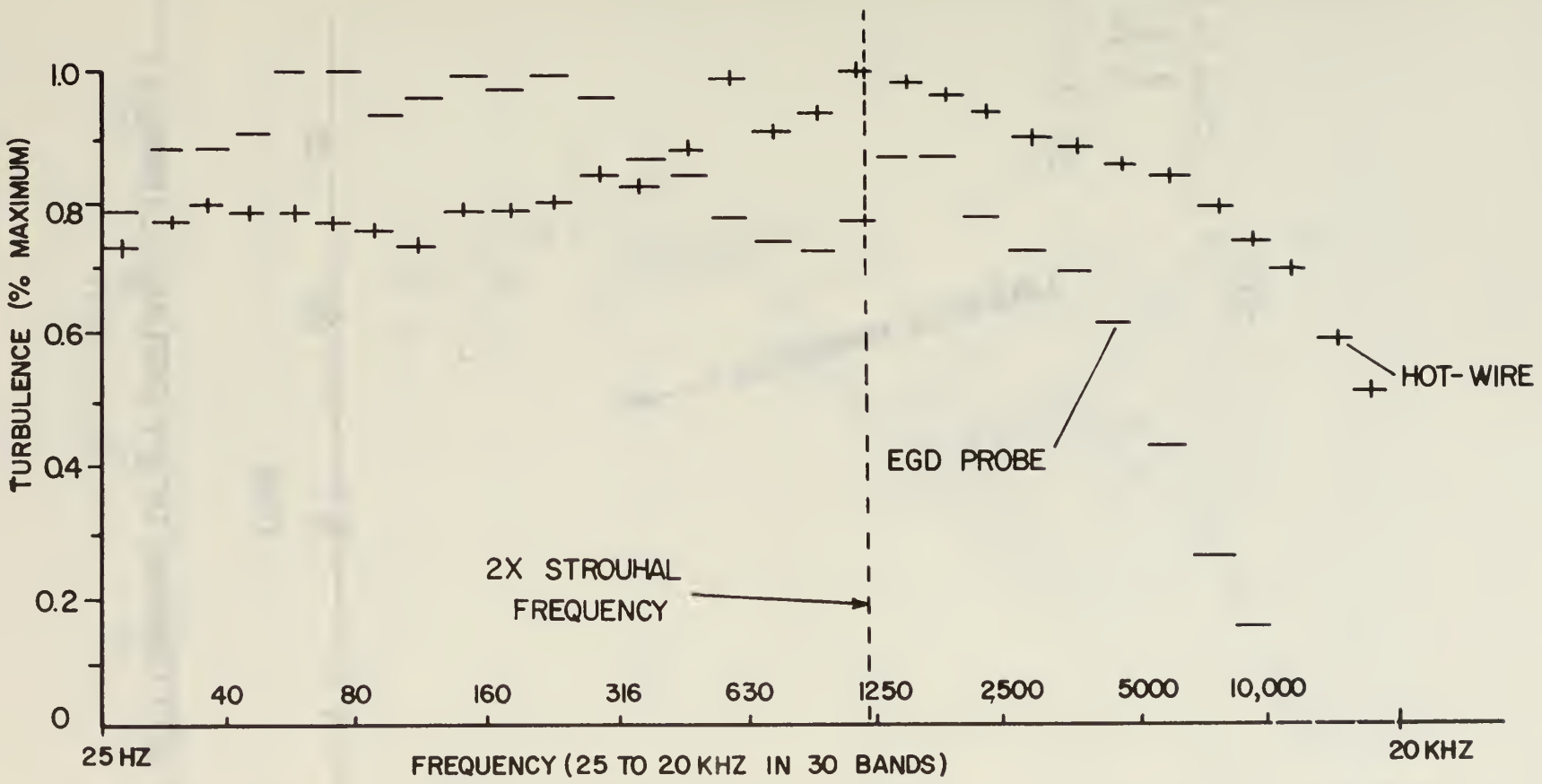

HOT WIRE: MAIN AIR (185 ft/s, $(v/U_{\infty} = .84)$, NOZZLE AIR (13PSIG)

EGD PROBE: $I_G = 0.2\mu A$, MAIN AIR(185ft/s), STEAM (14 PSIG)

FIGURE 26. NORMALIZED X-Y DISPLAYS —— L = 5mm (℄)

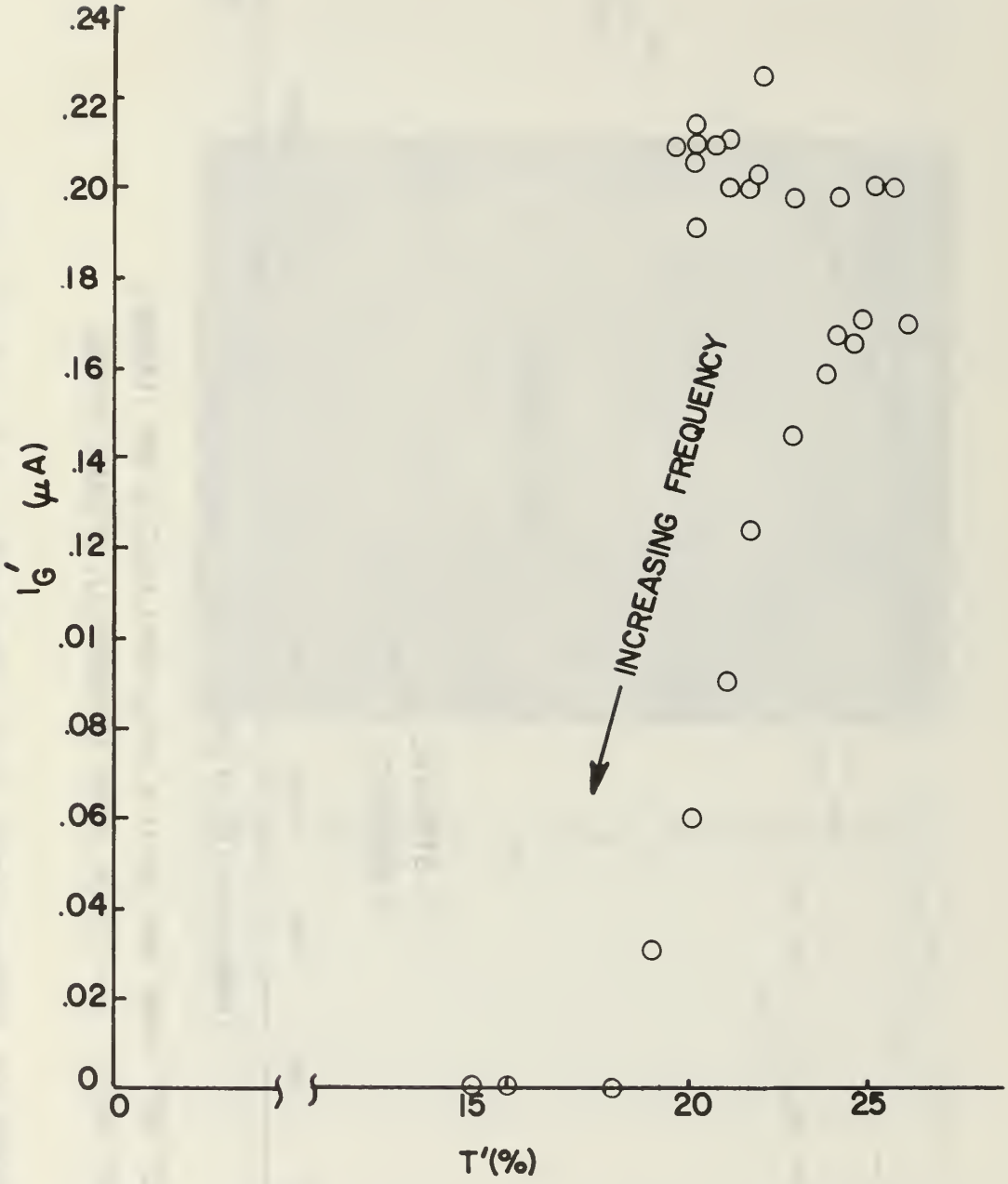

FIGURE 27. SCATTERGRAM OF X-Y DISPLAYS, L = 5mm (℄)

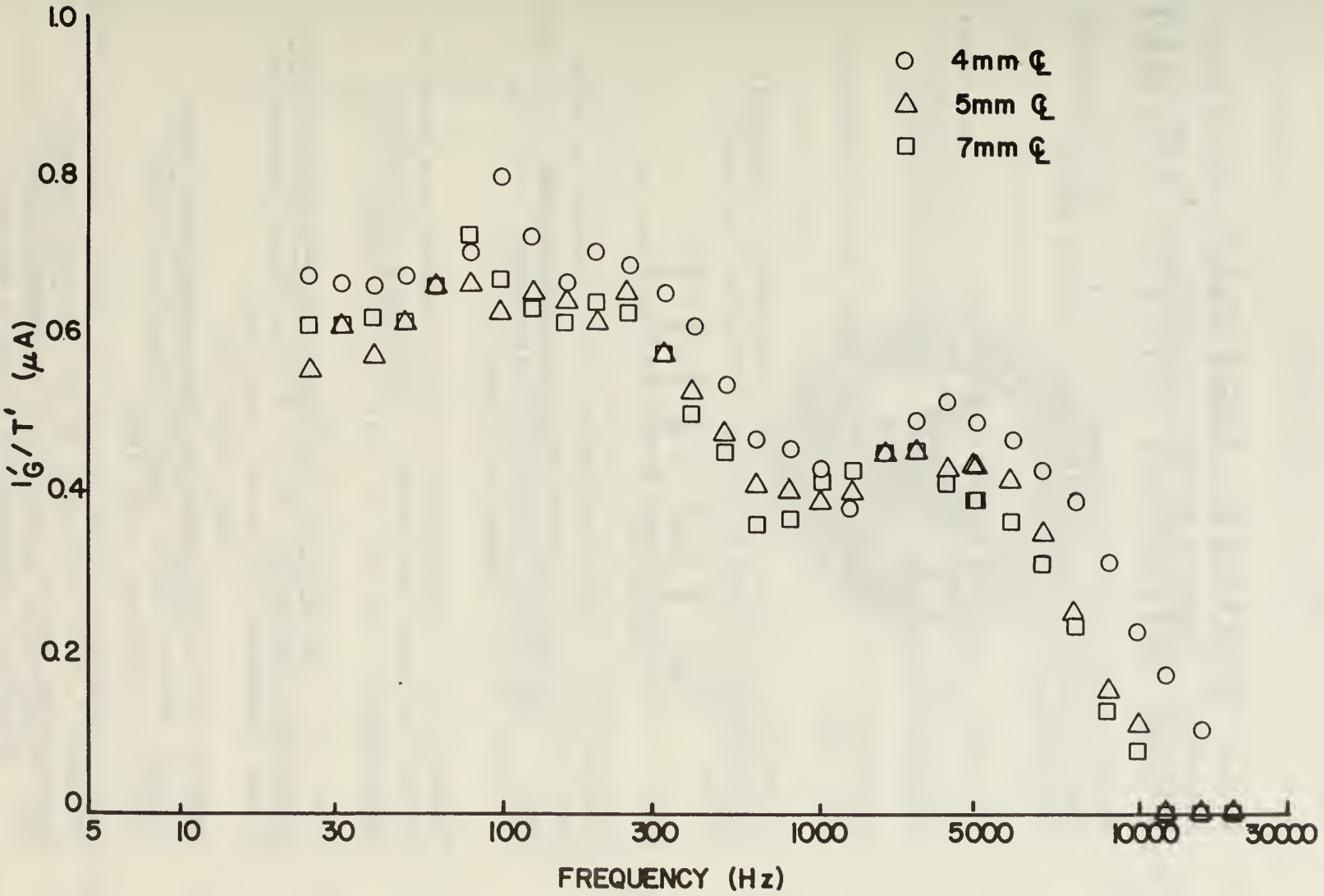

FIGURE 28. FREQUENCY DEPENDENCE OF THE RATIO OF COLLECTOR CURRENT TO TURBULENCE

LIST OF REFERENCES

1. Bennett, W. E., "The Generation of Direct Current at High Potentials," Research Applied in Industry, v. 12, no. 12, December 1959, England.

2. Naval Postgraduate School Report 57ZI9121A, EHD Research Final Report for the Year 1968-69, by Oscar Biblarz, 30 December 1969.

3. Ohio State University Research Foundation, Columbus, Report No. 10, Ad 684 939, Studies of the Effects of Electrostatic Fields on Fluid Flows, by H. R. Velkoff, p. 65-77, 1969.

4. Schlichting, H., Boundary Layer Theory, 4th ed., McGraw-Hill, 1960.

5. Kovasznay, L.S.G., "Hot-Wire Anemometry," Physical Measurements in Gas Dynamics, Princeton University Press, 1954.

6. Hinze, J.O., Turbulence, p. 122-124, McGraw-Hill, 1959.

7. Werner, F.D., "An Investigation of the Possible Use of the Glow Discharge as a Means for Measuring Air Flow Characteristics," The Review of Scientific Instruments, v. 21, no. 1, p. 61-68, January, 1950.

8. Nygaard, K.J., "Anemometric Characteristics of a Wire-to-'Plane' Electrical Discharge," The Review of Scientific Instruments, v. 36, no. 12, 1771-1774, December, 1965.

9. Ober, W.T., Ion Injectors for Single-and Two-Phase Electrogasdynamic Generators, Master Thesis, Naval Postgraduate School, Monterey, California, June, 1969.

10. Wallace, D.W., Molecular-Ion Electrogasdynamic Flow Channel, Master Thesis, Naval Postgraduate School, Monterey, California, June, 1969.

11. Peterson, A.P.G. and Gross, E.E., Handbook of Noise Measurement, 6th ed., p. 273-278, General Radio Company, 1967.

12.. Pao, R.H.F., Fluid Mechanics, p. 111-112, Wiley, 1961.

United States
Naval Postgraduate School

THESIS

Electrogasdynamic Control of Separated Flow,

A Feasibility Study

by

John Peter Segen

June 1970

ABSTRACT

This investigation proposes to determine if electrogasdynamic interactions are feasible for flow separation control. It is shown theoretically that the electric pressure caused by charged particle movement in an electric field produces a pressure increase that is at the lower limit of values needed for flow separation control. The theoretical possibility is also shown using the Navier-Stokes equations with an electric body-force term included.

An experiment is carried out using charged particle injection and acceleration in a separated region beneath a backward-facing step. The experimental results are inconclusive. Recommendations are given to improve the experiment.

TABLE OF CONTENTS

LIST OF TABLES

LIST OF ILLUSTRATIONS

FIGURE

LIST OF SYMBOLS

A = Cross sectional area of duct

A^* = Area of EGD nozzle exit

a = Cylinder radius

b = Ion or charged particle mobility

c = Chord length

E = Electric field intensity

E_b = Breakdown electric field intensity

E_o = Initial electric field intensity

E_x = Electric field intensity in free stream direction

E_y = Electric field intensity normal to free stream direction

I = Current

I_c = Corona current

I_l = Collector current

j = Current density

k = Ratio of specific heats

M = Mass flow rate

p = Pressure

p_a = Ambient pressure

p_g = Gage pressure

p_o = Reservoir pressure

r = Distance from origin in polar coordinates

T = Thrust

U_∞ = Free stream velocity

u = Local velocity in axial direction

v_c = Corona potential

v_1 = Collector potential

v = Local velocity in normal direction

W = Electric potential

x = Axial coordinate

y = Normal coordinate

z = Width coordinate

ϱ = Charge density

ϵ = Dielectric constant

μ = Viscosity

ν = Kinematic Viscosity

θ = Angular coordinate

δ = Mass Density

I. INTRODUCTION

In 1904 Prandtl demonstrated that the extent of a separated flow region about a cylinder could be greatly reduced by suction. Since that time, many boundary layer control devices have been developed and tested. Some of these devices have proved successful, and are currently in use on modern aircraft. The distinguishing characteristics of a successful boundary layer control device are that it be of simple, reliable design and without excessive weight. That is, the total weight of the device, including extra structure required for mounting plus the power generating equipment needed to operate the device, must be less than the lift gained by the use of the device. Applied research in this field proceeds toward the objective of providing the optimum boundary layer control device with regard to benefits obtained, whether it be increased lift or decreased drag, at a minimum weight. With this thought in mind, all practical methods of controlling a boundary layer must be studied. One method that seems possible but needs more study to determine its feasibility is the use of accelerated charged particles as a means of imparting momentum to the stagnant region of a separated flow.

It is not meant to imply that this means of boundary layer control is a completely new idea. The earliest work found, not necessarily the earliest published, in a related area was a master's thesis by Shaar (Ref. 10) in 1947. In this work Shaar shows that the injection of a large number of positive ions into the boundary layer of a diffuser, the walls of which are maintained at floating potential, causes a reduction in height of the boundary layer at the exit. In 1969, Cheng

(Ref. 5) discussed the possibility of reducing separation on an airfoil by using an electric discharge. In this article he states that the pressure gradient in a separated turbulent boundary layer is approximately 10 dynes per cubic centimeter, and that if a corona discharge could exert a pressure of 1000 dynes per square centimeter on the flow the boundary layer would remain attached for about one additional meter downstream. Stuetzer (Ref. 12), in an undated paper, shows a remarkable reduction of the separation on a cylinder and a hydrofoil, which are kept at floating potential, in a flow of kerosene into which ions were injected. Stuetzer also makes use of electric pressure in determining when modifications to the separation pattern can be expected. He uses the ratio of electric pressure to the change in hydrostatic pressure to describe the relative influence of the injected charge, but states that experimental information needed to generalize this parameter to flows other than kerosene are not available.

The idea of viscously coupling particles, of optimal size and charge, has been studied in connection with electrogasdynamic generators (Ref. 7) but it has not been used to control airflows at atmospheric pressure. This project proposes to apply this idea to a subsonic separated airflow. In doing so it specifically endeavors to answer the question: What possibility exists to reduce the extent of separation on an airfoil by adding momentum to the separated region by viscous interaction between electrically accelerated, charged particles and the neutral particles in the separated region?

II. THEORETICAL FEASIBILITY

In recent years much research has been done in the field of electrogasdynamic (EGD) generators. The objective of this work has been to convert the flow energy of a flow into electrical work. This process essentially involves a momentum transfer from the flow particles to the electrically charged particles, which are usually generated by a corona discharge. The momentum gained by the charged particles causes them to move out of the region in which they were produced thereby doing electrical work. They are then collected to close the generator circuit. Although some success has been achieved in these projects the amount of electrical energy made available is generally small (Ref. 4).

A scheme for adding momentum to a separated boundary layer can be devised using a similar principle. Charged particles are injected into the flow in the same manner as an EGD generator and are then accelerated to a velocity higher than the flow velocity by an external electric field. These high velocity particles impart momentum to the stagnant air particles in the separated region by frictional coupling. The momentum gained by the netural air particles will cause a reduction in the extent of the separated region. The efficient injection of the charged particles, which requires a small particle mobility, occurs in the most optimum way for particles of about one micron in radius (Ref. 6,7).

The amount of momentum possessed by a flow of charged particles in an electric field, and hence the maximum amount that can be transferred, can be related to the pressure generated by this flow. This electric pressure can be found (Ref. 13) for a one-dimensional system which, while not realistic, gives a feel for what is happening. Consider the flow of

a dielectric gas into which positive charges are injected and then accelerated as in Figure 1. The dielectric gas is considered incompressible and to be moving at a uniform velocity. At x=0 positive ions of constant mobility b are injected into the flow with a velocity equal to the flow velocity. The ions are accelerated toward the downstream collector under the influence of an electric field of intensity E. This field is generated by an external power supply which causes the potential at x=0 to be W_o, and at x=L to be W_L, where W_o is greater than W_L. The system is operated at a steady state in that all the ions injected at x=0 are collected at x=L and the external current I is constant. The remaining quantities are as given in the list of symbols. The governing equations for this system are

Conservation of Mass

$$\delta u A = \dot{M} \qquad 2\text{-}1$$

Conservation of Charge

$$\rho u A = I \qquad 2\text{-}2$$

Conservation of Momentum

$$\delta u \frac{du}{dx} + \frac{dp}{dx} - \rho E = 0 \qquad 2\text{-}3$$

Poisson's Equation

$$\frac{dE}{dx} = \frac{\rho}{\epsilon} \qquad 2\text{-}4$$

Potential Relation

$$-\frac{dW}{dx} = E \qquad 2\text{-}5$$

Current Density Equation

$$j = \rho(bE + u) \qquad 2\text{-}6$$

Substituting the space charge density as given by Eq. 2-4 into

Eq. 2-6 gives an equation relating the electric field intensity to the current density and the flow velocity,

$$j\,dx = \epsilon b\,(E + \frac{u}{b})\,dE \qquad 2\text{-}7$$

Since the external current is constant, the current density, which for unit depth is just the external current divided by the cross-sectional area of the channel, is a constant. Now, assuming that the flow velocity is independent of the field intensity Eq. 2-7 may be integrated. After evaluation of the constant of integration this equation can be solved for the field intensity to give

$$E = \left[2\,\frac{jx}{\epsilon b} + (E_o + \frac{u}{b})^2\right]^{\frac{1}{2}} - \frac{u}{b} \qquad 2\text{-}8$$

Since frictional effects are neglected, u=U, Eq. 2-10 may be differentiated with respect to x and substituted into Poisson's equation to yield an expression for charge density,

$$\varrho = \frac{j}{b}\left[\frac{2jx}{\epsilon b} + (E_o + \frac{u}{b})^2\right]^{\frac{1}{2}} \qquad 2\text{-}9$$

This equation along with Eq. 2-10 may be substituted into the momentum equation to give a differential expression for the pressure,

$$dp = \left[\frac{j}{b} - \frac{j}{b^2}\,U\left[\frac{2jx}{\epsilon b} + (E_o + \frac{U}{b})^2\right]^{\frac{1}{2}}\right]dx \qquad 2\text{-}10$$

After integrating, evaluating the constant, and simplifying, the pressure change caused by charge movement in the electric field may be written into final form

$$p - p_o = \frac{\epsilon}{2}\,(E^2 - E_o^2) \qquad 2\text{-}11$$

Taking $E_o = 0$ and $E = E_b = 3\times10^6$ volts per meter, the breakdown field for air at normal conditions, and using $\epsilon = 8.86\times10^{-12}$ ampere seconds per

volt meter the maximum pressure change that can be expected is approximately 40 newtons per square meter or 0.835 pounds per square foot.

Cheng (Ref. 5), as previously noted, suggests that a pressure increase of 1000 dynes per square centimeter, which is 100 newtons per square meter, will cause a turbulent boundary layer to remain attached for one additional meter. The maximum electric pressure as calculated above is a sizeable fraction of this value. This would seem to indicate that a significant boundary layer control might be achieved by this method.

If this maximum electric pressure is divided by a suitable dynamic pressure the resulting ratio may be compared to the parameter used by Stuetzer (Ref. 12) to indicate when flow modifications became noticeable in his experiments on flow control. The dynamic pressure chosen is that corresponding to a normal aircraft landing speed of 110 knots. For standard temperature and pressure this is 41 pounds per square foot. This ratio turns out to be about 0.02 while Stuetzer indicates that separation reduction became noticeable for a value of 0.03. Here it would appear that the possibility of causing a significant control is small. However, the comparison is made for two different mediums, air vice kerosene, so a strict comparison is not possible without additional information.

The ratio for air can be improved by increasing the maximum breakdown field strength, and this can be done in a number of ways. One way, which occurs naturally in a separated flow area, is to increase the turbulence level (Ref. 4). Another is the use of chemical additives such as sulphur hexafluoride (SF_6) or Arctron-12 (CCl_2F_2) (Ref. 3).

These compounds act as electron scavengers to decrease the number of free electrons in the field which in turn increases the breakdown field strength by as much as a factor of three. It is interesting to note that an increase in breakdown field strength of approximately seven kilovolts per centimeter (E_b = 37 x 10^6 volts per meter) would increase the ratio of electric pressure to dynamic pressure for air to 0.03, the value cited (Ref. 12) for noticeable separation reduction.

Another means of assessing the possibility of delaying separation by using ions or charged particles is to use the Navier-Stokes equations with an electric body force term included. Consider the two dimensional system as shown in Figure 2 in which positive charges are injected into an incompressible air flow, at the body surface, just upstream from the separation point. The ions are collected at some point downstream after being accelerated by an electric field. The field is generated by an external power supply which causes a potential difference between the injector and the collector. It is assumed that the currents involved are small and that the field effects take place in a small region near the body surface. The extent of this region is of the same order of magnitude as the size of the region in which viscous effects occur in the ordinary boundary layer assumptions. With this assumption, the flow may be separated into two regions, the outer where electric and viscous effects are negligible and the inner region where electric and viscous effects are of comparable size to the pressure and convective terms. The Navier-Stokes equations may then be written for each region

Outer Region

x Direction

$$U \frac{dU}{dx} = -\frac{1}{\delta} \frac{\partial p}{\partial x} \qquad 2\text{-}12$$

y Direction

$$\frac{\partial p}{\partial y} = 0 \qquad 2\text{-}13$$

Inner Region

x Direction

$$u \frac{\partial u}{\partial x} + v \frac{\partial u}{\partial y} = - \frac{1}{\delta} \frac{\partial p}{\partial x} + \frac{\rho}{\delta} E_x + \frac{\nu}{\delta} \frac{\partial^2 u}{\partial y^2} \qquad 2\text{-}14$$

y Direction

$$\frac{1}{\delta} \frac{\partial p}{\partial y} = \frac{\rho}{\delta} E_y \qquad 2\text{-}15$$

From Eq. 2-14 it is concluded that the pressure in the external flow region is independent of y so that the partial derivative of p with respect to x becomes a total derivative. The effects of the electric field in the y direction are small and may be neglected so that the change in pressure across the inner region is zero. As in the ordinary boundary layer approximations this implies that the external or potential flow pressure is impressed across the boundary layer. Right at the body surface both velocity components are zero so that Eq. 2-15 may be written

$$\left| \frac{1}{\delta} \frac{dp}{dx} - \frac{\rho}{\delta} E_x \right|_{\text{wall}} = \left| \frac{\nu \partial^2 u}{\delta \partial y^2} \right|_{\text{wall}} \qquad 2\text{-}16$$

Separation occurs as the magnitude of the viscous term goes through zero. If this term could be made always to stay less than zero, separation could not occur. This can be accomplished if

$$\frac{\rho}{\delta} E_x > \frac{1}{\delta} \frac{dp}{dx} . \qquad 2\text{-}17$$

Since the pressure gradient in the x direction can be related to the convective term of the potential flow, Eq. 2-17 may be written,

$$\frac{\rho}{\delta} E_x > U \frac{du}{dx} . \qquad 2\text{-}18$$

As shown in Appendix A this condition at the surface is the maximum case. At points in the boundary layer away from the wall the convective terms cause a decrease in the value that the electric body force must assume to prevent separation. Thus, satisfying this criterion at the surface suffices for the whole boundary layer height.

To accelerate the boundary layer efficiently, the electric field strength and the charge density must be near the maximum possible. The maximum for each quantity would be that associated with conditions just before breakdown. For air at standard temperature and pressure the breakdown field strength, as given before, is 3×10^6 volts per meter while the breakdown limited charge density is 4.5×10^{-3} coulombs per cubic meter (Ref. 7). Using these values the maximum that the electric body force per unit mass may attain is,

$$\left| \frac{\rho}{\delta} E_x \right|_{max.} = 1.1 \times 10^4 \text{ m/sec}^2 .$$

In Appendix B values for the magnitude of the x component of the pressure gradient are calculated by equating to the potential flow convective term as in Eq. 2-12. This term is calculated for a circular cylinder, a Joukowsky airfoil, and for a NACA 0012 airfoil. These values are respectively 4.93×10^3, 1.33×10^3 and 9.4×10^2, all with units meters per square second. In all three cases the maximum electric body force is approximately an order of magnitude larger than the convective term, or by Eq. 2-12 the pressure gradient.

From this it is seen that the electric body force term can be sufficiently large to cause the viscous term of Eq. 2-16 to stay negative. It is then concluded that it is possible to delay separation on a body in a decelerated flow region by electrogasdynamic interactions provided

the particles can be injected in sufficient quantity and proper size to insure optimum conversion and maximum density, and that early breakdown and current leakage are prevented.

III. EXPERIMENTAL APPARATUS AND EXPERIMENTAL PROCEDURE

A. EXPERIMENTAL APPARATUS

This research was begun with the intention of demonstrating that a region of separated flow on an airfoil could be affected by the injection and acceleration of charged particles, but because of design and test difficulties it was necessary to begin with a test apparatus that was more compatible with the small size of the existing EGD tunnel facility. Since the tunnel is two inches by four inches in the inlet cross section, the airfoil would necessarily have been very thin to preclude tunnel blockage. This would have made it virtually impossible to route supply and instrumentation leads through the model cross section. The thinness of the airfoil would also have eliminated any region of gross separation and the separation point would have been difficult to fix. The apparatus, selected to minimize these problems, finally settled upon was a backward facing step mounted in one wall of the test section as shown in Figure 3. This set up eliminated the above problems since any lines going into it needed only to be routed through the wall, the location of the step fixed the point of separation, and the extent of the separated region was comparable to the step height. While this apparatus solved some of the design difficulties it somewhat changed the method of attacking the question at hand. With an airfoil it was possible to ask if electro-gasdynamic interaction would delay separation, but with the step it was only possible to ask if reattachment could be hastened by these interactions. It was felt that the mechanism of momentum addition needed to cause a reduction in reattachment length was similar to that necessary to cause a separation delay, and that a demonstration of this reduction

could show the feasibility of electrogasdynamic interaction for separation control.

The backward facing step was made as an integral part of a detachable test section wall. Provision was made to mount three electrogasdynamic injector nozzles (Figure 4), of a type designed to produce micron-size charged water droplets (Ref. 8), on the step face to discharge particles downstream. Since these nozzles required a supply of saturated steam, at 250°F, to operate it was necessary to use a material for the step wall that would not only be a good electric and heat insulator but also maintain its strength at this temperature. Teflon filled both of these requirements and was used for the step wall, while plexiglass was used for the remaining three sides of the test section. Two compartments were milled out on the step wall, in the area upstream from the step (Figure 5A), to serve as a common plenum for the three nozzles, and to provide mounting room for the three corona needles. The plenum was sealed with a fiber reinforced phenolic cover into which three fittings, for supply and instrumentation lines, were mounted (Figure 5B). The inside dimensions of the finished test section were 2 by 4 inches in the 3 inch long inlet section, and 2.281 by 4 inches in the 6.25 inch long section downstream of the step. Two interchangeable inner surfaces, as shown in Figures (6A-6B), were made for the downstream section. Both of these were made of 0.094 inch thick teflon sheet, but one was smooth and drilled for pressure taps while the other was tufted with number 30 silk thread in an interlocking one-eighth inch grid pattern covering a three by three inch area immediately downstream of the step. The test section was mounted through a reducer to an air plenum in which screens and honeycombs were installed to reduce the flow turbulence and to insure

flow uniformity (Figure 7).

Tunnel air was supplied by a Carrier three stage centrifugal compressor capable of continuously supplying 4000 cubic feet of air per minute. The EGD nozzles could be supplied either with air from the laboratory's high pressure air supply, or with saturated steam from a commercial steam generator. This generator was extensively reworked to provide clean steam at a higher continuous flow rate. This rework included fabrication of a new boiler and a constant water-level supply valve of stainless steel to replace the mild steel components of the original design. All steel fittings and connections in the supply water and steam lines were replaced with non-ferrous parts. The steam line from the generator to the steam plenum was then wrapped with an electric heating tape and covered with insulation. The output capacity of the unit was increased by installing an additional calrod heating element in the boiler. With these modifications the generator was capable of providing a continuous supply of clean steam while maintaining a plenum pressure of 15 psig. A schematic of air and steam flow is shown in Figure 8.

The corona rings of the three nozzles, mounted at the nozzle exit plane, were connected in series to a Sorensen high voltage power supply capable of supplying 30 kilovolts. The needle of each unit was connected to a common ground. A collector wire (0.015 inch diameter steel piano wire) was mounted across the tunnel 0.3 of an inch downstream from the nozzle exit plane and 0.187 inch from the wall. This collector wire could be maintained at a high positive potential by a Spellman high voltage power supply also capable of producing 30 kilovolts. Both electric power supplies had built-in voltmeters with 0-30 kilovolt scales

and milliammeters with 0-50 milliamp scales but to provide more sensitive current readings, it was necessary to connect externally a Simpson microammeter with a 0-50 microamp scale. On the Sorensen unit, which supplied the corona potential, a Singer electrostatic voltment, which measured 0-40 kilovolts in four steps of 10 kilovolts each calibrated to 1% of full scale, was connected externally to provide finer measurement of the corona voltage. A Simpson microammeter was connected in series between each corona needle and ground. Figure 9 shows a schematic of the electric circuitry.

Thermocouples were installed in the steam plenum and on the electric heating tape to furnish temperature data from these two places. Conventional 0-50 psig pressure gages were used to read out pressure in the nozzle plenum and in the steam and air supply lines. A water manometer, connected to a traversable pitot static tube, was used to measure the flow pressure of tunnel air. A series of 19 pressure taps, at a half inch on either side of the center nozzle, spaced at intervals of one-eighth of an inch, were installed in the wall starting three-eights of an inch downstream from the step. These taps, used to record the static pressure at the wall in the separated regions, were connected to a water manometer bank. A Securities Associates two-channel hot wire anemometer and a traverse unit were available to obtain velocity information. It was necessary to modify the traverse unit by extending the probe arm and to design and construct a positioning track. Details of the experimental setup are shown in Figures 10-12.

B. EXPERIMENTAL PROCEDURE

The procedures developed for this experiment were designed to evaluate how the reattachment point, for the separated flow over the backward facing step, moved as a result of adding momentum to the flow

through the nozzles. Then, by applying this information to the movement caused by an electrogasdynamic interaction, the amount of momentum being supplied by this method could be measured.

Three devices were used to obtain reattachment point information. These were hot-wire surveys, tuft observations, and static wall pressure profiles. It was realized that the hot wire could not be operated in a flow containing water droplets and/or charged particles; therefore, only air was injected through the nozzles during these runs. The tuft observations were intended to give mainly qualitative information but it was hoped that some approximate quantitative information might also be gained from these observations. It was anticipated that the static pressure profiles along the wall in the separated region would give the most accurate information for all types of nozzle flow.

Table 1 gives a summary of the various runs made with the information pertinent to each run. All runs were made with a tunnel air flow dynamic pressure of 20 centimeters of water which corresponds to a free stream velocity of 183 feet per second. I_c is the average corona current, I_L is the collector current and V_c is the accelerator voltage applied to the collector wire.

Run 1 was made to become familiar with the apparatus and to obtain some general information on the extent of the separated region. Run 2 was made to verify the flow uniformity in the inlet section. Run 3 was a series of velocity traverses at $z = \pm 0.5$ (see coordinate system of Figure 13) starting at the step and proceeding downstream past the reattachment point as shown by Run 1. Run 4 was a repeat of Run 3 with air flow through the nozzles and a nozzle plenum pressure of 7.5 psig. Run 5 was done to obtain a series of pressure profiles for various nozzle

plenum pressures to show reattachment point movement. Tuft pattern photos with steam injection through the nozzles were done in Run 6 to accomplish the same purpose. In Run 7 steam at the pressures listed was injected through the nozzles and then the pressures at the wall were recorded. The coronas of the three nozzles were then energized so that each was conducting, accelerator voltage was applied and the readings of the wall pressure taps were again taken.

RUN	NOZZLE FLOW	Plenum Pressure (psig)	I_c	I_L	V_L	Data Taken
1	None	0	0	0	0	Visual Tuft Observations
2	None	0	0	0	0	Hot wire velocity profiles
3	None	0	0	0	0	Hot wire velocity profiles
4	Air	7.5	0	0	0	Hot wire velocity profiles
5	None	0	0	0	0	Pressure profiles
	Air	2.5	0	0	0	" "
	Air	5.0	0	0	0	" "
	Air	7.5	0	0	0	" "
	Air	10.0	0	0	0	" "
	Air	12.5	0	0	0	" "
	Air	15.0	0	0	0	" "
6	None	0	0	0	0	Tuft Photography
	Steam	2.5	0	0	0	" "
	Steam	5.0	0	0	0	" "
	Steam	7.5	0	0	0	" "
7	None	0	0	0	0	Pressure Profiles
	Steam	2.5	0	0	0	" "
	Chgd. part.	2.5	28	50	8	" "
	Steam	5.0	0	0	0	" "
	Chgd. part.	5.0	28	50	8	" "
	Steam	7.5	0	0	0	" "
	Chgd. part.	7.5	28	50	8	" "

TABLE 1

SUMMARY OF EXPERIMENTAL PROCEDURE

V. RESULTS AND CONCLUSIONS

A. RESULTS

The observation of the tuft pattern made during the first run showed a fairly well defined reattachment line across the wall at about 1.375 inches downstream from the step. Since the line was straight, it appeared that the presence of the nozzles on the step was washed out due to turbulent mixing. This value for the reattachment distance was later used as a guide in locating the reattachment point with the velocity surveys.

Velocity traverses made in the inlet section show the flow to be uniform and to have a flat profile (Figure 14) similar to the profile that would be expected on a flat plate. This occurs for flow in an inlet of a rectangular duct that is not fully developed. Fully developed turbulent flow in an inlet section cannot be expected for at least 25 hydraulic diameters from the inlet, and in this case the complete inlet section was only about one hydraulic diameter long. The flow is assumed to be turbulent in the inlet since previous tests of a similar test section show the turbulent intensity of the flow at the inlet to be 0.14% and the boundary layer to be growing according to the 1/7th power law. At the step the profiles have developed a slight bulge near the wall (Figure 15A-B) so that a maximum velocity of 1.01 times the center-line velocity occurs at 0.25 inches from the wall. This is attributed to the influence of the lower pressure in the separated region below the step.

A minimum velocity existed, in each velocity survey made in the separated region, at some distance away from the wall. The (x,y) coordinates of this minimum velocity of each profile are shown in Figure 16.

A separated area behind a backward facing step is characterized by a two-dimensional recirculation velocity (Ref. 1) that runs upstream parallel to and near the wall and downstream next to the expanding channel flow. The existence of this minimum is interpreted as indicating that the velocity decreases to zero near the center of the separated region and then goes to some negative value near the wall. The point where the minimum velocity occurred at the wall (there was no inflection in the profile) was taken as the point of reattachment. This occurred for the condition of no nozzle flow at x = 1.37 inches and for a nozzle flow of air, at 7.5 psig plenum pressure, at x = 1.01 inches. The reattachment occurs for both cases at the same downstream point for z = $\pm$0.5 as shown in Figures 17-20.

As described in Ref. 1, a stall region downstream of a backward facing step has an over-all length of separation based on the point where the edge of the expanding flow first contacts the wall. This point is a short distance downstream from the end of the two-dimensional recirculation region. This is shown in Figure 21 which is taken directly from Ref. 1. The nomenclature "first point of reattachment" and "re-attachment point" is new and will be used hereafter in describing these points. The data obtained from the velocity surveys are correlated with the first point of reattachment since it occurs immediately after the region of recirculation flow.

The data obtained from the static pressure taps show a negative velocity just below the step which gradually increases to a maximum positive pressure and then drops off. To analyze what is happening here, it is helpful to look at Figure 21. In the three-dimensional flow region and the recirculation region there is a flow velocity near the wall.

Hence in these regions the static pressures will be negative. Just before the first point of reattachment the pressure will go to zero since there will be a point of zero flow velocity. Between the first point of reattachment and the reattachment point more of the channel flow will impinge on the wall causing an increase in pressure. At the reattachment point this pressure will be a maximum and will gradually decrease as the flow realigns to become nearly parallel again.

The pressure profiles for the separated flow and for the separated flow with air injection through the nozzles at various pressures are shown in Figure 22. The x-coordinate of the first point of reattachment and that of the reattachment point are cross plotted from Figure 22 onto Figure 23 which has as ordinate the thrust produced by the three nozzles per unit nozzle exit area. The method of calculating the thrust produced by these nozzles is shown in Appendix C.

Since the movement of the reattachment points was more pronounced at the lower values of thrust addition it was decided to operate at these lower values for steam and charged particle injection.

The next run was made using the tufted inner wall and injecting steam to find out how valuable this measurement technique was. As can be seen from Figures 24-25, the information was mostly qualitative. The reattachment line was much clearer in an airflow since the steam wet the threads so that they were not as sensitive when steam was injected.

The pressure profiles obtained with the steam injection are shown plotted as smooth curves in Figure 26. Immediately after the data were obtained with the steam injection at each plenum pressure setting, the corona units were energized to two kilovolts and adjusted for operating at steady currents. The corona currents were different on each nozzle,

being approximately 50, 25, and 10 microamps respectively on nozzles 1, 2, and 3. However, the spacing of the needles was so critical in regard to corona current that this range was the best that could be obtained with the apparatus. The accelerator potential on the collector was raised to 8 kilovolts, the highest that could be maintained without breakdown. The collector current for this condition was about 50 microamps. Then the static pressures along the wall were read again. These values are plotted as points on Figure 26. As can be seen most of these points fall right on the associated curve so that no change is evident. In order to determine if a change in these static pressure values was taking place that was smaller than the least count of the manometer board (0.1 centimeters of water or 0.205 pounds per square foot), a micromanometer that measured to the nearest 0.01 centimeters of water was connected to various taps. The fluctuation of the setup was approximately 0.08 centimeters of water and at no time did the injection and acceleration of the charged particles cause a pressure change greater than 0.05 centimeters of water. The manometer change associated with the maximum electric pressure of 0.835 pounds per square foot is 0.4 centimeters of water.

B. CONCLUSIONS

The experimental values of charge density and breakdown field intensity with steam injection as calculated in Appendix D are 6.4×10^{-4} coulombs per cubic meter and 8.5×10^{5} volts per meter respectively. These values were found using the assumption of a homogeneous one-dimensional field. The breakdown field strength is lower than that cited previously because the experimental field was not actually one-dimensional and homogeneous, and because a space charge was present. The breakdown

field for this apparatus in quiet air is 11.6×10^5 volts per meter so that the increase in breakdown field strength due to turbulence is not evident, possibly due to the presence of moisture.

The charge density calculated from Poisson's equation, which is done without assuming a particle size or mobility, is very close to the charge density calculated from the current density equation, which was done assuming a 1 micron particle radius. This implies that the EGD injector nozzles are producing particles which can be efficiently coupled to a viscous flow. In fact, the greatest proportion of the collector current obtained was due to the convective movement of the particles as seen by noting that the mean flow velocity was 384 meters per second while the drift velocity was only 4 meters per second.

The electric pressure that was calculated from the experimental field intensity corresponds to a manometer change of 0.03 centimeters of water. Thus, the pressure that was generated by the charged particle drift velocity was completely lost in the pressure fluctuations due to the turbulent component of the flow velocity. This can also be seen by noting the great difference in mean flow velocity and drift velocity.

Therefore, it is concluded that no movement of the reattachment point was observed because the magnitude of the momentum addition due to electrogasdynamic interaction was too small to cause a detectable change.

The backward facing step provides a well-defined separated region. The reattachment point for this kind of separated flow is quite sensitive to momentum addition. The movement of the reattachment point was four inches per pound of injected thrust for low thrust levels, but decreased rapidly as the injected thrust increased. This damping out of the reattachment point movement was due to the fact that the discharge area

was only a small fraction of the step area and that at higher thrust levels the injected flow became more turbulent and less efficient in imparting momentum in a downstream direction.

VI. RECOMMENDATIONS

The experiment should be redesigned to allow operation in the region where small values of injected momentum cause large changes in the reattachment length. This could be done in a setup using a flow of air, saturated with water vapor, over a backward-facing step. A corona discharge device could be mounted in the separated area immediately downstream of the step. This device should not require steam injection to operate it, thus eliminating the movement of the reattachment point by any means other than EGD interactions. Part of the device might even be on the face, for instance a wire on the face and a half cylindrical screen slightly downstream. The saturated air entering this separated area would condense in the region of the discharge and obtain a charge. A field applied between the corona and some downstream collector would cause these particles to be accelerated toward the collector. Care should be taken to keep the field as one-dimensional as possible to ensure a breakdown intensity near maximum. This would also allow the attainment of higher charge densities. The area that the corona discharges into should be of the same size as the step face.

It would be worthwhile to make an investigation of reattachment point movement by injection beneath various height steps. This investigation might indicate a particular size step that was more sensitive to momentum injection. In this investigation a more thorough survey of the separated area could be made to find the extent of the three-dimensional region (Figure 22) immediately downstream of the step (Ref. 1), to determine if a particular location or configuration of corona device could take advantage of this flow.

The pressure taps along the wall were the only reliable means of obtaining reattachment point information with steam injection but they had a tendency to become plugged because of condensation inside the taps. A multiple trap arrangement should be constructed so that each pressure tap is connected to the manometer through a trap. These traps would collect the condensate without allowing the taps themselves to become plugged. Another solution to this problem would be to make the taps out of teflon tubing. Since teflon is a poor conductor, the steam would not condense in them as it does in metal tubes. Then mount the test channel with the step at the top. Since water does not "wet" teflon, the condensate that forms in the teflon tubes would then fall out. A third solution would be to use a series of pressure transducers mounted in the wall.

APPENDIX A

EFFECT OF CONVECTIVE TERMS

It has been shown that the value of the electric body force term to prevent separation at the body surface is

$$\left| \frac{\varrho E_x}{\delta} \right| > \left| \frac{1}{\delta} \frac{dp}{dx} \right| \qquad \text{A-1}$$

At a position in the boundary layer away from the wall and at the same stream-wise distance, the x-momentum equation is

$$\frac{1}{\delta} \frac{dp}{dx} - \frac{\varrho}{\delta} E_x + u \frac{\partial u}{\partial x} + v \frac{\partial u}{\partial y} = \nu \frac{\partial^2 u}{\partial y^2} \qquad \text{A-2}$$

This equation can be rewritten using the continuity equation

$$\frac{\partial u}{\partial x} + \frac{\partial v}{\partial y} = 0 \qquad \text{A-3}$$

Then equation B-2 becomes,

$$\frac{1}{\delta} \frac{dp}{dx} - \frac{\varrho}{\delta} E_x - u \frac{\partial v}{\partial y} + v \frac{\partial u}{\partial y} = \nu \frac{\partial^2 u}{\partial y^2} \qquad \text{A-4}$$

which can be written,

$$\frac{1}{\delta} \frac{dp}{dx} - \frac{\varrho}{\delta} E_x - u^2 \frac{\partial}{\partial y} \left(\frac{v}{u} \right) = \nu \frac{\partial^2 u}{\partial y^2} \qquad \text{A-5}$$

As before, no separation can occur if the term on the right hand side stays negative. The quantity in parenthesis is negative by equation A-1 and is made more negative by the last term since v/u is the stream-line slope which increases from zero at the body surface to a maximum at the boundary layer edge as seen from the flat plate solution (Ref. 9). Then the criterion for prevention of separation at points away from the body is

$$\left| \frac{\varrho E_x}{\delta} \right| > \left| \frac{1}{\delta} \frac{dp}{dx} - v^2 \frac{\partial}{\partial y} \left(\frac{v}{u} \right) \right| \qquad \text{A-6}$$

which is less stringent than the requirement at the wall.

APPENDIX B

CALCULATION OF THE PRESSURE
GRADIENT TERM OF THE NAVIER-STOKES EQUATION

1. Circular Cylinder

For the potential flow about a right circular cylinder the flow velocity is given by (Ref. 14)

$$U^2 = U_\infty^2 \left[1 - \frac{a^4}{r^4} + 2\frac{a^2}{r^2}\left(\sin^2\theta - \cos^2\theta\right)\right] \qquad \text{B-1}$$

where a is the cylinder radius and $\sin\theta = \frac{y}{r}$ and $\cos\theta = -\frac{x}{r}$.

Then for the velocity at the surface, where r=a,

$$U^2 = 2\,U_\infty^2 \left[1 + \left|\frac{y^2 - x^2}{x^2 + y^2}\right|\right] \qquad \text{B-2}$$

Differentiating this quantity with respect to x,

$$2\,U\frac{du}{dx} = 2\,U_\infty^2 \left[\frac{(x^2 + y^2)(-2x) - (y^2 - x^2)\,2x}{(x^2 + y^2)^2}\right] \qquad \text{B-3}$$

Simplifying this expression and relating it to the pressure gradient,

$$\frac{1}{\rho}\frac{dp}{dx} = -U\frac{du}{dx} = 4\,U_\infty^2\frac{x\,y^2}{r^4} \qquad \text{B-4}$$

Choosing a cylinder of unit radius and a free stream velocity of 110 kts or 56 meters per second B-4 may be rewritten in terms of .

$$\frac{1}{\rho}\frac{dp}{dx} = -1.25 \times 10^4 \cos\theta \sin^2\theta \qquad \text{B-5}$$

The maximum value of this equation is found in the usual way to occur at $\theta = 125.7^\circ$ where $\cos\theta = -0.58$, $\sin\theta = 0.82$. Then the maximum magnitude of the pressure gradient is

$$\left(\frac{1}{\rho}\frac{dp}{dx}\right)_{max} = 4.93 \times 10^3 \ \text{m/sec}^2 \qquad \text{B-6}$$

2. Joukowsky Airfoil

The value of the pressure gradient for this case is calculated by using graphical data as found in Ref. 7. Separation occurs at x = 0.47C and at this point the slope of the graph of dimensionless velocity versus dimensionless chord-wise distance is

$$\frac{d\left|\frac{U}{U_\infty}\right|}{d\left|\frac{x}{c}\right|} = -0.36$$ and the value of

the velocity at this point is $U = 1.1U_\infty$. Then approximately

$$U\frac{dU}{dx} = -0.435\frac{U_\infty^2}{c} \qquad \text{B-7}$$

but, as before,

$$\frac{1}{\delta}\frac{dp}{dx} = -U\frac{du}{dx} = 0.435\frac{U_\infty^2}{c} \qquad \text{B-8}$$

Using U_∞ = 56 meters per second and c = 1 meter, the pressure gradient near the separation point is approximately

$$\frac{1}{\delta}\frac{dp}{dx} = 1.33 \times 10^3 \text{ m/sec}^2$$

3. NACA 0012 Airfoil

In Ref. 2 on page 321, $\left(\frac{U}{U}\right)^2$ versus $\left(\frac{x}{c}\right)$ is plotted for an NACA 0012 airfoil. The slope of this curve is approximately constant from $\frac{x}{c}$ = 0.2 to $\frac{x}{c}$ = 0.8 at

$$\frac{d\left|\frac{U}{U_\infty}\right|^2}{d\left|\frac{x}{c}\right|} = -0.6$$

Performing the indicated differentiation and simplifying,

$$U\frac{dU}{dx} = -0.3\frac{U_\infty^2}{c} \qquad \text{B-9}$$

Then using U=56 meters per second and c=1 meter

$$\frac{1}{\delta}\frac{dp}{dx} = 9.4 \times 10^2 \text{ m/sec}^2.$$

APPENDIX C

CALCULATION OF NOZZLE THRUST

The thrust produced by a flow through a convergent nozzle is given by (Ref. 11),

$$\frac{T}{A^*} = 2\left[\left(\frac{2}{k+1}\right)^{\left(\frac{1}{k-1}\right)}\right] p_o - p_a \qquad C\text{-}1$$

Denoting the nozzle plenum pressure by p_g to indicate that it is a gage pressure, this expression may be written in terms of the gage pressure in the plenum as

$$\frac{T}{A^*} = 2\left[\left(\frac{2}{k+1}\right)^{\left(\frac{1}{k-1}\right)}\right] p_g + 2\left[\left(\frac{2}{k+1}\right)^{\left(\frac{1}{k-1}\right)} - 1\right] p_a \qquad C\text{-}2$$

For steam with $k=1.33$ and $p_a=14.7$ psi, this becomes

$$\left(\frac{T}{A^*}\right)_s = 1.264p_g + -.264p_a \qquad C\text{-}3$$

For air with $k=1.4$ and $p_a = 14.7$ psi, it is

$$\left(\frac{T}{A^*}\right)_A = 1.246p_g + 0.246p_a \qquad C\text{-}4$$

Table II shows the thrust per unit discharge area developed at each plenum pressure used.

TABLE II

THRUST DEVELOPED BY CONVERGENT NOZZLE FOR AIR AND STEAM AT VARIOUS PLENUM PRESSURES

Plenum Pressure (psig)	T/A* Air (psi)	T/A* Steam (psi)
2.5	6.72	7.04
5.0	9.83	10.20
7.5	12.94	13.36
10.0	16.05	16.52
12.5	19.16	19.68
15.0	22.27	22.84

APPENDIX D

CALCULATION OF ELECTRIC BODY FORCE AND PRESSURE FROM EXPERIMENTAL VALUES

Breakdown occurred between the collector and the corona ring at a collector potential of 8.5 kilovolts and a corona potential of 2.0 kilovolts. The distance separating the ring and the collector is 7.62×10^{-3} meters. The linear homogeneous breakdown intensity is then,

$$\left|E_b\right| = \frac{dW}{dx} = 8.5 \times 10^5 \ \frac{\text{volts}}{\text{meter}} \qquad \text{D-1}$$

The the electric pressure due to this field is,

$$p = \frac{\epsilon}{2} E_b^2 = 3.2 \ \frac{\text{newt}}{\text{meter}^2} = 0.067 \ \frac{\text{pounds}}{\text{feet}^2} \qquad \text{D-2}$$

From Poisson's equation the charge density is,

$$\rho = \epsilon \frac{dE}{dx} = 9.9 \times 10^{-4} \ \frac{\text{coulombs}}{\text{meter}^3} \qquad \text{D-3}$$

The charge density can also be calculated using the current density equation,

$$\frac{I_c}{A} = \rho (bE+u) \qquad \text{D-4}$$

Assuming that the EGD injector nozzles are operating at design conditions, so that they are injecting singly charged particles of 1 micron radius, the particle mobility will be 5×10^{-6} square meters per volt second (Ref. 4). From this the drift velocity is 4.25 meters per second. The flow velocity at nozzle exit is sonic and may be calculated (Ref. 11) to be 384 meters per second. As seen from Figures 24-25 the discharge jet width increases only slightly from exit to collector wire. With the drift velocity very much smaller than the flow velocity the one-dimensional continuity equation holds approximately. Thus, using an exit velocity of 384 meters per second, an exit area of 4.64×10^{-4}

square meters the charge density is,

$$\rho = 2.8 \times 10^{-4} \frac{\text{coulombs}}{\text{meter}^3} \qquad \text{D-5}$$

This compares favorable to the value found from Poisson's equation,

Using an average of these two charge densities to compute the electric body force,

$$\frac{\rho}{\delta} E_b = 4.4 \times 10^2 \frac{\text{meters}}{\text{seconds}^2} \qquad \text{D-6}$$

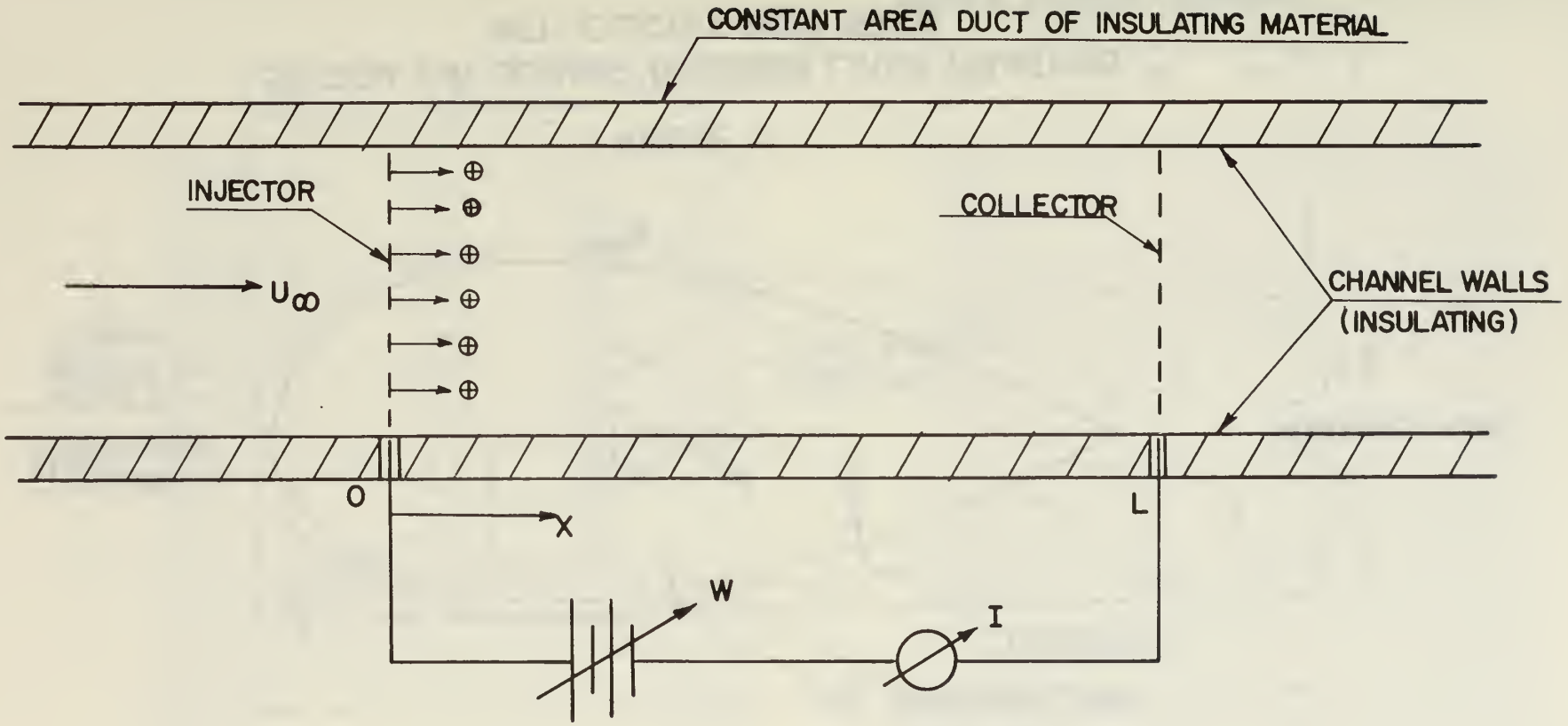

FIGURE 1

SYSTEM FOR DEVELOPING ELECTRIC PRESSURE.

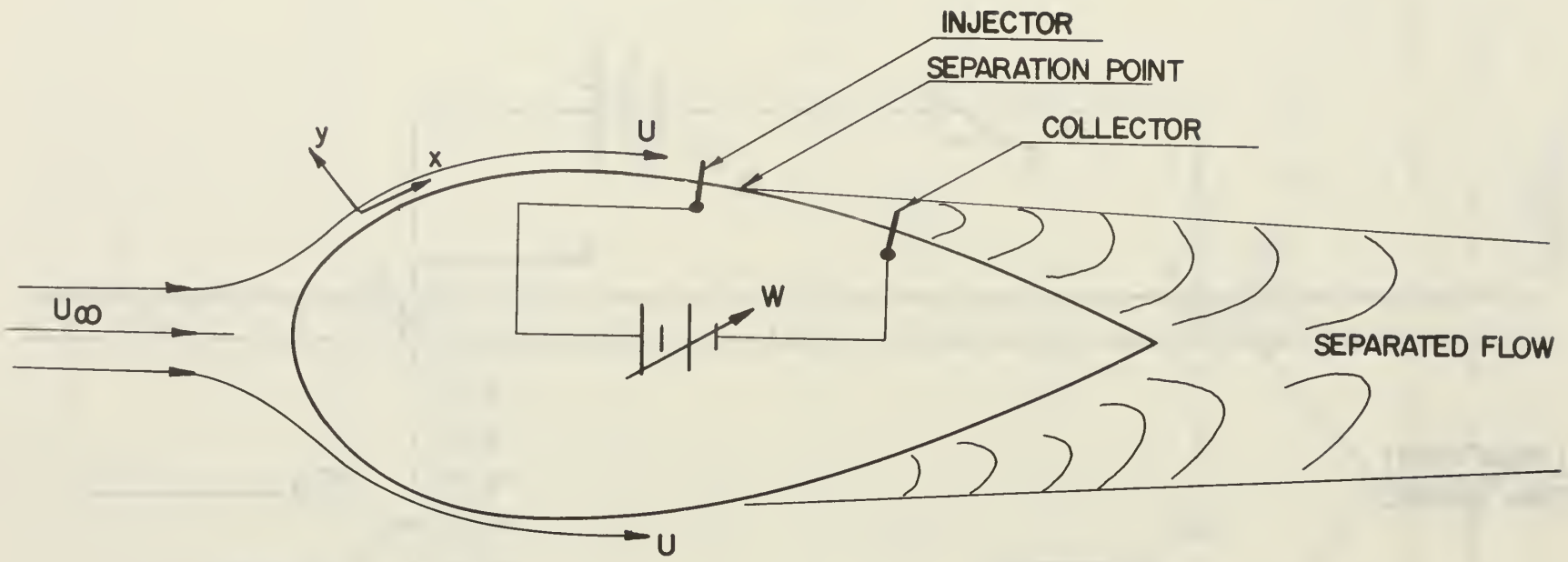

FIGURE 2

SYSTEM FOR DERIVING BOUNDARY LAYER EQUATIONS
WITH ELECTRIC BODY FORCE.

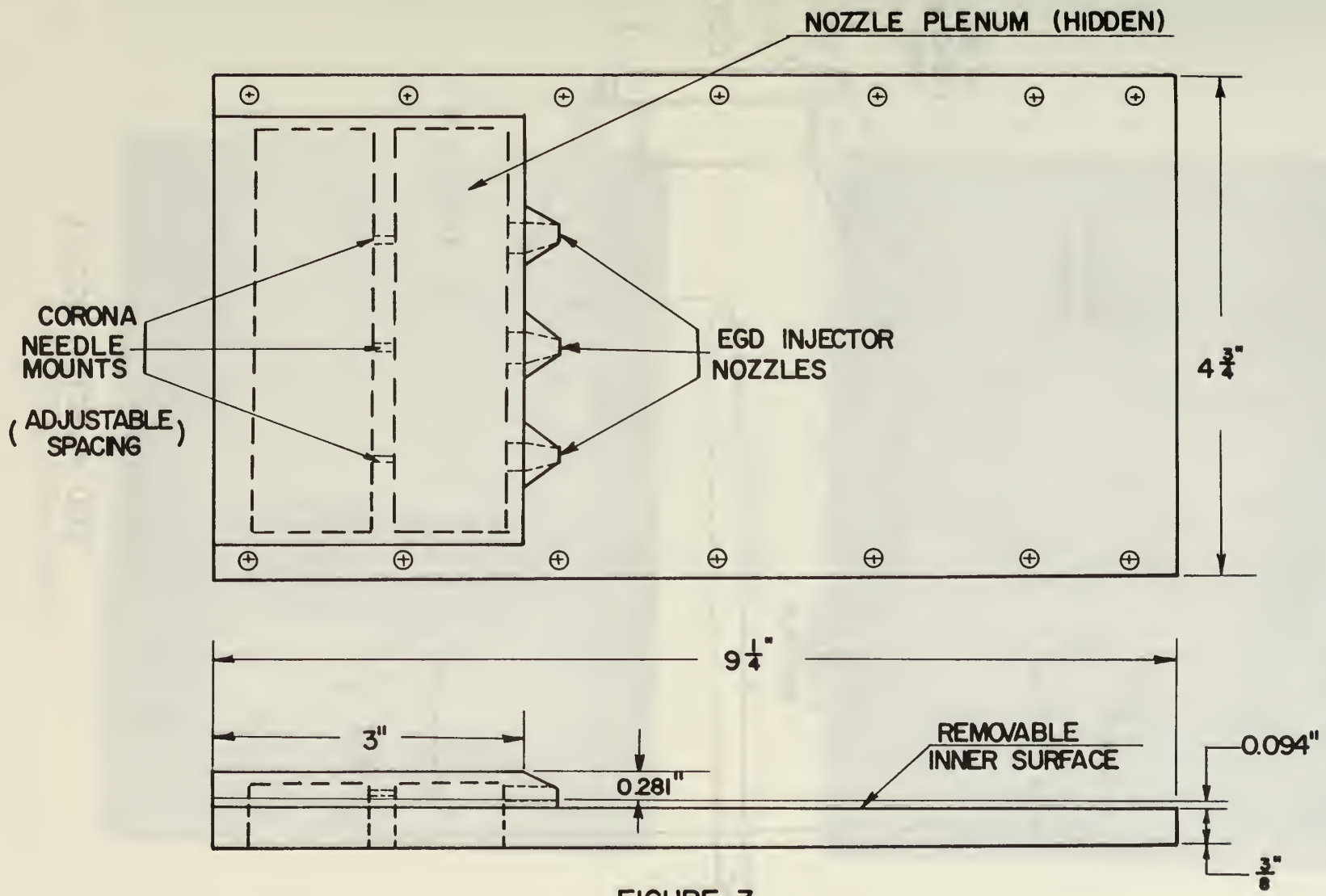

FIGURE 3

STEP WALL INSERT.

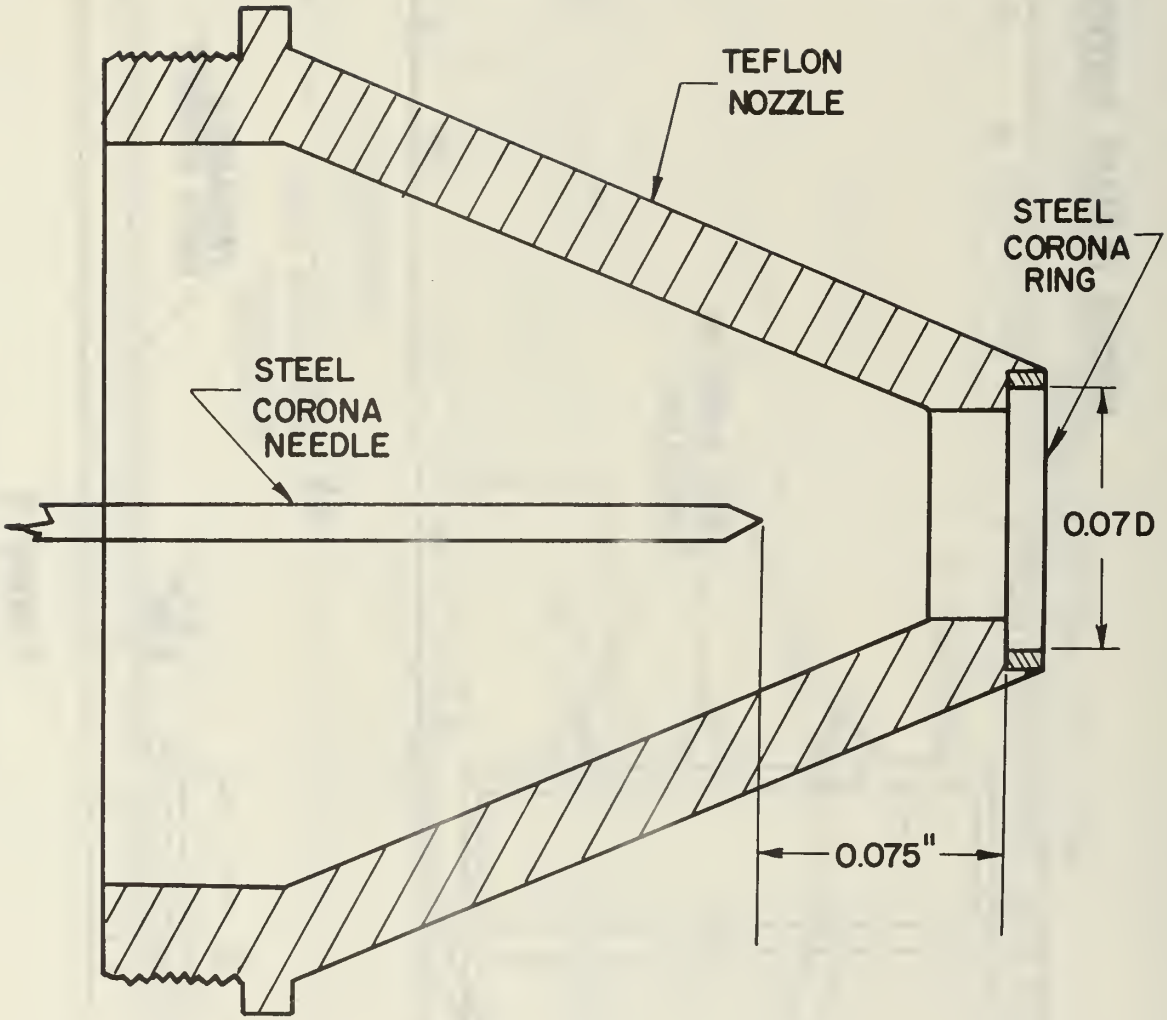

FIGURE 4

EGD INJECTOR NOZZLE

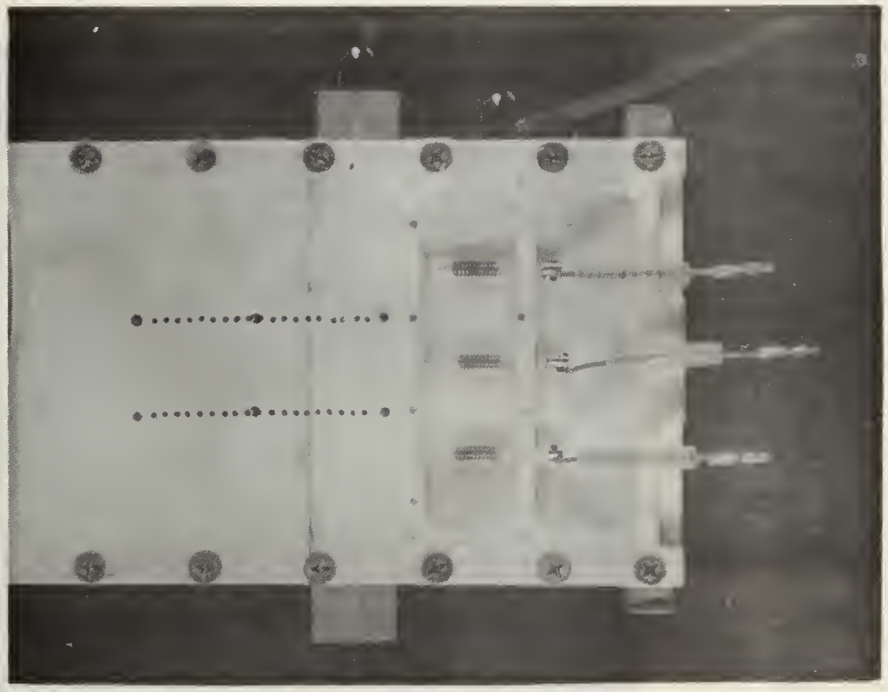

FIGURE 5A NOZZLE PLENUM

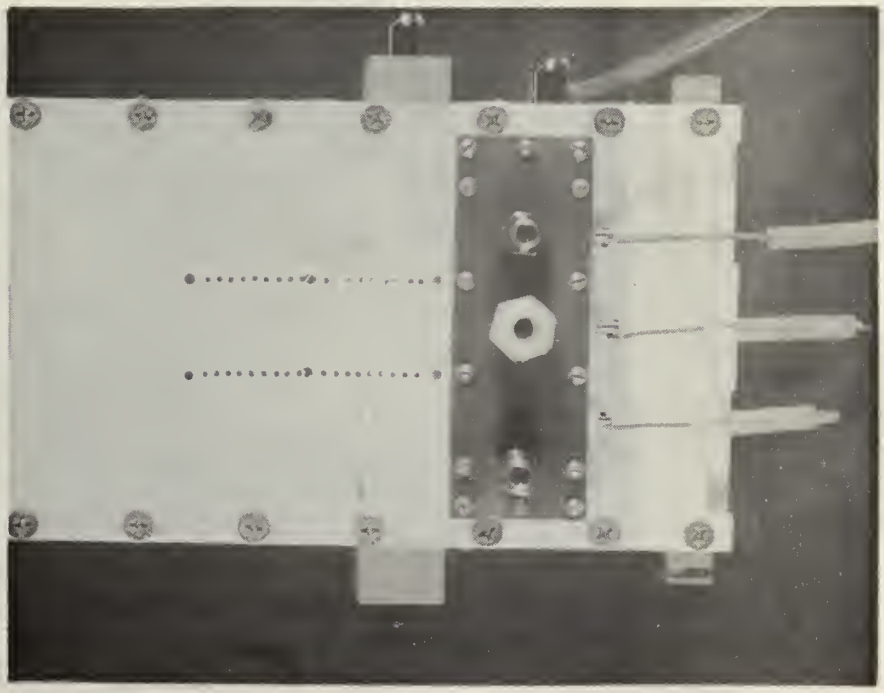

FIGURE 5B NOZZLE PLENUM COVER

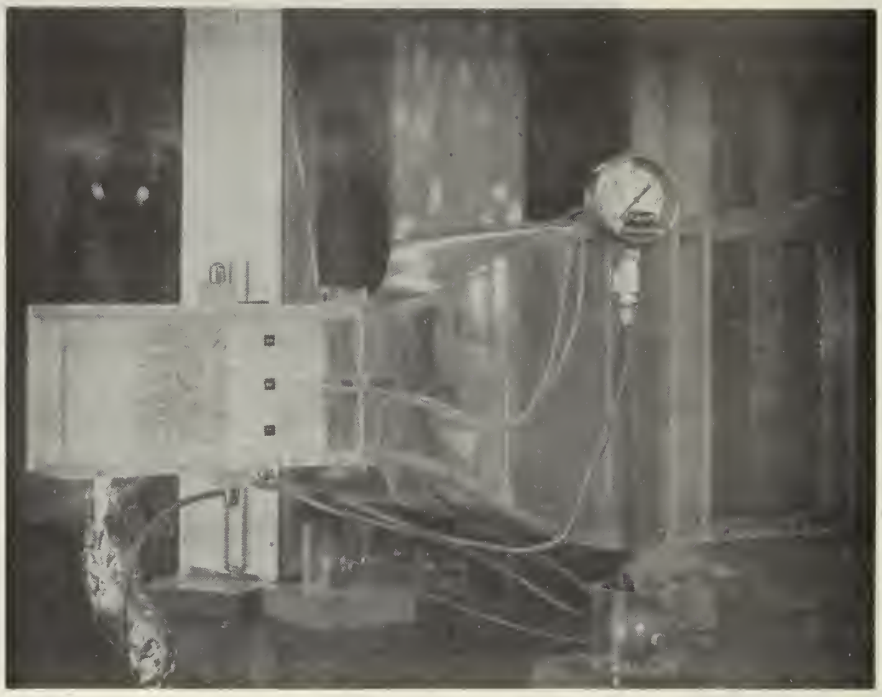

FIGURE 6A SECTION WITH TUFTED WALL

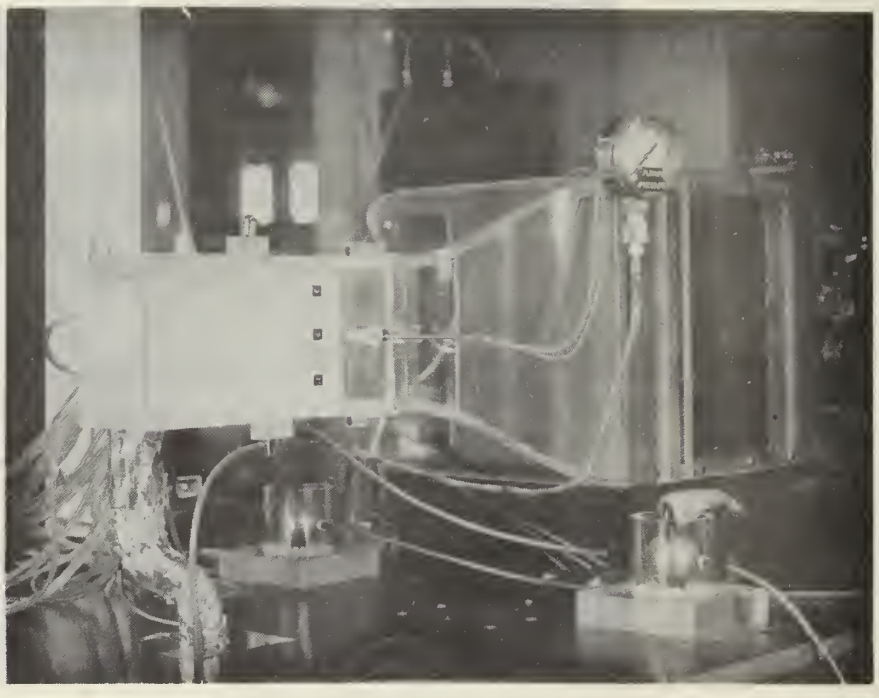

FIGURE 6 B SECTION WITH SMOOTH WALL

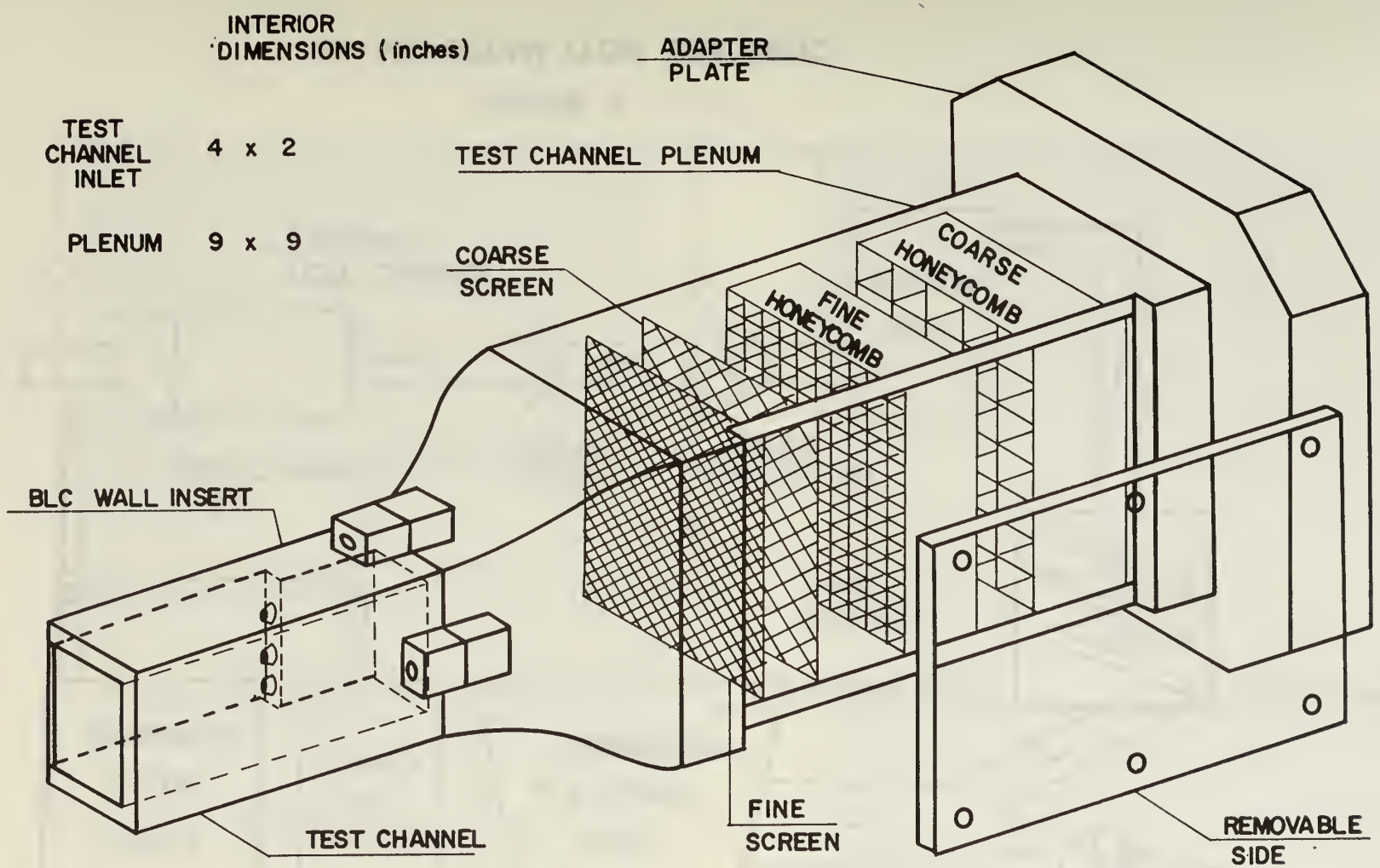

FIGURE 7
TEST SECTION

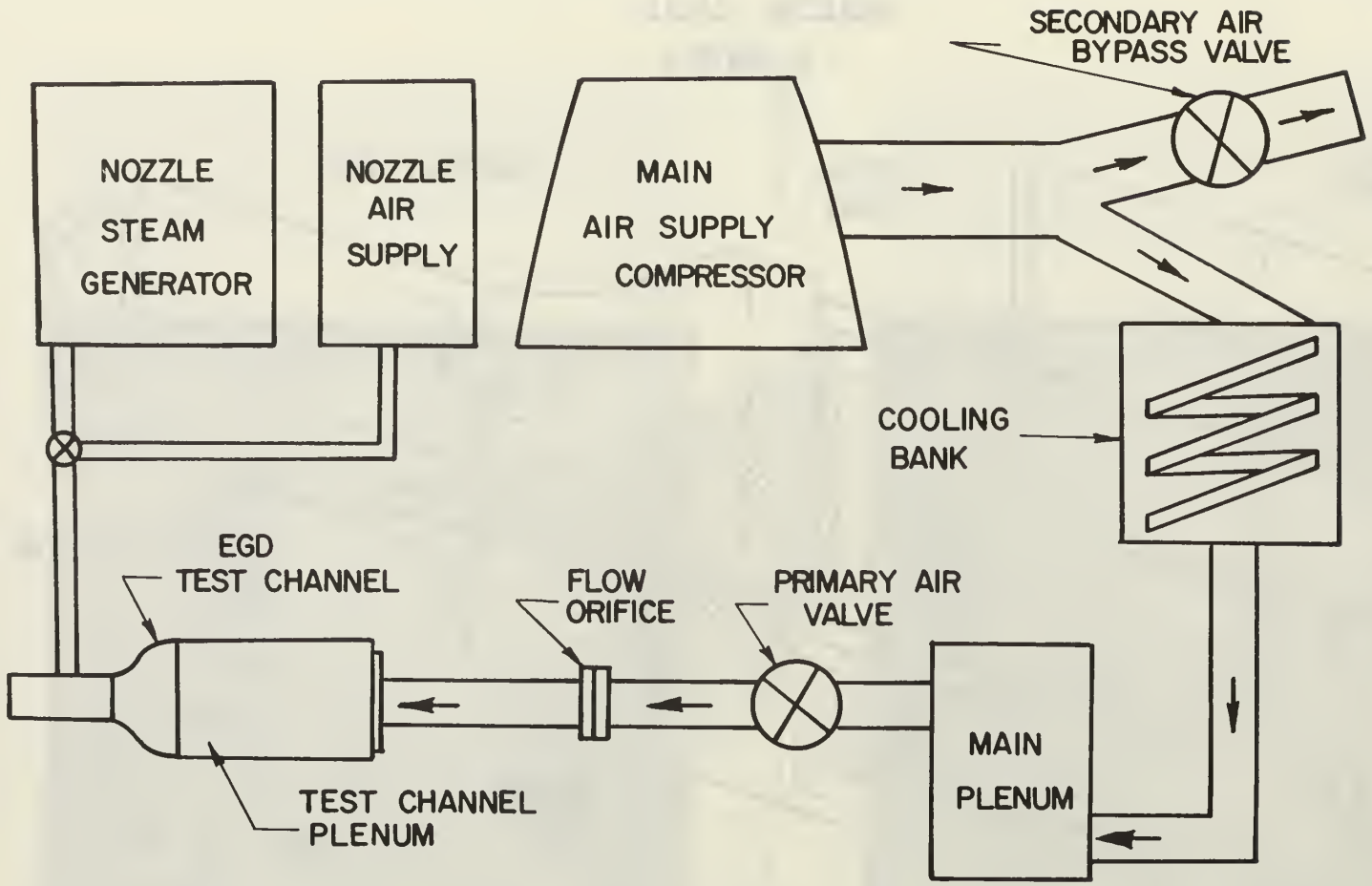

FIGURE 8

AIR AND STEAM FLOW SCHEMATIC.

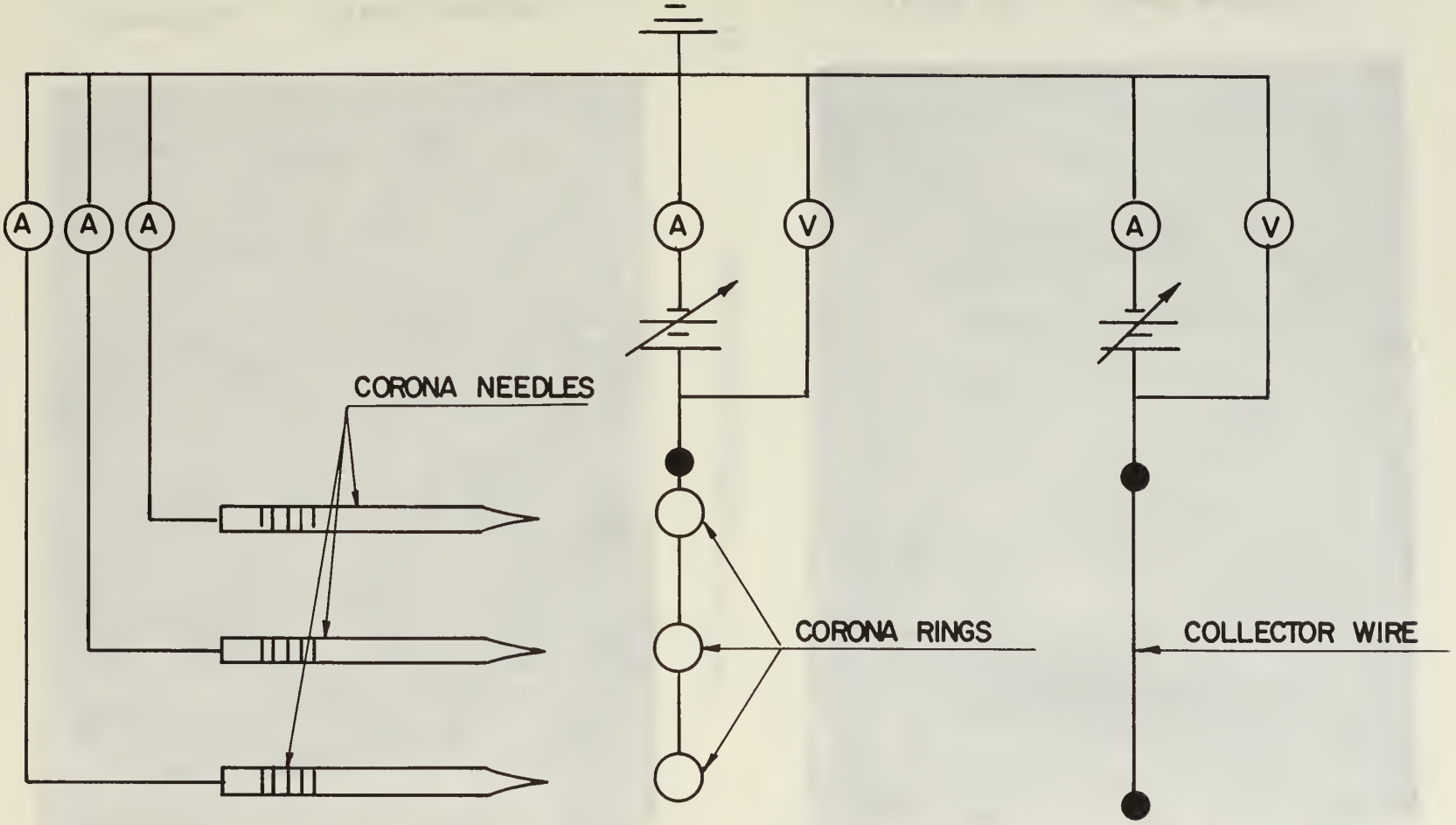

FIGURE 9. ELECTRICAL CIRCUITRY SCHEMATIC

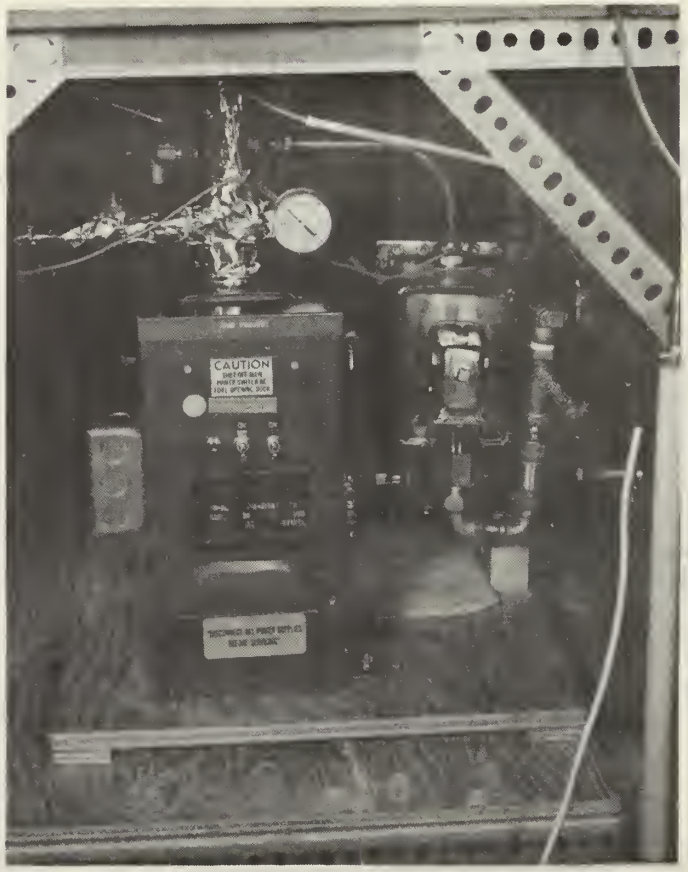

FIGURE 10A STEAM GENERATOR

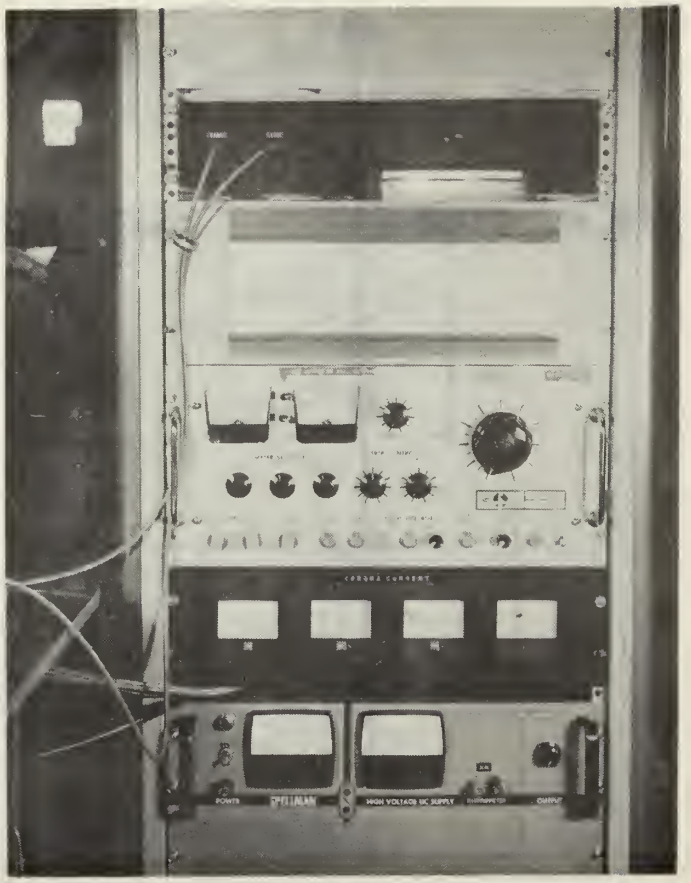

FIGURE 10B POWER SUPPLIES

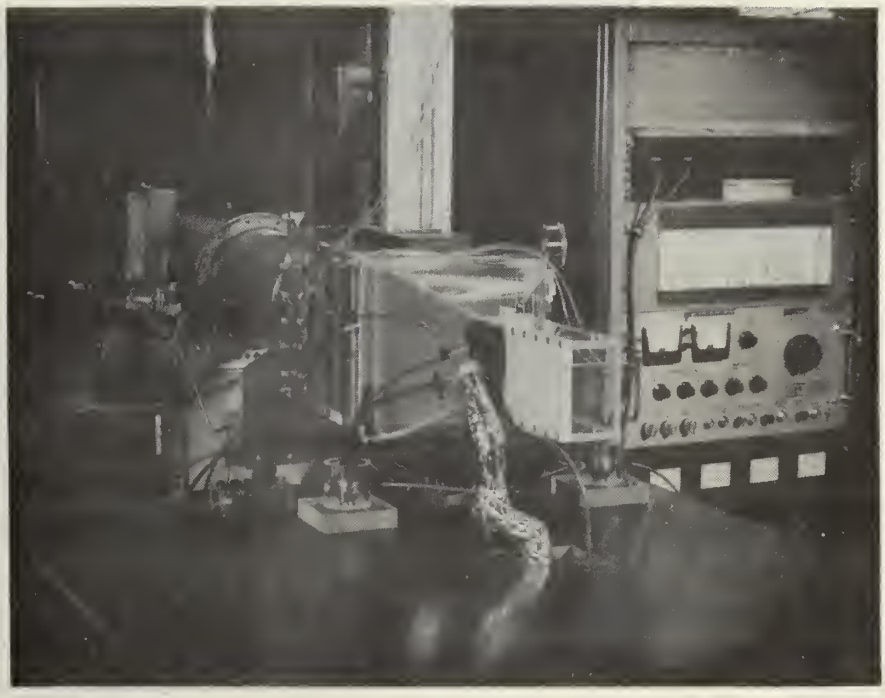

FIGURE 11A SUPPLY AND INSTRUMENTATION LINES

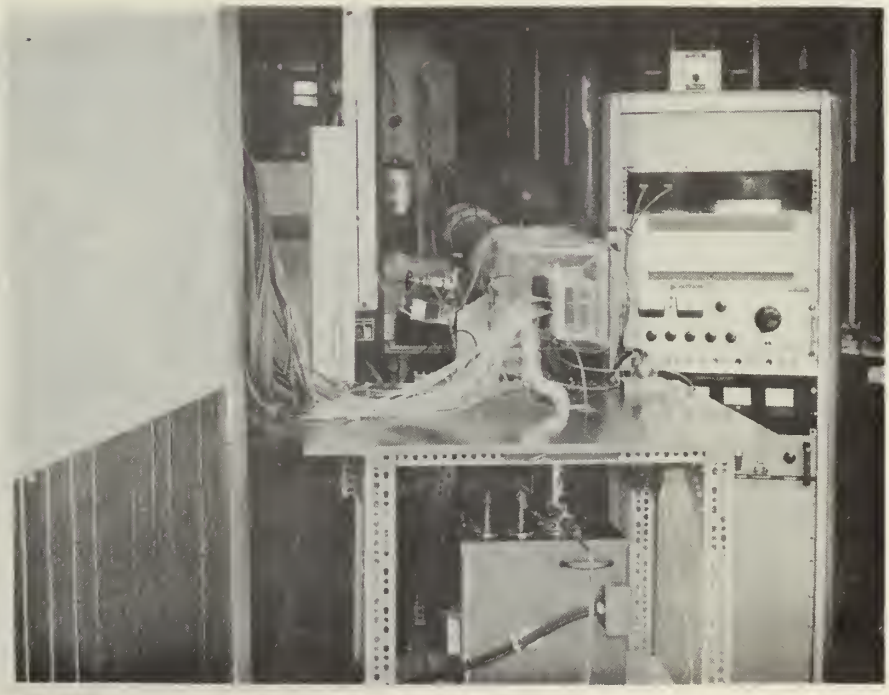

FIGURE 11B EXPERIMENTAL SETUP

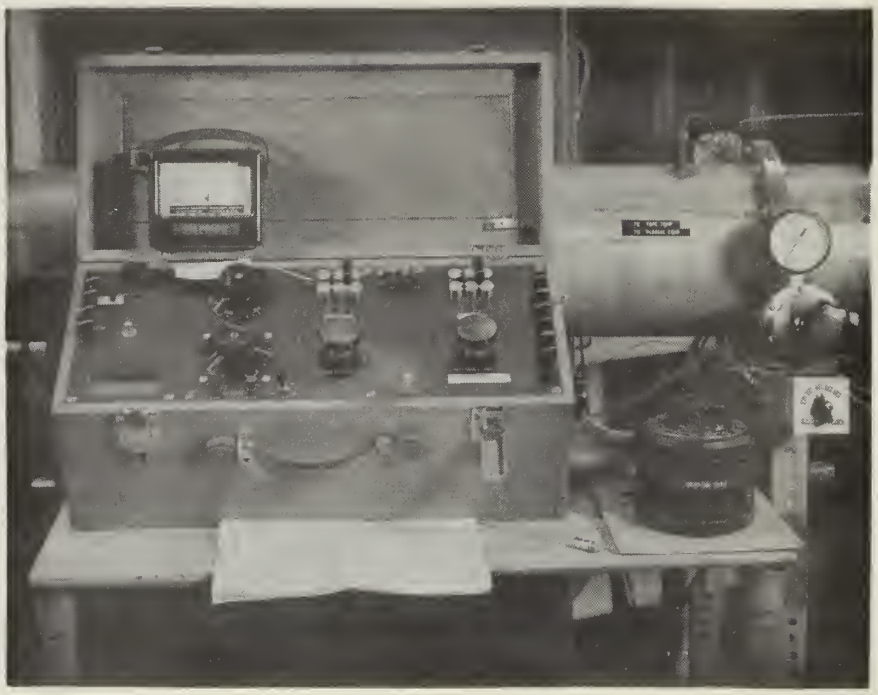

FIGURE 12A TEMPERATURE INSTRUMENTATION

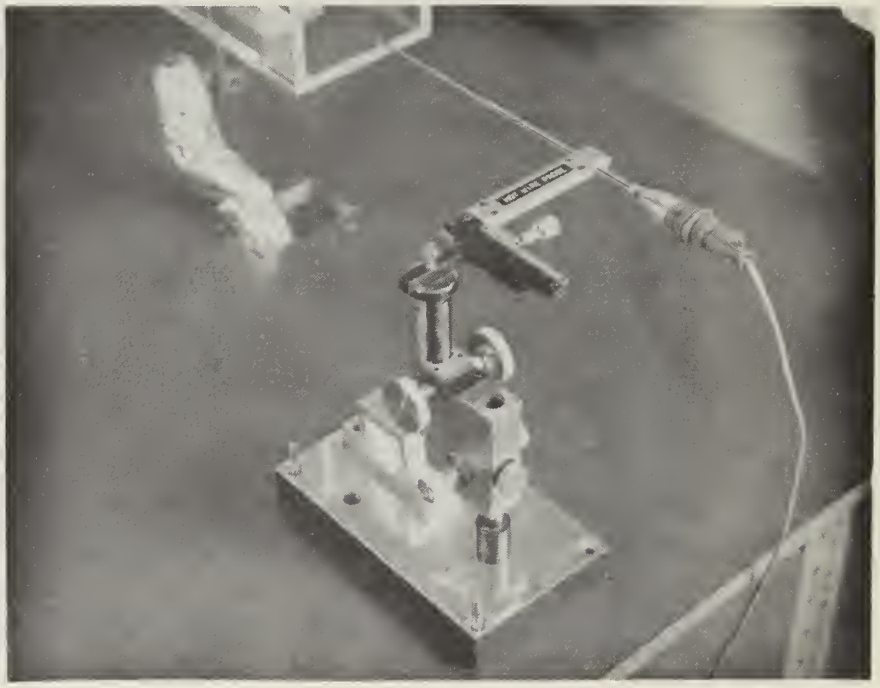

FIGURE 12B HOT WIRE TRAVERSE

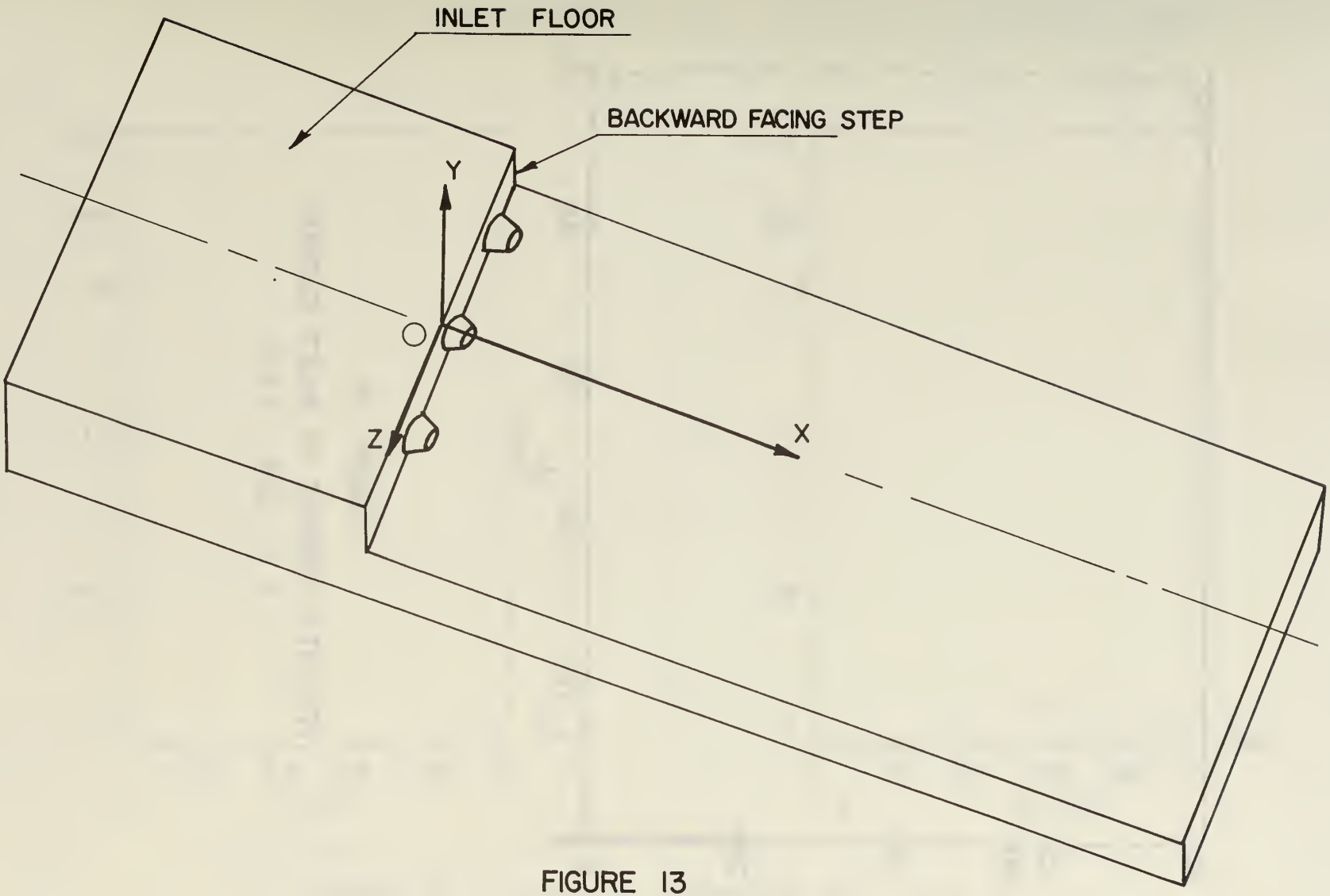

FIGURE 13

COORDINATE SYSTEM ATTACHED TO BACKWARD FACING STEP.

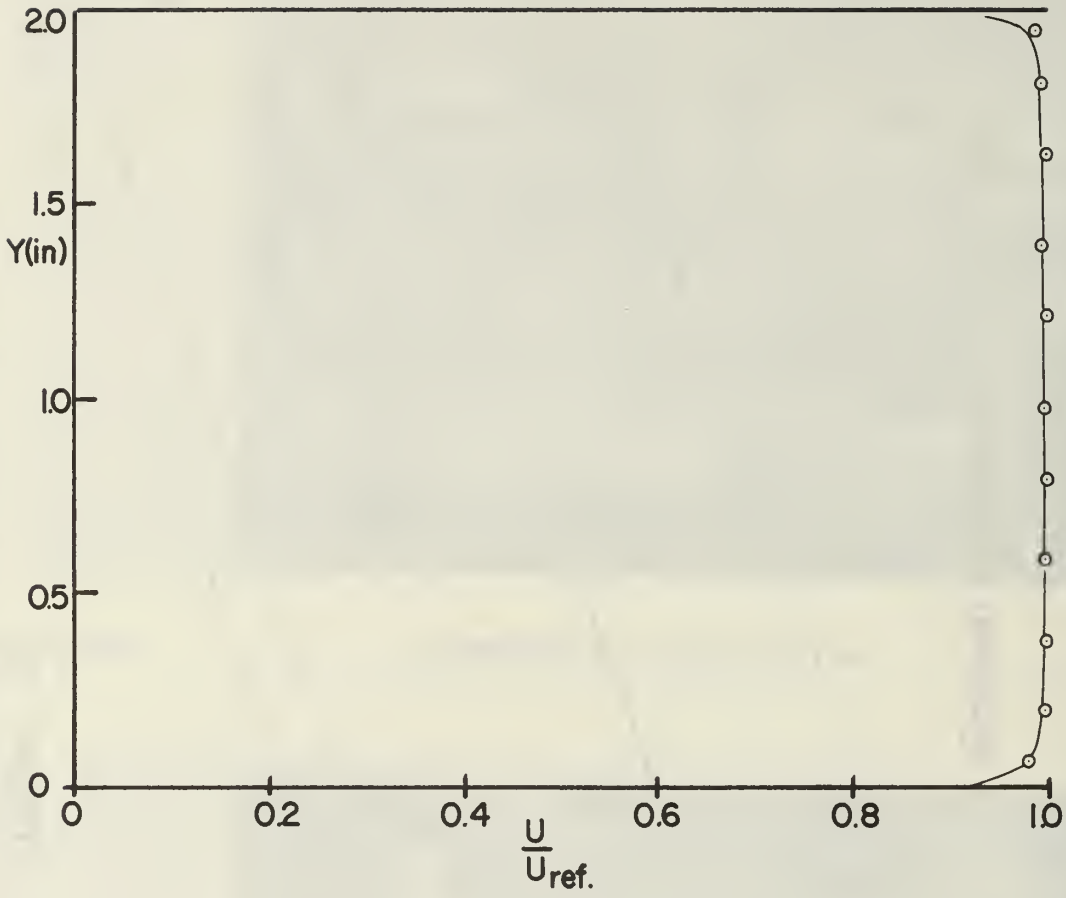

FIGURE 14

VELOCITY PROFILE IN INLET SECTION

X = -1.125 , Z = 0

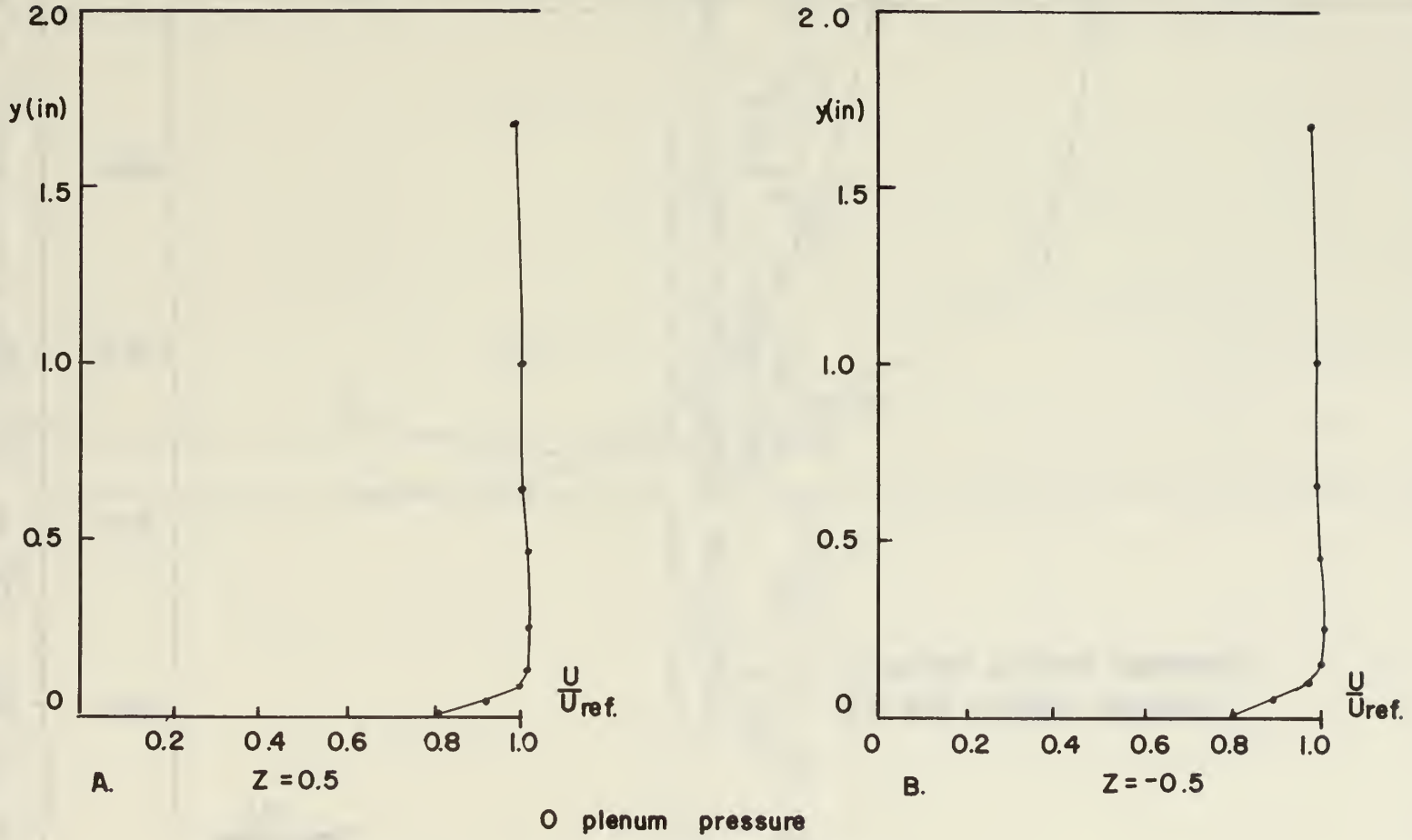

FIGURE 15. VELOCITY PROFILES AT x =0

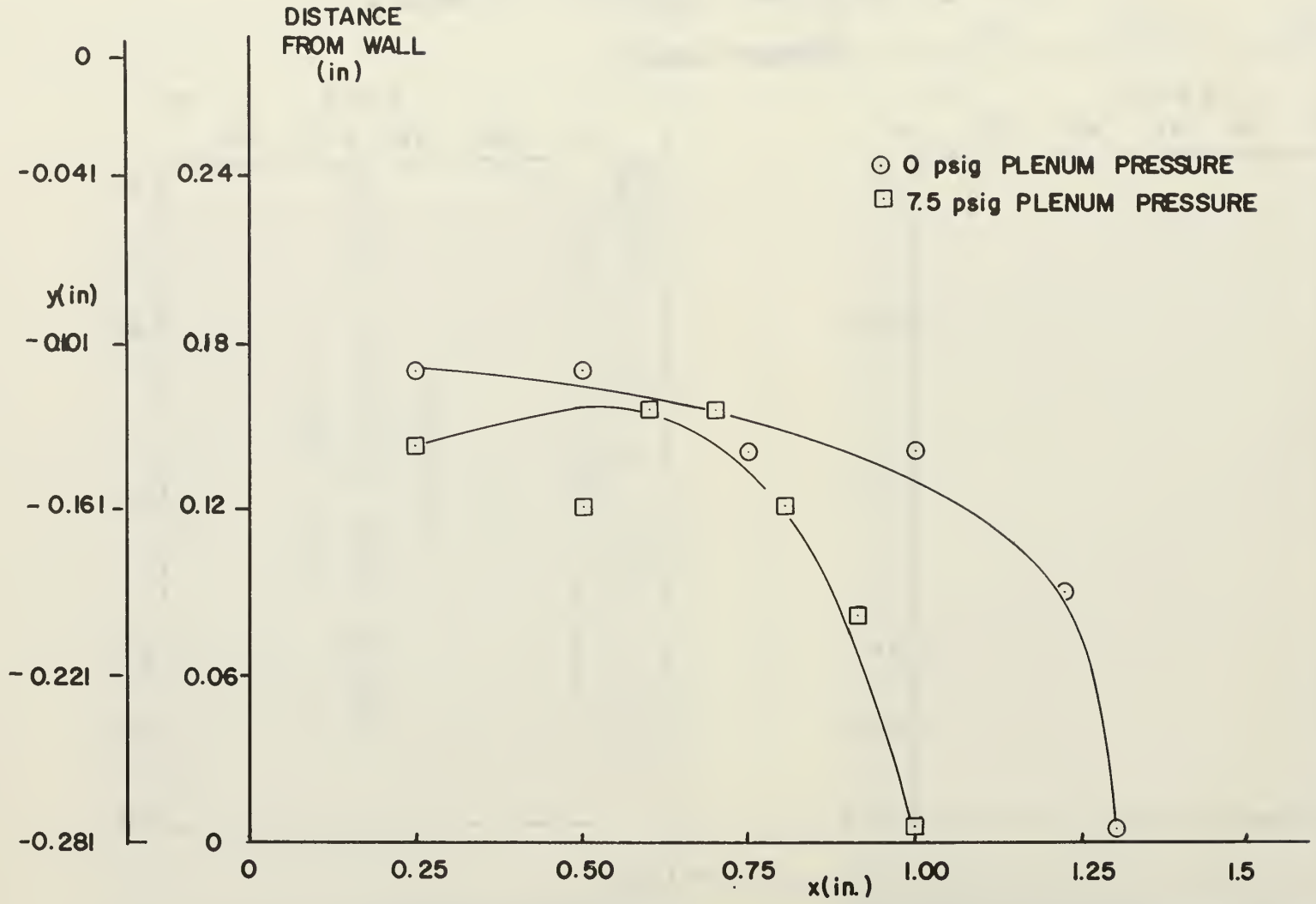

FIGURE 16. POINT OF MINIMUM VELOCITY IN SEPARATED AREA

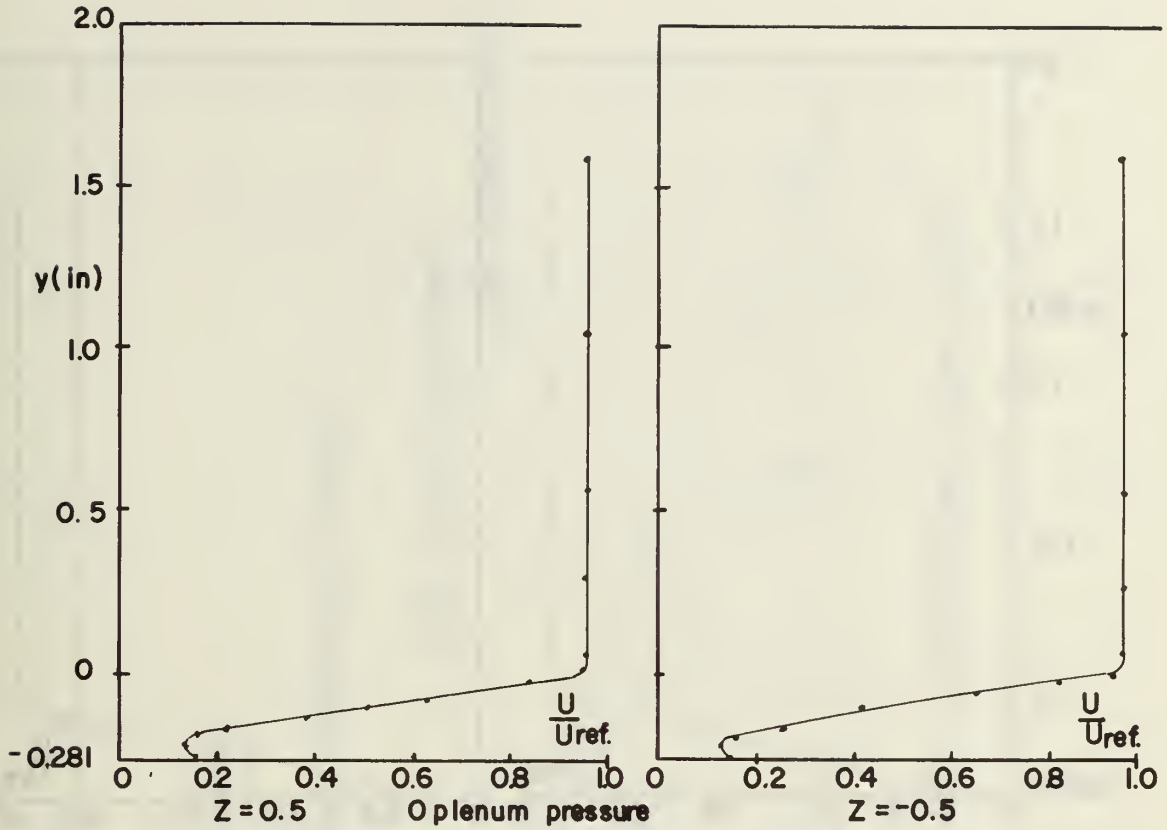

FIGURE 17 VELOCITY PROFILES BEFORE REATTACHMENT x=1.36

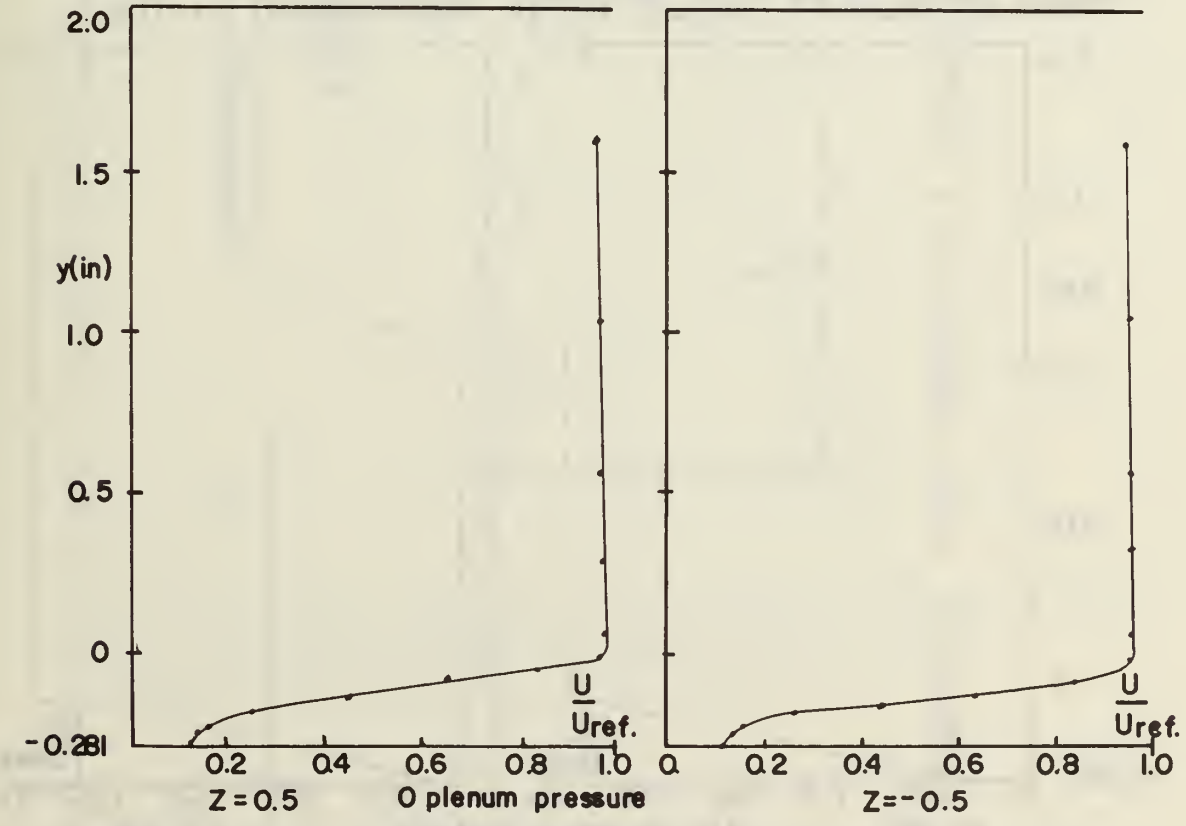

FIGURE 18. VELOCITY PROFILES AFTER REATTACHMENT x =1.38

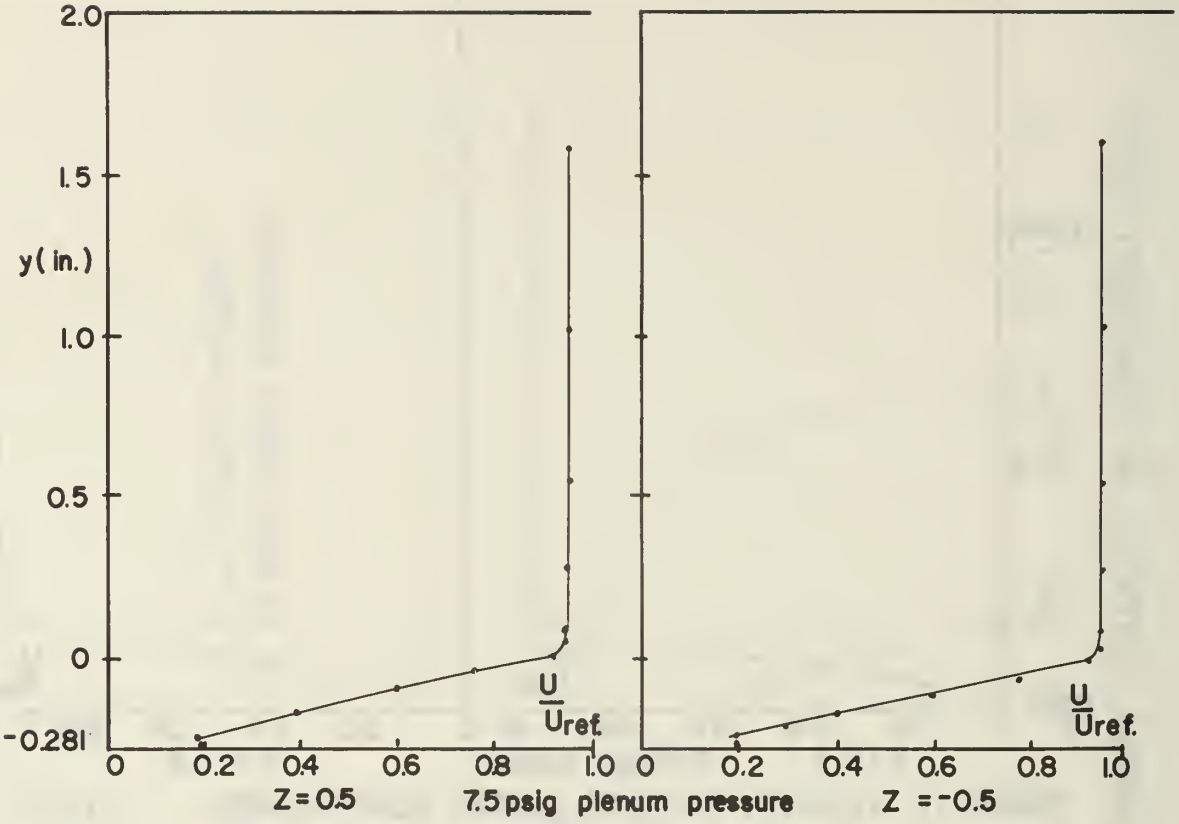

FIGURE 19 VELOCITY PROFILES BEFORE REATTACHMENT x = 1.00

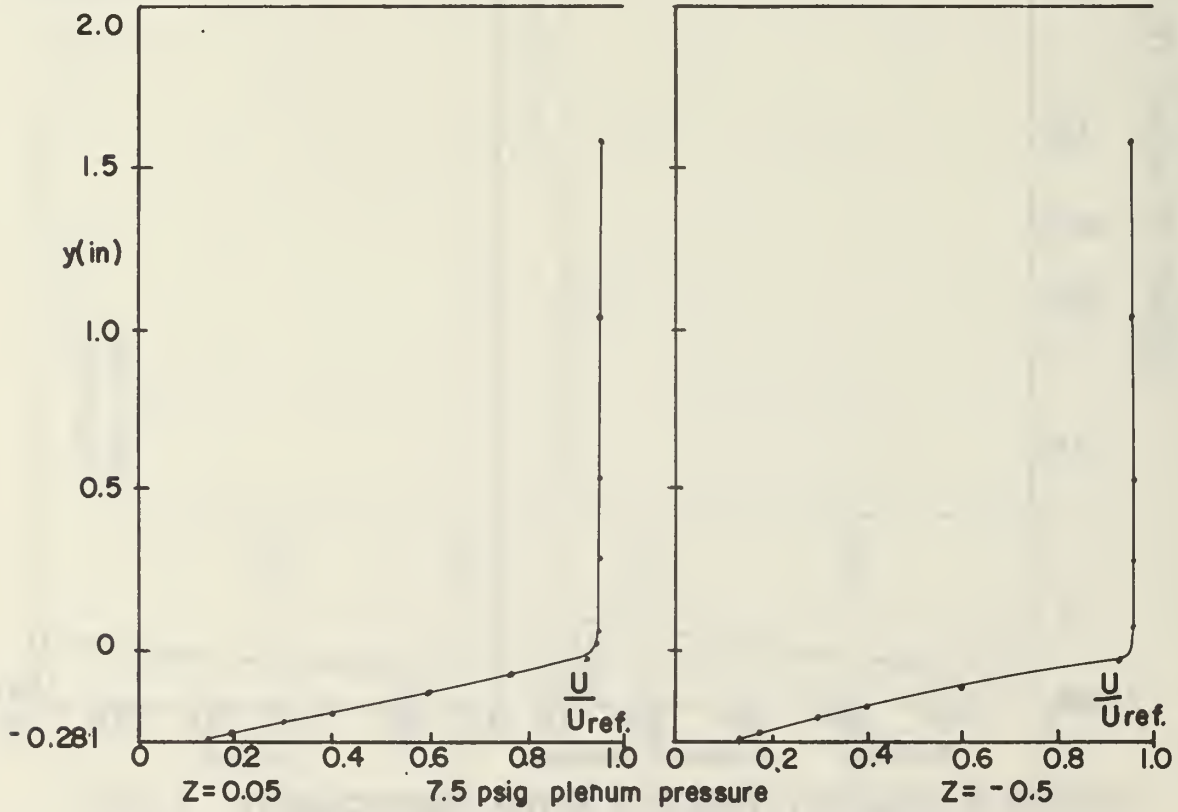

FIGURE 20. VELOCITY PROFILES AFTER REATTACHMENT. x = 1.02

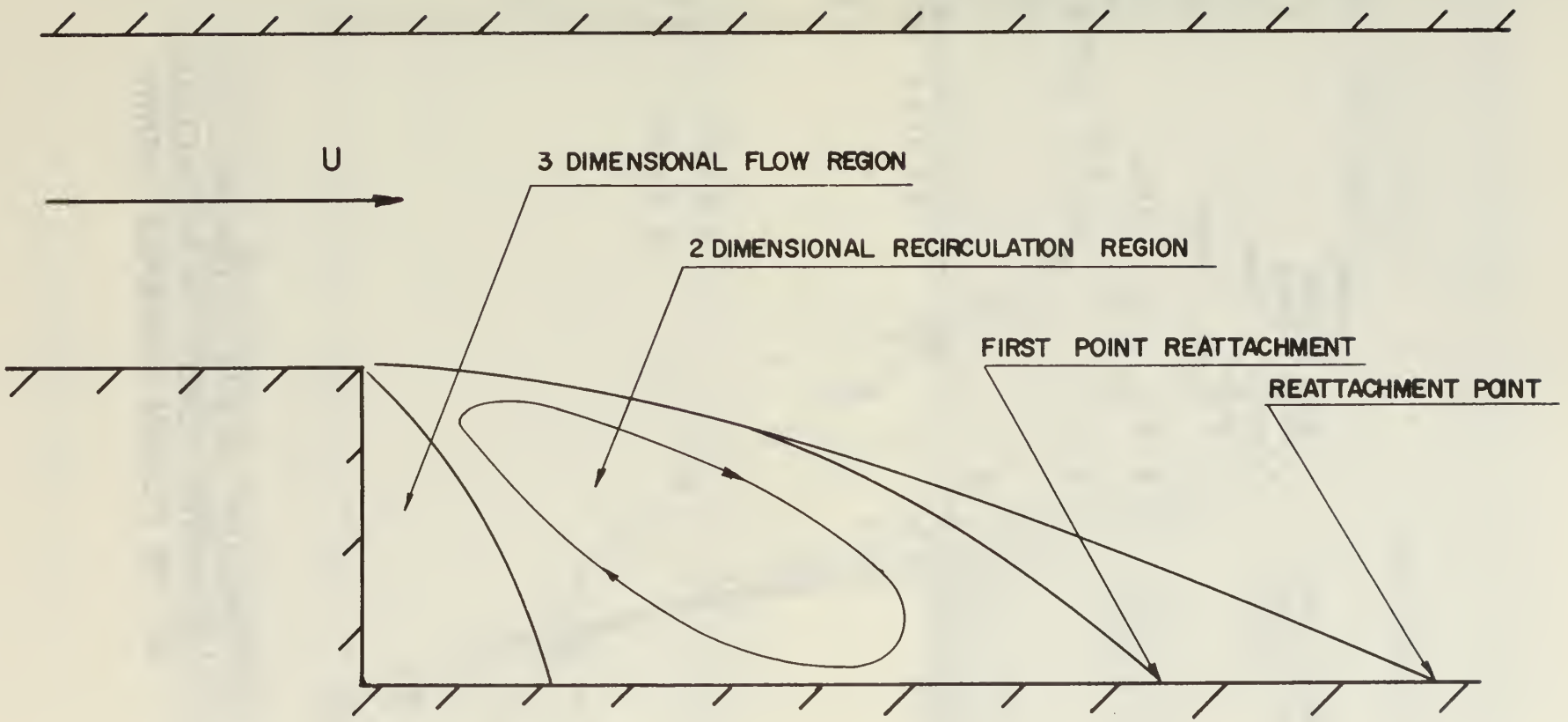

FIGURE 21. FLOW REGIONS IN A SEPARATED AREA DOWNSTREAM FROM A STEP.

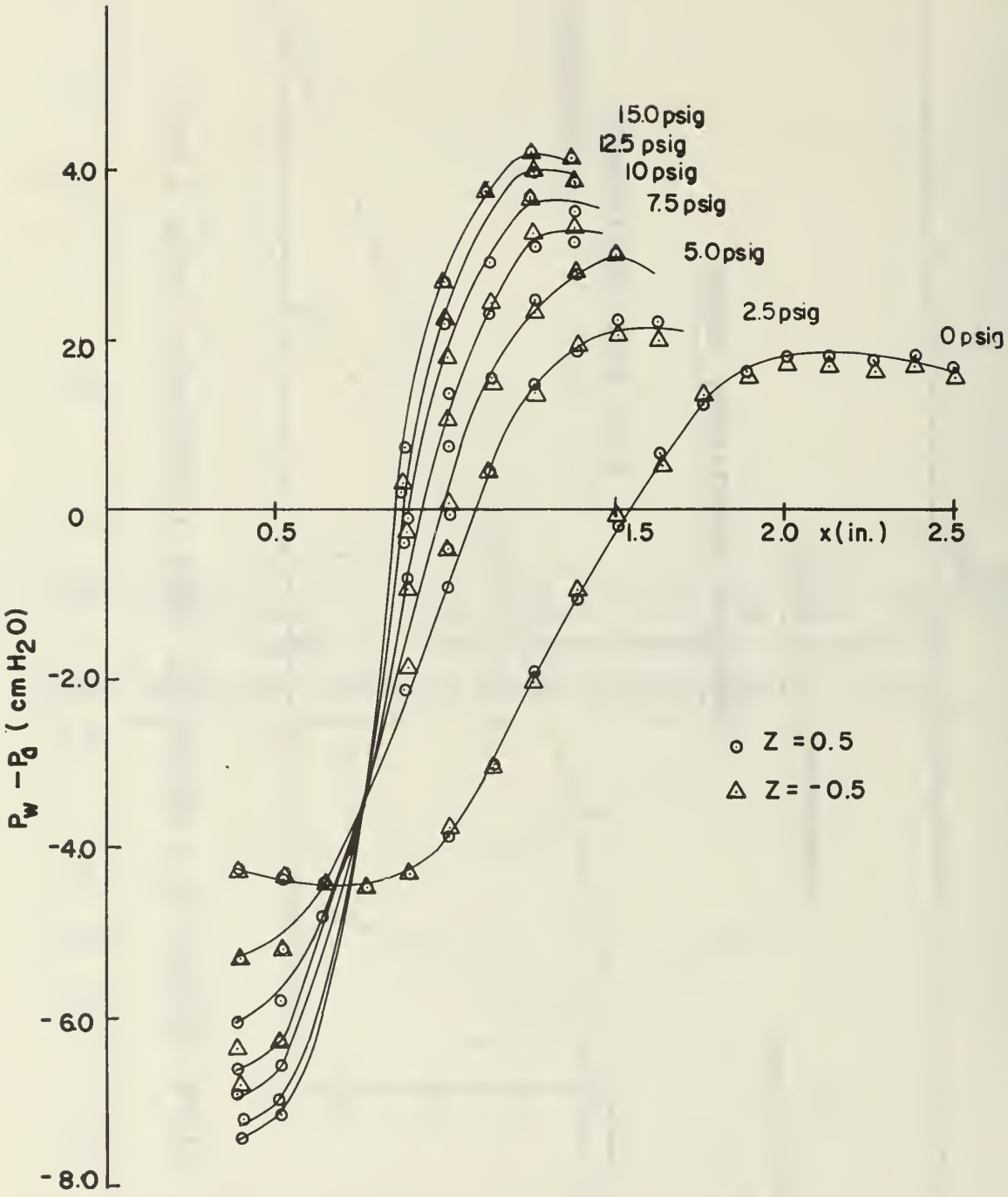

FIGURE 22. PRESSURE PROFILES ALONG WALL IN SEPARATED REGION FOR AIR INJECTION AT THE PLENUM PRESSURES SHOWN.

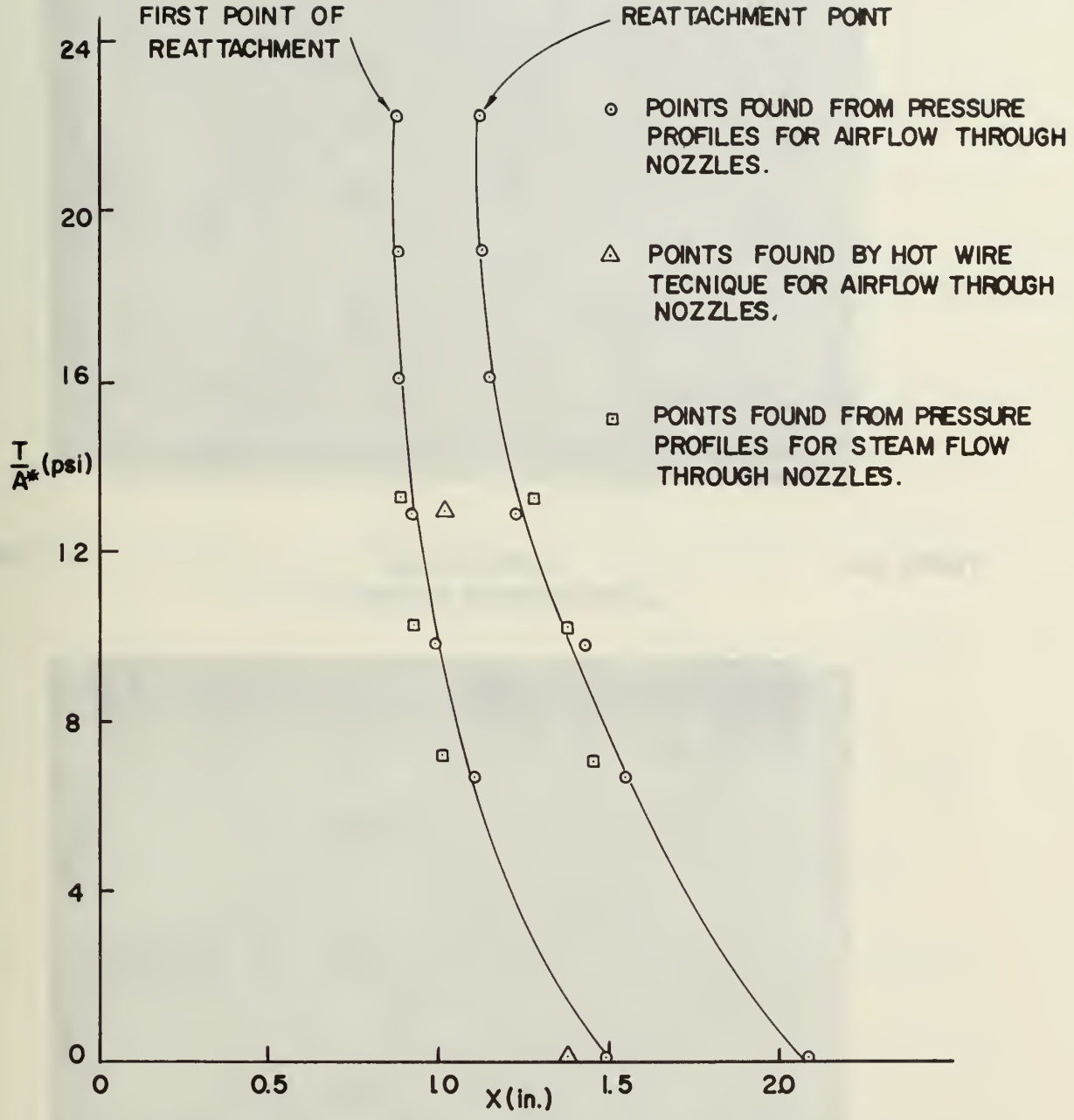

FIGURE 23. MOVEMENT OF REATTACHMENT POINT CAUSED BY NOZZLE THRUST PER UNIT AREA.

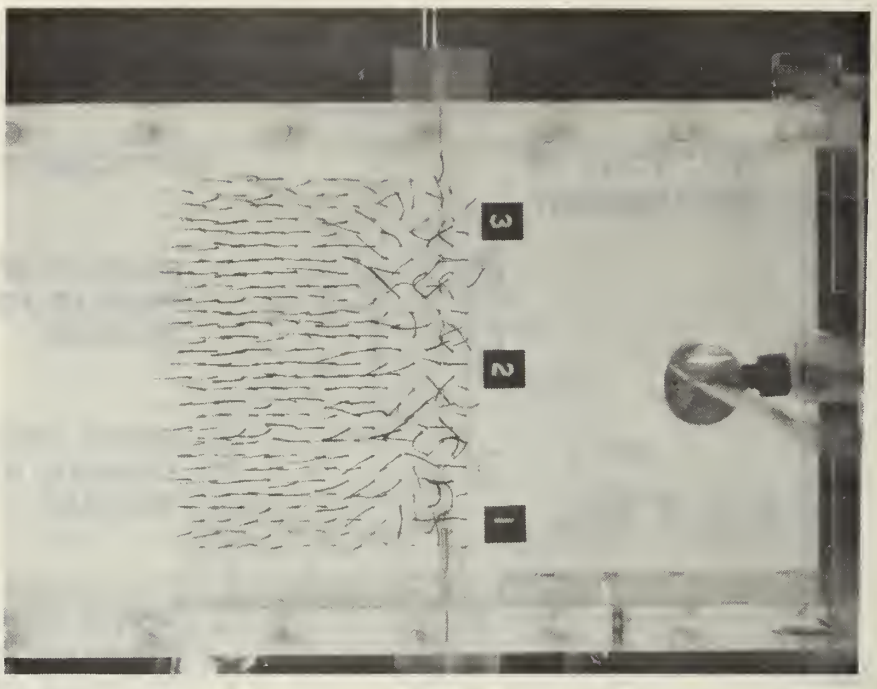

FIGURE 24A

TUFT PATTERN
ZERO PLENUM PRESSURE

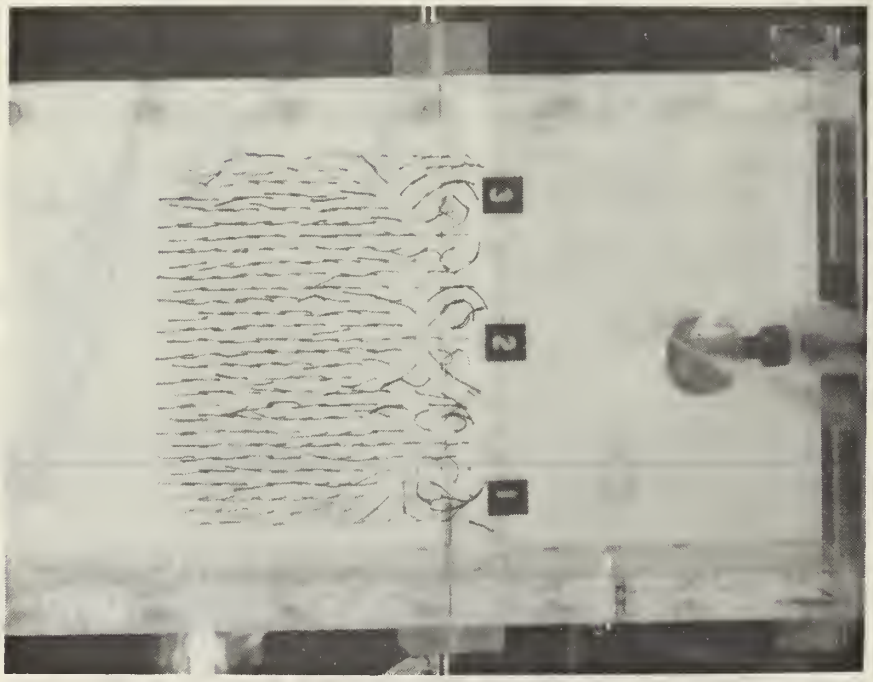

FIGURE 24B

TUFT PATTERN
2.5 psig PLENUM PRESSURE, STEAM

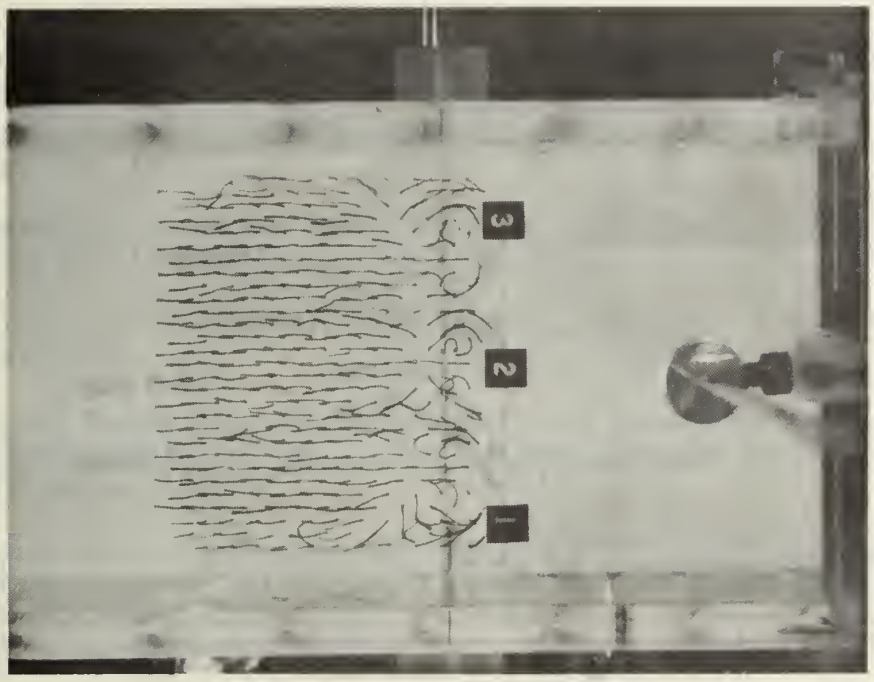

FIGURE 25A TUFT PATTERN
5.0 psig PLENUM PRESSURE, STEAM

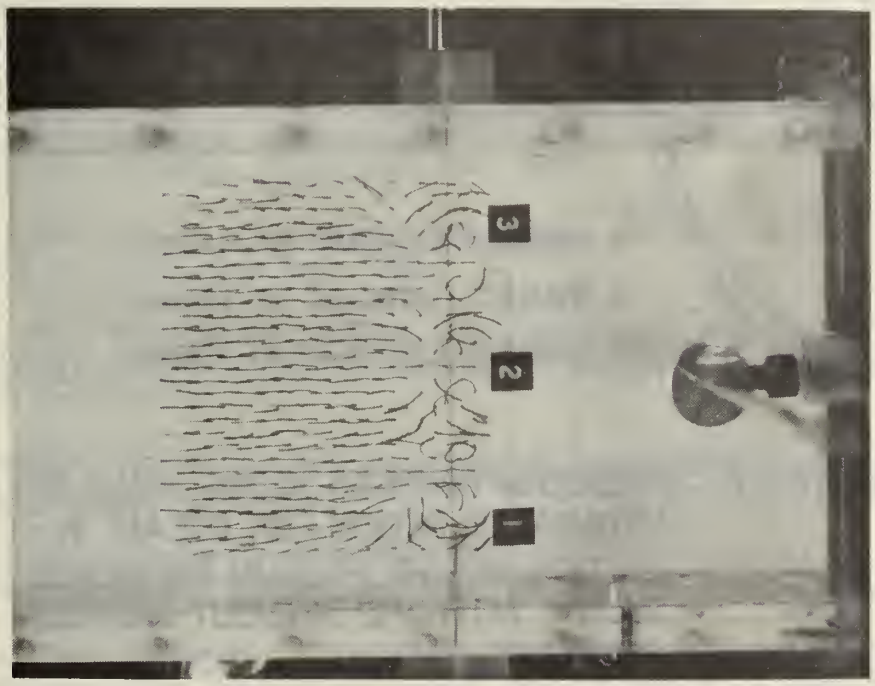

FIGURE 25B TUFT PATTERN
7.5 psig PLENUM PRESSURE, STEAM

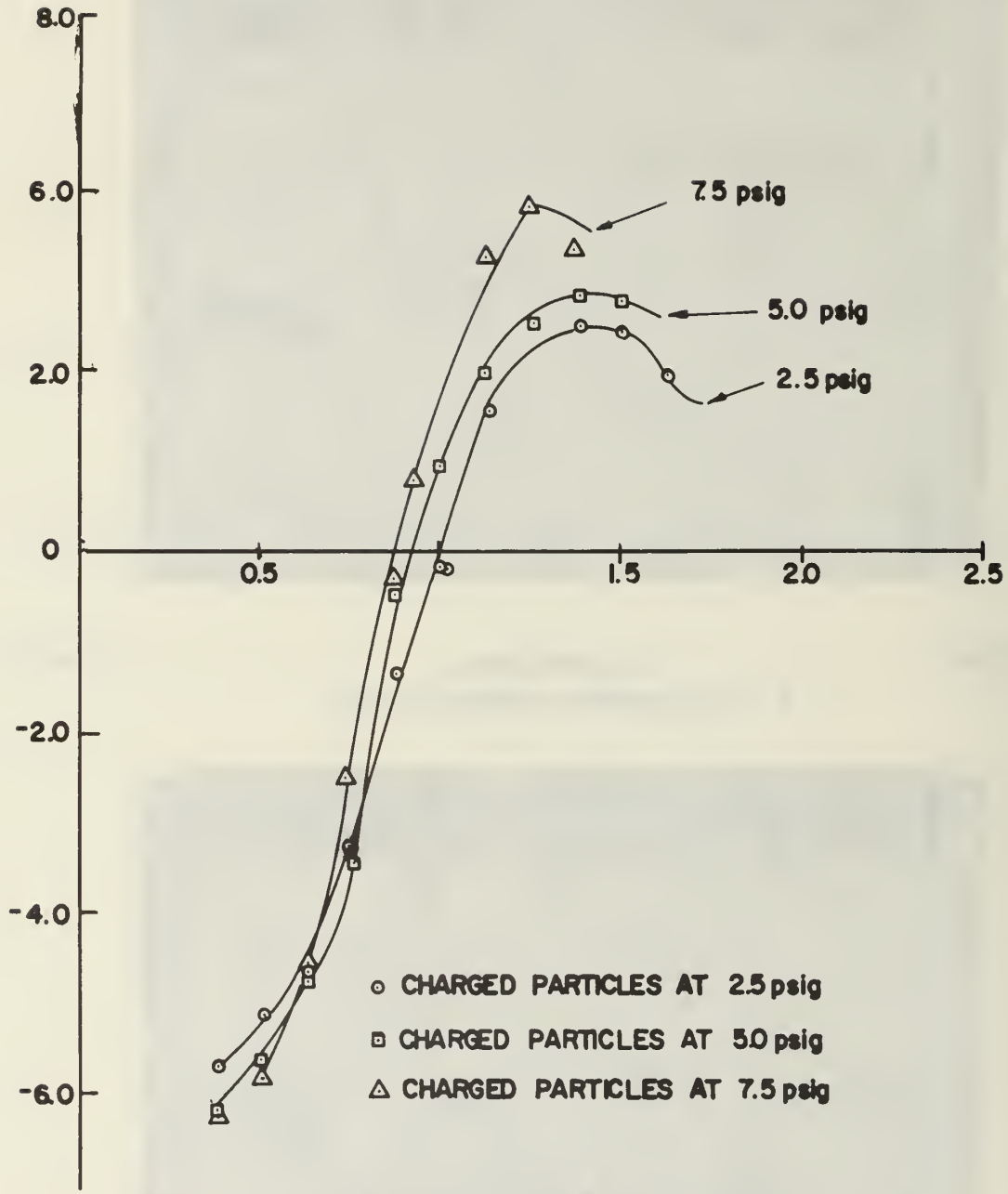

FIGURE 26. PRESSURE PROFILES ALONG WALL IN SEPARATED REGION FOR STEAM INJECTION AT THE PLENUM PRESSURES SHOWN WITH AND WITHOUT CHARGED PARTICLES.

BIBLIOGRAPHY

1. Abbott, D. W. and Kline, S. J., "Experimental Investigation of Subsonic Turbulent Flow over Single and Double Backward Facing Steps", Transactions of the ASME Journal of Basic Engineering, p. 317-325 September 1962.

2. Abbott,I. H. and Von Doenhoff, A. E., The Theory of Wing Sections, Dover Publications Inc., New York 1959.

3. Alston, L. L. (Editor), High Voltage Technology, Oxford University Press 1963.

4. United States Naval Postgraduate School Report NPS-57Z I912A, EHD Research Final Report for the Year 1968-69, by Oscar Biblarz, 30 December 1969.

5. Cheng, Sin-I, Aerospace Applications of Electro-Aerodynamic Interaction, proceedings of the International Symposium on Electrohydrodynamics, Massachusetts Institute of Technology, p. 147-150 31 March, 1-2 April 1969.

6. Aerospace Research Laboratories Report ARL65-4 A Continuation of the Basic Study of Slender Channel Electrogasdynamics, by Bernard Kahn, January 1965.

7. Marks, A., Barreto, E., and Chu, C. K., Charged Aersol Energy Converter, paper presented at AIAA Summer Meeting, Los Angeles, California 17-20 June 1963.

8. Ober, Lt.(j.g.) William, Ion Injector for Single and Two-Phase Electrogasdynamic Generators, Master's Thesis, Naval Postgraduate School, Monterey, California June 1969.

9. Schlichting, H., Boundary Layer Theory, 4th ed., McGraw Hill Book Co. Inc., New York 1960.

10. Shaar, Lcdr. Camille Maleek, Jr., Ionization and Boundary Layer Control, Master's Thesis, Rensselaer Polytechnic Institute, Troy, New York 1947.

11. Shapiro, Ascher H., The Dynamics and Thermodynamics of Compressible Fluid Flow, Vol. 1, p. 102-103, The Ronald Press Co., New York 1953.

12. Stuetzer, Otmar M., Electrohydrodynamic Flow Control, a paper prepared at Sandia Laboratory, Alburquerque, New Mexico (unpublished).

13. Stuetzer, Otmar M., "Instability of Certain Electrohydrodynamic Systems," The Physics of Fluids, Vol. 2, No. 6, p. 642-643, November-December 1959

14. Wood, Karl D., Technical Aerodynamics, 2nd Ed., McGraw Hill Book Co. Inc., New York 1947.

DISTRIBUTION LIST

		No. Copies
1.	Defense Documentation Center Cameron Station Alexandria, Virginia 22314	20
2.	Library Naval Postgraduate School Monterey, California 93940	2
3.	Commander Naval Air Systems Command Department of The Navy Attn: Dr. H. R. Rosenwasser, Code AIR-310C	2
4.	Chairman Department of Aeronautics Naval Postgraduate School Monterey, California 93940	1
5.	Professor T. H. Gawain Department of Aeronautics Naval Postgraduate School Monterey, California 93940	1
6.	Professor K. E. Woehler Physics Department Naval Postgraduate School Monterey, California 93940	1
7.	Professor Oscar Biblarz Department of Aeronautics Naval Postgraduate School Monterey, California 93940	6
8.	Professor J. R. Melcher Dept. of Elec. Engr., Room 31-141 Mass. Inst. of Technology Cambridge, Massachusetts 02139	1
9.	Professor Albert Solbes Dept. of Aero., Room 37-375 Mass. Inst. of Technology Cambridge, Massachusetts 02139	1
10.	Mr. Alvin M. Marks Marks Polarized Corp. 153-16 10th Avenue Whitestone, New York 11357	1

11. Dr. M. C. Gourdine — 1
Gourdine Systems, Inc.
112 Naylon Avenue
Livingston, New Jersey 07039

12. Dr. Hans von Ohain — 1
Aerospace Research Laboratory
U. S. Air Force
Wright-Patterson AFB, Ohio 45433

13. Professor A. E. Fuhs — 1
Department of Aeronautics
Naval Postgraduate School
Monterey, California 93940

14. Dr. Ernesto Barreto — 1
Atmospheric Research Center
State University of New York
130 Saratoga Road
Scotia, New York 12302

15. Professor H. R. Velkoff — 1
Dept. of Mech. Engr.
Ohio State University
Columbus, Ohio 43210

16. Dr. Otmar M. Stuetzer — 1
Sandia Corporation
P. O. Box 5800
Alburquerque, New Mexico 87115

17. Dr. Ralph Roberts — 1
Office of Naval Research
Power Program, Code 473
Washington, D. C. 20360

18. Mr. John A. Stakowski — 1
Office of Naval Research
Power Program, Code 473
Washington, D. C. 20360

19. Dr. H. J. Mueller — 1
Naval Air Systems Command
Code AIR 310
Washington, D. C. 20360

20. Dr. S. J. Magram — 1
Army Research Office
Arlington, Virginia 22200

21. Air Force Office of Scientific Research — 1
Washington, D. C. 20333
Attn: Power Systems Group

22. Mr. Robert C. Hamilton — 1
Institute of Defense Analysis
400 Army - Navy Drive
Arlington, Virginia 22202

23. Dr. George C. Szego — 1
Institute of Defense Analysis
400 Army - Navy Drive
Arlington, Virginia 22202

24. Mr. S. Cohen — 1
NASA Lewis Research Center
21000 Brookpark Road
Cleveland, Ohio 44135

25. Mr. M. Lawson — 1
Aerospace Research Laboratory
U. S. Air Force
Wright-Patterson AFB, Ohio 45433

26. Dean of Research Administration — 2
Naval Postgraduate School
Monterey, California 93940

27. Professor C. D. Hendricks — 1
Department of Electrical Engineering
University of Illinois
Urbana, Illinois 61801

28. CAPT T. C. Willke — 1
Aerospace Research Laboratory
U. S. Air Force
Wright-Patterson AFB, Ohio 45433

Unclassified

Security Classification

DOCUMENT CONTROL DATA - R & D

(Security classification of title, body of abstract and indexing annotation must be entered when the overall report is classified)

1. ORIGINATING ACTIVITY *(Corporate author)*

Naval Postgraduate School
Monterey, California 93940

2a. REPORT SECURITY CLASSIFICATION

Unclassified

2b. GROUP

3. REPORT TITLE

EHD Research
Final Report for the Year 1969-70

4. DESCRIPTIVE NOTES *(Type of report and inclusive dates)*

5. AUTHOR(S) *(First name, middle initial, last name)*

Oscar Biblarz, K. E. Woehler, and T. H. Gawain

6. REPORT DATE	7a. TOTAL NO. OF PAGES	7b. NO. OF REFS
December 1970		10

8a. CONTRACT OR GRANT NO.	9a. ORIGINATOR'S REPORT NUMBER(S)
AIRTASK No. A340C/551A/0R0 100 2010	NPS-57ZI0121A
b. PROJECT NO.	
c.	9b. OTHER REPORT NO(S) *(Any other numbers that may be assigned this report)*
d.	

10. DISTRIBUTION STATEMENT

This document has been approved for public release and sale; its distribution is unlimited

11. SUPPLEMENTARY NOTES	12. SPONSORING MILITARY ACTIVITY
	Naval Air Systems Command Washington, D. C. 20360

13. ABSTRACT

This is the second year-end report on the EHD contract. Whereas previous work concentrated on building up the experimental facility and on delineating the effects of turbulence on breakdown, this work details the effects of turbulence on charged particle mobility. The two-phase injector is used exclusively.

Spectral measurements of velocity and collector current are reported. These are used to determine the potential use of EHD in anemometry and to deduce particle size distributions. Measurements of charge distribution are also reported and a comparison is made between these and the spectral measurements.

Equations defining an axisymmetric, turbulent EHD flow have been derived. Also, the feasibility of flow separation control with an EHD interaction has been investigated.

Research plans for the coming year are outlined in this report.

14 KEY WORDS	LINK A		LINK B		LINK C	
	ROLE	WT	ROLE	WT	ROLE	WT
Electrohydrodynamics						
Electrogasdynamics						
Turbulence						
Drift velocity						
Charged particle size distribution						
Particle Charge distribution						
Anemometry						
Separation Control						
Direct Energy Conversion						